TOPOLOGICAL PHASE OF MATTER AND FLOQUET CODES

by

Bowen Yan

A Dissertation

Submitted to the Faculty of Purdue University

In Partial Fulfillment of the Requirements for the degree of

Doctor of Philosophy

Department of Physics and Astronomy

West Lafayette, Indiana

December 2024

THE PURDUE UNIVERSITY GRADUATE SCHOOL
STATEMENT OF COMMITTEE APPROVAL

Dr.Xingshan Cui, Chair

Department of Mathematics

Dr. Jukka Vayrynen

Department of Physics and Astronomy

Dr. Arnab Banerjee

Department of Physics and Astronomy

Dr. Ralph Kaufmann

Department of Mathematics

Approved by:

Dr. Gabor Csathy

ACKNOWLEDGMENTS

First, I would like to express my deepest gratitude to my advisor, Xingshan Cui. I am profoundly thankful for his unwavering encouragement, freedom, and understanding throughout my studies and research. His vast knowledge and sharp insights have been invaluable, as he consistently identified the crux of my confusions and explained them with remarkable clarity, detail, and patience. This thesis would not have been possible without his clear guidance and support.

I would also like to thank my undergraduate advisor, Changgan Zeng, who introduced me to the fascinating world of flat-band systems and gave me my first exposure to the intriguing realm of strongly correlated electrons. My gratitude extends to Chris Greene, who helped me delve into AMO physics, guiding me through this fundamental and enriching field.

My heartfelt thanks go to my committee members: Arnab Banerjee, Jukka Vayrynen, and Ralph Kaufmann. I am deeply grateful for their valuable advice, encouragement, time, and insightful discussions, which have driven me to improve and progress. A special thank you to Jukka Vayrynen for his kind encouragement and for introducing me to his research group, where I immersed myself in an inspiring condensed matter physics environment and gained a deeper understanding of topological phases of matter in physical systems.

I also owe special thanks to Martin Kruczenski for introducing me to conformal field theory and for his continued support and encouragement throughout my journey.

I want to express my gratitude to my friends Yuming Shi, Penghua Chen, Yuchen Wang, Xi Cheng, and Guangjie Li. A special thanks goes to Penghua Chen for being an incredible collaborator and providing invaluable support. My deep thanks also go to Yuming Shi for always being a thoughtful listener and engaging in genuine and meaningful conversations with me. To my 5-year roommate Yuchen Wang, I am truly grateful for your endless help and friendship during this time.

I also thank Nan Cheng for the memorable trips and passionate academic discussions that have made this journey even more meaningful. My thanks also go to Zhengmian Hu and Xingrui Song for the many joyful and thought-provoking discussions on various topics.

Lastly, I must express my greatest gratitude to my parents. Your unwavering support and presence, especially during difficult times, have been my anchor. I could not have achieved this without your love and encouragement. Thank you for standing with me and believing in me every step of the way.

TABLE OF CONTENTS

LIST OF TABLES

LIST OF FIGURES

ABSTRACT

This abstract contains work from the article entitled "Floquet Codes from Coupled Spin Chains" written by the author, Penghua Chen, and Shawn X. Cui published on arXiv [1], and the article entitled "Generalized Kitaev spin liquid model and emergent twist defect" written by the author, Penghua Chen, and Shawn X. Cui published on Annals of Physics [2], and the article entitled "Ribbon operators in the generalized Kitaev quantum double model based on Hopf algebras" written by the author, Penghua Chen, and Shawn X. Cui published on Journal of Physics A [3].

Kitaev's quantum double model is a family of exactly solvable lattice models that realize two dimensional topological phases of matter. The model was originally based on finite groups, and was later generalized to semi-simple Hopf algebras. In this thesis, We rigorously define and study ribbon operators in the generalized quantum double model. These ribbon operators are important tools to understand quasi-particle excitations. It turns out that there are some subtleties in defining the operators in contrast to what one would naively think of. In particular, one has to distinguish two classes of ribbons which we call locally clockwise and locally counterclockwise ribbons. Moreover, we point out that the issue already exists in the original model based on finite non-Abelian groups, but it seems to not have been noticed in the literature. We show how certain common properties would fail even in the original model if we were not to distinguish these two classes of ribbons. Perhaps not surprisingly, under the new definitions ribbon operators satisfy all properties that are expected. For instance, they create quasi-particle excitations only at the end of the ribbon, and the types of the quasi-particles correspond to irreducible representations of the Drinfeld double of the input Hopf algebra. However, the proofs of these properties are much more complicated than those in the case of finite groups. This is partly due to the complications in dealing with general Hopf algebras rather than group algebras.

On the other hand, the Kitaev spin liquid model on a honeycomb lattice offers an intriguing feature that encapsulates both Abelian and non-Abelian phases [4]. Recent studies suggest that the comprehensive phase diagram of the possible generalized Kitaev model largely depends on the specific details of the discrete lattice, which somewhat deviates from the traditional understanding of "topological" phases. In the second part of this thesis, we propose an adapted version of the Kitaev spin liquid model on arbitrary planar lattices. Our

revised model recovers the surface code model under certain parameter selections within the Hamiltonian terms. Changes in parameters can initiate the emergence of holes, domain walls, or twist defects. Notably, the twist defect, which presents as a lattice dislocation defect, exhibits non-Abelian braiding statistics upon tuning the coefficients of the Hamiltonian. Additionally, we illustrate that the creation, movement, and fusion of these defects can be accomplished through natural time evolution by linearly interpolating the static Hamiltonian. These defects demonstrate the Ising anyon fusion rule as anticipated. Our findings hint at possible implementation in actual physical materials owing to a more realistically achievable two-body interaction.

The topological phase of matter not only supports anyons as quasi-particle excitations but also exhibits a long-range entangled ground state, which often functions as a quantum error-correcting code. The Floquet code is introduced to reduce the high cost of measuring many-body syndrome operators. In the third part of this thesis, we propose a novel construction of the Floquet 3D toric code and Floquet X-cube code through the coupling of spin chains. This approach not only recovers the coupling layer construction on foliated lattices in three dimensions but also avoids the complexity of coupling layers in higher dimensions, offering a more localized and easily generalizable framework. Our method extends the Floquet 3D toric code to a broader class of lattices, aligning with its topological phase properties. Furthermore, we generalize the Floquet X-cube model to arbitrary manifolds, provided the lattice is locally cubic, consistent with its Fractonic phases. We also introduce a unified error-correction paradigm for Floquet codes by defining a subgroup, the Steady Stabilizer Group (SSG), of the Instantaneous Stabilizer Group (ISG), emphasizing that not all terms in the ISG contribute to error correction, but only those terms that can be referred to at least twice before being removed from the ISG. We show that correctable Floquet codes naturally require the SSG to form a classical error-correcting code, and we present a simple 2-step Bacon-Shor Floquet code as an example, where SSG forms instantaneous repetition codes. Finally, our construction intrinsically supports the extension to n-dimensional Floquet $(n, 1)$ toric codes and generalized n-dimensional Floquet X-cube codes.

1. INTRODUCTION

This introduction contains work from the article entitled "Generalized Kitaev spin liquid model and emergent twist defect" written by the author, Penghua Chen, and Shawn X. Cui published on Annals of Physics [2], and the article entitled "Ribbon operators in the generalized Kitaev quantum double model based on Hopf algebras" written by the author, Penghua Chen, and Shawn X. Cui published on Journal of Physics A [3].

People want quantum computers for different reasons. The original motivation was to simulate the quantum world, which requires an exponential amount of computational resources on a classical computer. On the other hand, since the factoring problem was shown to be solvable efficiently on a quantum computer [5], quantum computation has demonstrated the potential to dramatically reduce the computational time for certain problems compared to a classical computer. Shortly thereafter, effective simulation of quantum mechanics was proposed [6].

If we examine the architecture of a general computer, it consists of three major functional elements. The first is an encoder, which interprets information into a computable basis. This is followed by a functional unit, which applies actions or computations to the computational basis. Finally, a decoder is required to read out the desired information. While classical computers use binary strings as their computational basis, quantum computers utilize quantum states. As demonstrated in [7], quantum computers are much more error-prone than classical ones due to the fragility of quantum states, which can decohere under small but unavoidable perturbations or unexpected couplings. Fortunately, Shor argued that with a sufficiently low error rate, error-correcting codes provide a useful paradigm that enables reliable quantum computation [8].

One may ask if a fault-tolerant quantum computational paradigm could ever exist. We can "imagine" a scenario as follows. Suppose we have a nucleus at hand and define one quantum bit basis as follows: $|\ 0\rangle$ if it is a proton, and $|\ 1\rangle$ if it is a neutron. Such a basis would be exceptionally robust, as no error could change the state unless a nuclear reaction occurs. Thus, we can conclude that encoding information into particle types would be naturally fault-tolerant. The next question would be whether a "good" quantum gate

could exist. One might consider braiding to be fault-tolerant, as it is unaffected by local perturbations along the path and depends only on the topology of the particle trajectories.

Surely, the above imagination cannot be realized with elementary particles in our universe. Setting aside the question of whether a superposition of a proton and a neutron is physically meaningful, the braiding of elementary particles always results in ± 1, which is insufficient for computation. This raises a mathematical question: under what scenarios can a non-trivial representation of braiding group be realized?

Fortunately, this question is answered by anyon theories, which underpin topological quantum computation [9], [10]. Anyons, which are generalizations of bosons and fermions. Unitary matrices can be realized through the braiding of non-abelian anyons. Even more remarkable is that anyons appear as quasi-particle excitations in two-dimensional topological phases of matter, fundamentally representing a collective quantum state. This makes superpositioning them natural, thereby enabling the construction of computational quantum bits.

Finding a topological phase of matter is a major task for realizing topological quantum computation, and it is also an intriguing topic in its own right.

Two large classes of topological phases of matter are realized on lattice models. The Kitaev Quantum Double model achieves the realization of a vast class of anyon theories described by the representation category of the Drinfeld double of a group $\mathbf{G}$ [11]. Another important class of lattice models is the Levin-Wen model, which describes anyon theories characterized by the Drinfeld center of a fusion category [12]. The relationship between these two models is studied in [13]. It is conjectured that these two models are equivalent, which implies a generalization of the Kitaev Quantum Double model to the semisimple weak Hopf algebra case. A large class of similar models has also been studied [14]. The boundary and anyon condensation aspects are further investigated in [15]–[20]. Some researchers have explored how these models can be implemented as quantum memory [21]. The model has been extended to the C*-semisimple Hopf algebra case [22].

In Chapter 2, we extend this line of work by explicitly determining the structure of ribbon operators and pointing out the necessity of local orientation [3].

Anyon theories are well described by Unitary Modular Tensor Categories (UMTC) [23]. It can be proven that some of the non-Abelian cases support universal quantum computation. These theories have also been extensively studied from the perspective of topological quantum field theory [23]–[25]. For a good review on tensor categories, we recommend [26], [27].

Another interesting and exactly solvable model is the Kitaev Spin Liquid Model [4], which supports Abelian anyons in the gapped phase and non-Abelian anyons after opening a gap to the gapless phase. This model is simple yet fruitful and may be relatively easy to realize in real laboratories due to its two-body nearest-neighbor interactions.

Theoretically, numerous subsequent works have sought to generalize this model. For example, it has been explored on translationally invariant two-dimensional lattices with vertices of higher coordination numbers [28]–[30], on two-dimensional amorphous lattices [31], on three-dimensional diamond lattices [32], and on trivalent three-dimensional lattices [33]. These studies suggest that the gapless phase strongly depends on the geometric details of the lattice, challenging the conventional notion of a "topological" phase.

In Chapter 3, we will focus on the gapped phase, specifically the Toric Code in the original honeycomb model [4], and generalize it. We will demonstrate that the entire theory can be formulated on arbitrary planar lattices. The gapped phase of the model can be either the Toric Code model or a Toric Code with defects, as described in [34], which behaves as non-Abelian Ising anyons. Furthermore, we will show that there is a natural way to move these defects through time evolution.

The topological phase of matter is a special quantum phase that lies beyond Landau's symmetry-breaking paradigm [4]. The most well-known platform for realizing this phase is the Fractional Quantum Hall Effect [35]. For a comprehensive review, see [36]. This phase can support anyons as its quasi-particle excitations, contributing significantly to topological quantum computation. Furthermore, its ground state can serve as a quantum error-correcting code, as no local operator can have a non-trivial effect on the ground state.

One drawback of using the ground state of a topological phase of matter is the requirement to measure many-body syndrome operators, which is computationally expensive. Interestingly, the Kitaev spin liquid model can be treated as a subsystem code that requires

only two-body operators. For a review of subsystem codes, we recommend [37], [38]. Moreover, the honeycomb subsystem code has been "floquetified" in [39], exhibiting a non-trivial automorphism of the toric code. This approach has been further developed into the framework of dynamical automorphism codes [40], [41]. In Chapter 4, we present the construction of floquet $(n, 1)$ toric codes and floquet n-dimensional X-cube codes, which can be realized by coupling spin chains. The construction is localized, allowing it to be defined on general n-dimensional lattices.

It remains unclear how to precisely identify a topological phase. Topological entanglement entropy provides one way to characterize such phases [42], [43]. Significant efforts have been devoted to studying the properties of topological order [44]–[47].

An analysis shows the fragility of the 2D Toric Code under thermalization [48], which has motivated interest in three-dimensional topological phases. The Walker-Wang model was proposed from the perspective of topological quantum field theory [49], [50]. Additionally, there are a couple of 3D lattice models, such as the 3D Toric Code [51], 3D Color Code [52], and fracton codes [53]–[59].

Fracton models exhibit exotic topological phases of matter, where the ground state degeneracy depends not only on the topology of the underlying lattice but also on its size. The excitations in these models are highly constrained and cannot move freely, which contributes to their thermal stability. However, the application of 3D topological matter to the paradigm of topological quantum computation remains unclear. Nevertheless, these systems are of great theoretical interest.

2. RIBBON OPERATORS IN THE GENERALIZED KITAEV QUANTUM DOUBLE MODEL BASED ON HOPF ALGEBRAS

This chapter contains work from the article entitled "Ribbon operators in the generalized Kitaev quantum double model based on Hopf algebras" written by the author, Penghua Chen, and Shawn X. Cui published on Journal of Physics A [3].

2.1 Introduction

Topological phases of matter (TPM) in two spacial dimensions are gapped quantum liquids at low temperature that have robust ground state degeneracy, stable long-range entanglement, quasi-particle excitations (aka anyons), and possibly non-Abelian exchanging statistics. There exist global degrees of freedom encoded in the ground states which are resistant to local perturbations and which can be changed unitarily by non-trivial movements of quasi-particle excitations. These features make TPMs ideal quantum media to perform fault-tolerant quantum computing, namely, topological quantum computing [11] [60]. The theory of TPMs in 2D can be described equivalently by either a $(2+1)$ topological quantum field theory or a unitary modular tensor category.

A large class of TPMs in 2D are realized by spin lattice models. Among the most well known lies the toric code which is an Abelian toplogical phase and can also be described by a $\mathbb{Z}_2$ gauge theory. Toric code is a special example of Kitaev's quantum double models that associate to each finite group G an exactly solvable lattice model [11]. When G is $\mathbb{Z}_2$, the theory reduces to toric code. When G is a non-Abelian group, the model realizes a non-Abelian topological phase. In such models, anyon types correspond to irreducible representations of the Hopf algebra $D(G)$, the Drinfeld double (or, quantum double) of the group algebra $\mathbb{C}[G]$. The quantum double model can be generalized by replacing G with a semi-simple $\mathbb{C}^*$ Hopf algebra H. Given such a Hopf algebra, the authors in [61] wrote down a frustration-free Hamiltonian consisting of pairwise commuting local projectors analogous to the original setup. We call this model the generalized Kitaev quantum double model[1].

[1]↑This model can be further generalized to a semi-simple weak Hopf algebra [62]. We will not discuss this generalization in this paper.

Another class of realizations are the Levin-Wen string-net models [12] based on unitary fusion categories. String-net models and the quantum double models are closely related. Specifically, for a Hopf algebra H, it was shown that the generalized quantum double model based on H is equivalent to the string-net model based on $\mathrm{Rep}(H)$, the category of representations of H [63] [64].

A key tool to describe the creation/annihilation and movement of anyons in the models mentioned above is the notion of ribbon operators (or string operators). In toric code, these are a string of Pauli Z operators on the lattice or a string of Pauli X operators on the dual lattice. However, when the group G is non-Abelian, these two types of string operators have to be 'entangled'; one has to consider a thickened string of operators, namely, operators on a ribbon. Roughly, a ribbon is a strip in the lattice with one side running along edges of the lattice and the other side along edges of the dual lattice. In the quantum double model, one first defines the operators for two types of elementary ribbons (triangles), and then extend the definition to longer ribbons using an induction (see [11] [65] for details). In [61], it was stated briefly without proofs that ribbon operators in the generalized quantum double model can also be defined in a similar way.

In this paper, we rigorously define ribbon operators in the generalized quantum double model based on a semi-simple $\mathbb{C}^*$ Hopf algebra, and systemically study their properties. It is illustrated that the ribbon operators can be interpreted as representations of $D(H)^*$ or $D(H)^{*,\mathrm{op}}$, where $D(H)$ is the Drinfeld double of H. We also prove explicitly that, given a ribbon, the ribbon operators on it commute with all terms in the Hamiltonian except for those associated with the two ends of the ribbon. Hence, ribbon operators create excitations only at their ends. For a ribbon τ, denote by V_τ the space of states obtained by ribbon operators on τ acting on the ground state. V_τ is the space of 2-point excitations where the excitations lie at the ends of τ. It is shown that V_τ is naturally isomorphic to $D(H)^*$. Moreover, local operators at the ends of τ act on V_τ by regular representations of $D(H)$. It follows that elementary excitation types are in one-to-one correspondence to irreducible representations of $D(H)$. Although these properties are as anticipated, and hence may not be surprising to experts, the computations involved in proving them turn out to be significantly more

complicated than those in the case of finite groups. This is partly due to the complications in dealing with general Hopf algebras rather than just group algebras.

Furthermore, we reveal some subtleties in the definition of ribbon operators. In the literature (e.g., [11], [65]), only two types of elementary ribbons are considered, the direct triangle and the dual triangle. For instance, in Figure 2.1, I and III are direct triangles, while II and IV are dual triangles. However, we show in Section 2.3.2 that I and III have to be treated differently when defining operators on them, and so do II and IV. The point is that there is a property, which we call *local orientation*, that distinguishes each pair of the above triangles. For instance, II is locally clockwise while IV is locally counterclockwise. Local orientation can also be extended to general ribbons. As a consequence, there will be two types of ribbons according to their local orientation, and the definition of ribbon operators on each type has to be different. If we were not to distinguish these two types of ribbons, certain common properties to be expected would not hold. For example, the ribbon operator would fail to commute with terms of the Hamiltonian away from the end points. Surprisingly, we point out that this issue already exists even in the original quantum double model when the input group is non-Abelian, but this issue seems to not have been addressed in the literature to the best of our knowledge. Lastly, our definition of ribbon operators is explicit, in contrast to those in the string-net models where one needs to solve a set of consistency equations.

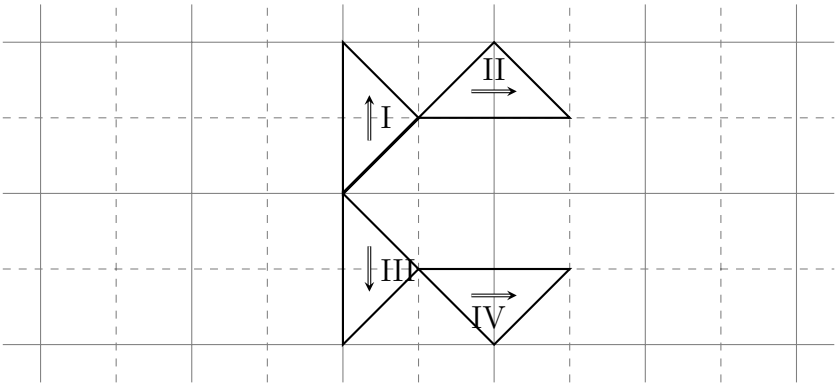

Figure 2.1. An illustration of elementary ribbons (dark solid triangles). The solid grid represents the lattice and the dashed grid represents the dual lattice.

The rest of the paper is organized as follows. In Section 2.2, we collect some basic facts about semi-simple Hopf algebras, their representations, and Drinfeld double. We also review the Hamiltonian of the generalized quantum double model. In Section 2.3, we carefully formulate ribbons, provide the definition of ribbon operators, and study their properties. In particular, it is shown in Section 2.3.3 that local orientation needs to be considered even in the original Kitaev model with a non-Abelian group. Many of technical details can be found in the appendices.

2.2 Background

2.2.1 Hopf algebra

Hopf algebras are important objects in a number of areas, such as representation theory, tensor categories, algebraic topology, topological quantum field theories, etc. There is an extensive literature covering different aspects of Hopf algebras. In this section, we simply provide a brief review with the main purpose of fixing conventions. For detailed discussions, see for instance [66] [67].

A Hopf algebra over $\mathbb{C}$ is a vector space H endowed with the linear maps (called structure maps),

$$\mu\colon H\otimes H\to H, \qquad \eta\colon \mathbb{C}\to H, \tag{2.1}$$

$$\Delta\colon H\to H\otimes H, \qquad \epsilon\colon H\to \mathbb{C}, \tag{2.2}$$

$$S\colon H\to H, \tag{2.3}$$

satisfying several conditions to be specified in the following.

Firstly, (μ,η) defines an (associative) algebra structure. That is, the multiplication μ is associative:

$$\mu\left[\mu(a\otimes b)\otimes c\right]=\mu\left[a\otimes\mu(b\otimes c)\right], \tag{2.4}$$

or briefly

$$(ab)c=a(bc). \tag{2.5}$$

The unit 1_H for the multiplication μ is given by $\eta(1)$. Secondly, (Δ, ϵ) defines a (coassociative) coalgebra structure with Δ and ϵ the comultiplication and counit, respectively. We will use the *Sweedler notation* for expressions involving comultiplications. For instance, we write

$$\Delta(a) = \sum_{(a)} a' \otimes a''. \tag{2.6}$$

The comultiplication map being coassociative means

$$(\Delta \otimes id) \circ \Delta = (id \otimes \Delta) \circ \Delta, \tag{2.7}$$

or in Sweedler notation,

$$\sum_{(a)} \left[\sum_{(a')} (a')' \otimes (a')'' \right] \otimes a'' = \sum_{(a)} a' \otimes \left[\sum_{(a'')} (a'')' \otimes (a'')'' \right]. \tag{2.8}$$

Due to the above equality, we simply write

$$(\Delta \otimes id) \circ \Delta(a) = \sum_{(a)} a' \otimes a'' \otimes a''', \tag{2.9}$$

or

$$(\Delta \otimes id) \circ \Delta(a) = \sum_{(a)} a^{(1)} \otimes a^{(2)} \otimes a^{(3)}. \tag{2.10}$$

More generally, we use the Sweedler notation for

$$(\Delta \otimes id_{H^{\otimes(n-2)}}) \circ \cdots \circ (\Delta \otimes id) \circ \Delta(a) = \sum_{(a)} a^{(1)} \otimes \cdots \otimes a^{(n)}. \tag{2.11}$$

The counit ϵ satisfies

$$\sum_{(a)} \epsilon(a') a'' = \sum_{(a)} a' \epsilon(a'') = a. \tag{2.12}$$

Thirdly, Δ and ϵ are both required to be algebra morphisms. In particular, this implies ϵ defines a 1-dimensional representation of H. Lastly, S is called the antipode which is invertible in our consideration satisfying:

$$\sum_{(a)} a' S(a'') = \epsilon(a) 1_H = \sum_{(a)} S(a') a''. \tag{2.13}$$

To emphasize on structure maps, we also denote a Hopf algebra by

$$(H; \mu, \eta, \Delta, \epsilon, S). \tag{2.14}$$

In this paper, we will only consider finite dimensional semisimple Hopf algebras. Over $\mathbb{C}$, semisimplicity is equivalent to the condition that S is involutory, namely, $S^2 = id$. The following identities are implied in a finite dimensional Hopf algebra.

$$S(ab) = S(b)S(a), \quad S(1_H) = 1_H, \quad \epsilon[S(a)] = \epsilon(a), \tag{2.15}$$

$$\sum_{(a)} S(a'') \otimes S(a') = \sum_{(S(a))} S(a)' \otimes S(a)''. \tag{2.16}$$

Given a Hopf algebra $(H; \mu, \eta, \Delta, \epsilon, S)$, there are several ways of constructing new Hopf algebras out of it. Take H^* to be the linear dual of H. Then

$$(H^*; \Delta^T, \epsilon^T, \mu^T, \eta^T, S^T), \tag{2.17}$$

defines a Hopf algebra structure on H^*, where for a map f, f^T means the linear dual of f.[2] For example, μ^T is a map from H^* to $H^* \otimes H^*$:

$$\mu^T(f)(a \otimes b) = f\left[\mu(a \otimes b)\right] = f(ab). \tag{2.18}$$

[2]↑Another common notation for f^T is f^*. Here we use f^T since under appropriate bases, the matrix of f^T is the transpose of that of f. Another reason is to avoid confusion since we will introduce a $*$ operation below with a different meaning.

where $a, b \in H$, and $f \in H^*$. We can also define the opposite Hopf algebra H^{op} by

$$(H^{op}; \mu^{op}, \eta, \Delta, \epsilon, S^{-1}), \tag{2.19}$$

where H^{op} as a vector space is the same as H, and μ^{op} is defined as

$$\mu^{op}(a \otimes b) = \mu(b \otimes a) = ba. \tag{2.20}$$

Similarly, we have the co-opposite Hopf algebra H^{cop},

$$(H^{cop}; \mu, \eta, \Delta^{cop}, \epsilon, S^{-1}), \tag{2.21}$$

where again H^{cop} as a vector space is H, and Δ^{cop} is defined as

$$\Delta^{cop}(a) = \sum_{(a)} a'' \otimes a'. \tag{2.22}$$

The above three operations $(\cdot)^*$, $(\cdot)^{op}$, and $(\cdot)^{cop}$ are all involutive, and can also be composed with each other. It is direct to check that as Hopf algebras $(H^*)^{cop} \simeq (H^{op})^*$ and $(H^*)^{op} \simeq (H^{cop})^*$.

For a semisimple Hopf algebra H, a (two-sided) integral is an element $h_0 \in H$ such that for all $a \in H$,

$$ah_0 = h_0 a = \epsilon(a) h_0. \tag{2.23}$$

The space of integrals is a 1-dimensional subspace, and hence h_0 is uniquely defined if we require

$$h_0^2 = h_0, \quad \text{or equivalently} \quad \epsilon(h_0) = 1. \tag{2.24}$$

We call such an h_0 the Haar integral of H. It can be proved that h_0 is cocommutative, namely

$$\Delta(h_0) = \sum_{(h_0)} h_0' \otimes h_0'' = \sum_{(h_0)} h_0'' \otimes h_0'. \tag{2.25}$$

To make a Hopf algebra into a Hilbert space, we introduce the $*$-structure. A $*$-structure on H is a conjugate-linear map $* : H \to H$ satisfying the following properties:

$$(a^*)^* = a, \quad (ab)^* = b^*a^*, \quad 1^* = 1, \tag{2.26}$$

$$\sum_{(a)} (a')^* \otimes (a'')^* = \sum_{(a^*)} (a^*)' \otimes (a^*)''. \tag{2.27}$$

A Hopf algebra endowed with a $*$-structure is called a $\mathbb{C}^*$ Hopf algebra. Let H be such a Hopf algebra, and denote by ϕ the Haar integral of H^*. For $a, b \in H$, define

$$\langle a, b \rangle = \phi(a^*b). \tag{2.28}$$

The above form $\langle \cdot, \cdot \rangle$ defines a Hermitian inner product on H.

Unless otherwise stated, throughout this paper we will, as a convention, use letters such as h_0, ϕ for the Haar integrals, a, b, c, x, y for general elements of H, and f, g, t for general elements of H^*. We adopt the notation that $f(x?)$ is an element of H^* such that $f(x?)(y) = f(xy)$.

2.2.2 Representations of semisimple Hopf algebras

The category of finite dimensional representations over $\mathbb{C}$ of a semisimple Hopf algebra H is a semisimple tensor category with duals. If V, W are two representations,

$$\rho_V : H \to \mathrm{End}(V), \tag{2.29}$$

$$\rho_W : H \to \mathrm{End}(W), \tag{2.30}$$

then $V \otimes W$ is a representation with the action given by,

$$a.(v \otimes w) := \Big((\rho_V \otimes \rho_W)\Delta(a)\Big)(v \otimes w), \quad a \in H, v \in V, w \in W, \tag{2.31}$$

and so is V^* with the action given by,

$$a.f := f \circ \rho_V(S(a)), \quad a \in H, f \in V^*. \tag{2.32}$$

A representation V of H is irreducible if $\mathrm{End}_H(V) \simeq \mathbb{C}$. Denote by Irr_H the set of isomorphism classes of irreducible representations of H. Consider the regular representation H with the action given by left multiplication,

$$L(a)(c) := ac, \tag{2.33}$$

or by right multiplication by $S(\cdot)$,

$$R(a)(c) := cS(a). \tag{2.34}$$

These two actions commute and hence define an action of $H \otimes H$ on H by,

$$(a \otimes b).c := acS(b). \tag{2.35}$$

It is a basic fact that as a representation of $H \otimes H$, we have the isomorphism,

$$H \simeq \bigoplus_{\mu \in \mathrm{Irr}_H} \mu^* \otimes \mu. \tag{2.36}$$

An explicit isomorphism is given as follows. For each $\mu \in \mathrm{Irr}_H$, fix a basis $\{|\ i\rangle \ \mid \ i = 1, \cdots, dim(\mu)\}$, and denote the matrix of an element $a \in H$ under this basis by $D^\mu(a)$. Let $h_0 \in H$ be the Haar integral (see Equations 2.23, 2.24). We define the 'Fourier transformation' on H by [64],

$$|\ \nu ij\rangle = \sqrt{\frac{dim(\nu)}{dim(H)}} \sum_{(h_0)} D^\nu(h_0')_{ij} h_0'', \tag{2.37}$$

where $\nu \in \mathrm{Irr}_H$, and $i, j = 1, 2, \cdots, dim(\nu)$. For self-containedness, in Appendix A.6, we verify that the action of $H \otimes H$ on the subspace $\mathrm{span}\{|\ \nu ij\rangle \ \mid \ i, j = 1, \cdots, dim(\nu)\}$ is given by $\nu^* \otimes \nu$, and hence defines a desired isomorphism for Equation 2.36.

Lastly, the two representations L and R each induce a representation of H on H^*,

$$L(a) \mid f\rangle = \mid f[S(a)?]\rangle, \tag{2.38}$$

$$R(a) \mid f\rangle = \mid f(?a)\rangle, \quad |f\rangle \in H^*. \tag{2.39}$$

2.2.3 Drinfeld double of Hopf algebras

The Drinfeld double (or quantum double) $D(H)$ of a Hopf algebra H is a Hopf algebra

$$D(H) = \Big((H^*)^{cop} \otimes H; \mu_D, \eta_D, \Delta_D, \epsilon_D, S_D\Big). \tag{2.40}$$

It is constructed as a bicrossed product of H and $(H^*)^{cop}$. For $f, g \in H^*$, $a, b \in H$, μ_D is defined as

$$\mu_D\left[(f \otimes a) \otimes (g \otimes b)\right] = \sum_{(a)} f\, g\left[S^{-1}(a''')?a'\right] \otimes a''b, \tag{2.41}$$

which is known as the *straightening equation*. Notice that we have

$$f \otimes a = (f \otimes 1)(1 \otimes a). \tag{2.42}$$

The other structure maps can be determined by the property that $(H^*)^{cop}$ and H are both sub Hopf algebras of $D(H)$ by the inclusions $f \mapsto f \otimes 1$ and $a \mapsto \epsilon \otimes a$, respectively. For example, Δ_D is given by,

$$\Delta_D(f \otimes a) = \sum_{(f),(a)} (f'' \otimes a') \otimes (f' \otimes a''), \tag{2.43}$$

where in the Sweedler notation of f, we treat f as an element of H^* rather than $(H^*)^{cop}$. We will also use this convention throughout the paper. Namely, for $a \in H^{cop}$, as far as the Sweedler notation is concerned, we use Δ rather than Δ^{cop} to define a', a'', etc. Other structure maps are provided as follows,

$$\eta_D(1) = \epsilon \otimes 1, \tag{2.44}$$

$$\epsilon_D(f \otimes a) = f(1) \otimes \epsilon(a), \tag{2.45}$$

$$S_D(f \otimes a) = S(a)S^T(f). \tag{2.46}$$

2.2.4 Generalized Kitaev model based on Hopf algebras

In this subsection, H denotes a semisimple $\mathbb{C}^*$ Hopf algebra. The original Kitaev model [11] is constructed based on the group algebra $\mathbb{C}[G]$ of a finite group G while the generalized Kitaev model is based on a semisimple $\mathbb{C}^*$ Hopf algebra H. The latter is introduced in [61] which we review below.

For simplicity, we take a square lattice $\Gamma = (V, E, P)$ to establish the model, where V, E, and P denote the set of vertices, (directed) edges, and faces, respectively, as shown in Figure 2.2 (the solid grid)[3]. We also define the dual lattice $\Gamma^* = (P^*, E^*, V^*)$ where P^* is the set of vertices in Γ^* dual to the faces P in Γ, and E^* and V^* have similar interpretations. For an element $x \in V \cup E \cup P$, denote by x^* the corresponding element in $V^* \cup E^* \cup P^*$. For an edge $e \in E$, the direction of the dual edge e^* is obtained by rotating the direction of e counterclockwise by 90°. A **site** $s = (v, p)$ is a pair of a vertex v and an adjacent face p containing v. We draw a segment connecting v and the dual vertex $p*$ to represent the site. See Figure 2.2.

To each edge e of Γ, we attach a copy of the Hopf algebra (also a Hilbert space) $\mathcal{H}_e := H$. The total Hilbert space of the model is the tensor product over all edges of the associated Hilbert spaces:

$$\mathcal{H} := \bigotimes_{e \in E} \mathcal{H}_e. \tag{2.47}$$

$$L^a_+(x) = ax, \quad L^a_-(x) = xS(a). \tag{2.48}$$

$$T^f_+(x) = f(x'')x', \quad T^f_-(x) = f[S(x')]x''. \tag{2.49}$$

Upon the establishment of the oriented graph $\Gamma = (V, E, P)$, we can define the edge operators [61] illustrated in Figure 2.2 and the local operators $A_a(s)$ and $B_f(s)$ on a site

[3]↑The edges in the lattice can be arbitrarily directed, and the physics of the model will be independent of those directions.

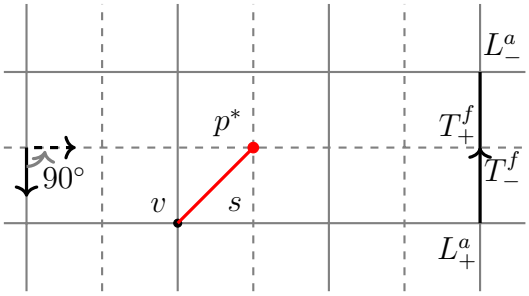

Figure 2.2. The solid grid connecting all vertices V represents the square lattice Γ, while the dashed grid connecting all dual vertices P^* represents the dual square lattice Γ^*. A site $s = (v, p)$ is represented by a segment connecting a vertex v and a dual vertex p^*. For $f \in H^*, a \in H$, the edge operators $T^f_\pm$ and $L^a_\pm$ act on the Hilbert space $\mathcal{H}_e$ of an edge e.

$s = (v, p)$ illustrated in Figure 2.3 and Figure 2.4, respectively. For each edge e of the lattice and for $f \in H^*, a \in H$, the edge operators $T^f_\pm$ and $L^a_\pm$ act on the Hilbert space $\mathcal{H}_e$. See Equations 2.48-2.49.

To define $A_a(s)$ for $a \in H$, we start from the site s, go around the vertex v to apply edge operators $L^{a'}_\pm$, $L^{a''}_\pm$, $L^{a'''}_\pm$, $L^{a^{(4)}}_\pm$ to each edge adjacent to v in counterclockwise order as shown and explained in Figure 2.3. For example, when it is applied to the product state of $|\, x_1\rangle$, $|\, x_2\rangle$, $|\, x_3\rangle$, $|\, x_4\rangle$ for the configuration in Figure 2.3, the result is

$$A_a(s) \,|\, x_1\rangle \,|\, x_2\rangle \,|\, x_3\rangle \,|\, x_4\rangle = \sum |\, a' x_1\rangle \,|\, a'' x_2\rangle \,|\, a''' x_3\rangle \,|\, a^{(4)} x_4\rangle. \tag{2.50}$$

$$A_a(s) = \sum L^{a'}_+ \otimes L^{a''}_+ \otimes L^{a'''}_+ \otimes L^{a^{(4)}}_+ \tag{2.51}$$

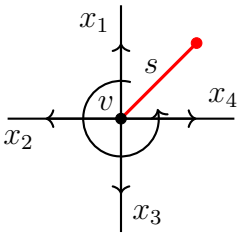

Figure 2.3. The convention for the local operator $A_a(s)$: for each edge, we choose $+$ sign for the edge operator $L^{a^{(n)}}$ if the edge leaves the vertex, and choose $-$ sign otherwise.

To define $B_f(s)$, $f \in H^*$, we start from the site s, go around the dual vertex p^* to apply edge operators $T_{\pm}^{f'}$, $T_{\pm}^{f''}$, $T_{\pm}^{f'''}$, $T_{\pm}^{f^{(4)}}$ to the edges on the boundary of p in counterclockwise order as shown and explained in Figure 2.4. When it is applied to the product state of $|\, x_1\rangle$, $|\, x_2\rangle$, $|\, x_3\rangle$, $|\, x_4\rangle$ for the configuration of Figure 2.4, the result is [4]

$$B_f(s) \mid x_1\rangle \mid x_2\rangle \mid x_3\rangle \mid x_4\rangle = \sum f(x_1'' x_2'' x_3'' x_4'') \mid x_1'\rangle \mid x_2'\rangle \mid x_3'\rangle \mid x_4'\rangle. \tag{2.52}$$

$$B_f(s) = \sum T_+^{f'} \otimes T_+^{f''} \otimes T_+^{f'''} \otimes T_+^{f^{(4)}} \tag{2.53}$$

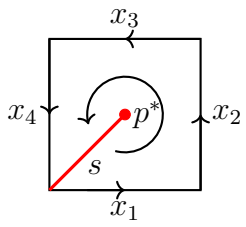

Figure 2.4. The convention for the local operator $B_f(s)$: for each edge, we choose $+$ sign for the edge operator $T^{f^{(n)}}$ if the direction of the edge coincides with the counterclockwise orientation of the boundary of p, and choose $-$ sign otherwise.

Remark 2.2.1. We remark that our convention for defining the operators $A_a(s)$ and $B_f(s)$ is opposite to that in [11] [61]. Explicitly, these operators on a lattice Γ will be the same as those of [61] on a lattice Γ' obtained from Γ by reversing the orientation of all edges. When the Hopf algebra is a group algebra, our convention is consistent with that in [65].

For each site $s = (v, p)$, we extend the definition of $A_a(s)$, $B_f(s)$ to the whole Hilbert space $\mathcal{H}$ by tensoring the identity operator on edges not adjacent to v or p. The $A_a(s)$ and $B_f(s)$ are called local operators at s. They define a representation of the Drinfeld double $D(H)$ by mapping $f \otimes a$ to $B_f A_a$. The most nontrivial part of the statement is the straightening equation. For self containedness, we verify the straightening equation for the local operators in Appendix A.1.

Let $h_0 \in H$ and $\phi \in H^*$ be the Haar integral. For a site $s = (v, p)$, it can be checked that $A_{h_0}(v) := A_{h_0}(s)$ only depends on v and $B_\phi(p) := B_\phi(s)$ only depends on p. Moreover, the

[4]↑To derive Equation 2.52, we use the fact that the comultiplication Δ_* in H^* is actually μ^T.

set of operators $\{A_{h_0}(v) \ : \ v \in V\} \cup \{B_\phi(p) \ : \ p \in P\}$ are mutually commuting projectors. The (frustration-free) Hamiltonian of the model is given by,

$$H = -\sum_{v \in V} A_{h_0}(v) - \sum_{p \in P} B_\phi(p). \tag{2.54}$$

The ground states are simultaneously stabilized by all the terms in the Hamiltonian. Equivalently, the ground states space can be characterized as the subspace of $\mathcal{H}$ corresponding to the trivial representation of $D(H)$ on all sites s.

2.3 Ribbon operators

In this section, we rigorously define ribbons, operators on them called ribbon operators, and study some of their important properties.

2.3.1 Directed ribbons

Let $s_0 = (v_0, p_0)$ and $s_1 = (v_1, p_1)$ be two distinct sites that share a common vertex (i.e., $v_0 = v_1$) or a common dual vertex (i.e., $p_0 = p_1$). There is a unique triangle τ whose sides are given by s_0, s_1, and an edge e_τ in the lattice or the dual lattice. See the bottom left two examples in Figure 2.5. The triangle τ is said to be of dual (resp. direct) **type** if e_τ is an edge in the dual (resp. direct) lattice, or equivalently, if $v_0 = v_1$ (resp. $p_0 = p_1$). We also assign a direction to τ, indicated by a double arrow inside the triangle, so that it points from s_0 to s_1. Denote by $s_i = \partial_i \tau, \ i = 0, 1$. A *ribbon* is a sequence of mutually non-overlapping directed triangles $\tau = \tau_1 \tau_2 \cdots \tau_n$ such that $\partial_1 \tau_i = \partial_0 \tau_{i+1}, \ i = 1, \cdots, n-1$. Note that τ inherits a direction from its components, also indicated by a double arrow, and we call $\partial_0 \tau := \partial_0 \tau_1$ the initial site and $\partial_1 \tau := \partial_1 \tau_n$ the terminal site of τ. See Figure 2.5 for an illustration of several ribbons. By default, all ribbons are directed. A closed ribbon is one for which the initial site and terminal site coincide. Unless otherwise stated, ribbons considered in this paper are not closed. Triangles are called elementary ribbons.

We introduce a property, called **local orientation**, of directed ribbons which seems to be missing in the literature, but will turn out to be critical to coherently define ribbon operators.

Definition 2.3.1. *Let τ be a directed triangle (of dual or direct type) with initial site $s_0 = \partial_0\tau = (v_0, p_0)$. Then τ has clockwise (resp. counterclockwise) local orientation if a clockwise (resp. counterclockwise) rotation of s_0 around p_0^* immediately swipes through the interior of τ. We draw a clockwise/counterclockwise arrow around p_0^* to denote the local orientation of τ (See Figure 2.5).*

An intuitive motivation for introducing local orientation is as follows. We can see that for a triangle of a given type, a choice of direction is not sufficient to uniquely determine the shape of the triangle. For example, the triangles II and IV in Figure 2.5 are both of dual type and directed to the right, but IV is an 'upside down' version of II, and as will be shown later, they have to be treated differently when we define ribbon operators on them. Local orientation can be used to distinguish those two since triangle II is locally clockwise while IV is locally counterclockwise.

It is straightforward to see that changing the direction of a triangle will also change its local orientation. We note that a choice of direction is a *structure* on the triangle, while the type and local orientation are each a *property* of a directed triangle (though only the later depends on the direction). Thus, there are four classes of directed triangles according to different combinations of local orientation and type. In Figure 2.5, the triangles I-IV in increasing order are, respectively, clockwise direct, clockwise dual, counterclockwise direct, and counterclockwise dual.

Now let τ be a general directed ribbon. Clearly, its composite triangles can have different types (direct or dual). However, an important observation is that all of the triangles of τ must have the same local orientation. Hence, we can extend the notion of local orientation from triangles to general ribbons. Intuitively, if a ribbon aligns horizontally and directs from left to right, then turning it upside down will change its local orientation while keeping its direction. Reversing the direction alone will flip its local orientation as well. As a notation,

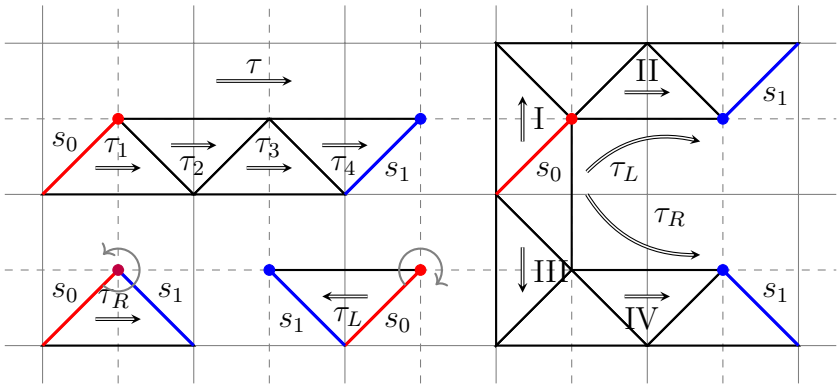

Figure 2.5. A ribbon τ is composed of triangles τ_i $(i = 1, 2 \cdots n)$ with a direction from s_0 to s_1. A triangle is a component of a ribbon with inherited direction and also the shortest ribbon.

we also denote a directed ribbon by τ_L if it is locally clockwise and by τ_R if it is locally counterclockwise. (This notation is motivated by the left/right hand rule)

2.3.2 Definition of ribbon operators

For a directed ribbon τ and $h \otimes f \in H \otimes H^*$, we will define the ribbon operator $F^{h \otimes f}(\tau)$, also written as $F^{(h,f)}(\tau)$. The operators will act on the whole Hilbert space $\mathcal{H}$, but the action is non-trivial only on the edges contained in τ. Explicitly, for an elementary ribbon τ, let $\mathcal{H}_\tau := \mathcal{H}_{e_\tau}$ if τ is direct, and $\mathcal{H}_\tau := \mathcal{H}_{e_\tau^*}$ otherwise. For a general ribbon τ, decompose $\tau = \tau_1 \sqcup \tau_2$ so that $\partial_1 \tau_1 = \partial_0 \tau_2$ and define inductively $\mathcal{H}_\tau := \mathcal{H}_{\tau_1} \otimes \mathcal{H}_{\tau_2}$. Then $F^{(h,f)}(\tau)$ will only act non-trivially on the space $\mathcal{H}_\tau$. The definition of ribbon operators below is motivated by [11] [65] for group algebras and by [61] for Hopf algebras. However, none of the above references addresses the critical issue of local orientation, as to be discussed later.

First, assume τ is an elementary directed ribbon, i.e., a triangle. There are four cases depending on its type and local orientation. Also, recall that the edges in the lattice as well as those in the dual lattice are directed. The direction of the edge e_τ and that of τ can be either parallel or opposite. Taking this into consideration, we distinguish eight cases in Equations 2.55a-2.55h, where Equations $(a) - (d)$ correspond to locally clockwise triangles and $(e) - (h)$ locally counterclockwise triangles.

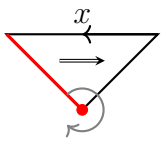

$$F^{(h,f)}(\tau_L) \mid x\rangle = \sum_{(x)} \epsilon(h) f[S(x'')] \mid x'\rangle \tag{2.55a}$$

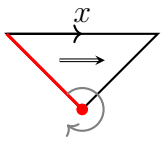

$$F^{(h,f)}(\tau_L) \mid x\rangle = \sum_{(x)} \epsilon(h) f(x') \mid x''\rangle \tag{2.55b}$$

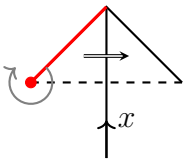

$$F^{(h,f)}(\tau_L) \mid x\rangle = \epsilon(f) \mid xS(h)\rangle \tag{2.55c}$$

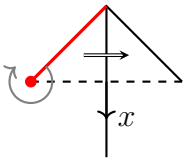

$$F^{(h,f)}(\tau_L) \mid x\rangle = \epsilon(f) \mid hx\rangle \tag{2.55d}$$

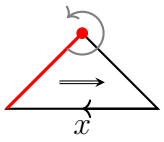

$$F^{(h,f)}(\tau_R) \mid x\rangle = \sum_{(x)} \epsilon(h) f[S(x')] \mid x''\rangle \tag{2.55e}$$

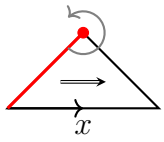

$$F^{(h,f)}(\tau_R) \mid x\rangle = \sum_{(x)} \epsilon(h) f(x'') \mid x'\rangle \tag{2.55f}$$

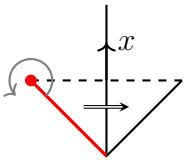

$$F^{(h,f)}(\tau_R) \mid x\rangle = \epsilon(f) \mid S(h)x\rangle \tag{2.55g}$$

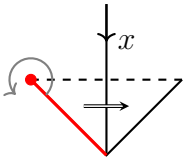

$$F^{(h,f)}(\tau_R) \mid x\rangle = \epsilon(f) \mid xh\rangle \tag{2.55h}$$

For ribbons other than elementary triangles, we define the ribbon operators inductively. Let τ be an arbitrary ribbon. Decompose τ as $\tau = \tau_1 \sqcup \tau_2$, where the terminal site of τ_1 matches the initial site of τ_2, and they are disjoint otherwise. For $h \otimes f \in H \otimes H^*$, define

$$F^{h,f}(\tau) := \sum_{i,(i),(h)} F^{h',g_i}(\tau_1) F^{S(i''')h''i',f(i''?)}(\tau_2), \tag{2.56}$$

where $\{i\}$ is an orthogonal complete basis of H, and $g_i = \langle i, \ \rangle$ is the corresponding functional in H^*. The above definition is explicit, but a more intuitive way is as follows. For an element $h \otimes f \in D(H)^* \simeq H \otimes H^*$ where the isomorphism denotes a linear isomorphism between vector spaces,

$$\Delta(h \otimes f) = \sum_{(h \otimes f)} (h \otimes f)' \otimes (h \otimes f)''. \tag{2.57}$$

We apply the expansion to the construction of ribbon operators as

$$F^{h \otimes f}(\tau) := \sum_{(h \otimes f)} F^{(h \otimes f)'}(\tau_1) F^{(h \otimes f)''}(\tau_2). \tag{2.58}$$

It can be checked that Equations 2.56 and 2.58 are equivalent. The ribbon operators do not depend on how the ribbon is partitioned into shorter ones due to the coassociativity of the comultiplication in Hopf algebras.

2.3.3 Local orientation in original Kitaev model

In this subsection, we show that the distinction of local orientation is already necessary in the orignal Kitaev model. Note that, from Equations 2.55, $F^{(h,f)}(\tau)$ does not distinguish local orientations on direct triangles if H is cocommutative, and it does not distinguish local orientations on dual triangles if H is commutative. In particular, if H is the group algebra of an Abelian group (e.g., toric code), then local orientations are redundant. On the other hand, for the group algebra of a non-Abelian group in the original Kitaev model, the two local orientations on a dual triangle should support different ribbon operators according to our definitions. This distinction, however, has not been addressed in the literature, to the best of our knowledge. In [11], [65], the definition of ribbon operators on triangles coincide with that presented in Equations 2.55*a*-2.55*d* corresponding to locally clockwise orientation. We show below with an explicit example that ignoring local orientations can cause certain properties to fail.

For the rest of the subsection, let $H = \mathbb{C}[G]$ be the group algebra of a non-Abelian group G. Equation 2.59 is a commutation relation that is expected to hold between ribbon operators and plaquette operators, where s_0 is the initial site of a ribbon τ (see Equation (B42) in [65]), and $t, h, g \in G$.

$$B_t(s_0)F^{h,g}(\tau) = F^{h,g}(\tau)B_{th}(s_0). \tag{2.59}$$

In fact, we just need the above identity to hold when both sides act on the ground state.

Take τ to be the ribbon shown in Figure 2.6, which is a dual triangle and has locally counterclockwise orientation. In Appendix A.2, we show in detail that Equation 2.59 fails for τ and any other ribbon that starts with τ if we use the old definition of ribbon operators on them. By recognizing τ with locally counterclockwise orientation and using the new

definition (Equation 2.55g), we can resolve the issue, and obtain the following commutation relation,

$$B_t(s_0)F^{h,g}(\tau) = F^{h,g}(\tau)B_{ht}(s_0), \tag{2.60}$$

which is equivalent to Equation 2.59 when acting on the ground state since $\delta_{ht,e} = \delta_{th,e}$.

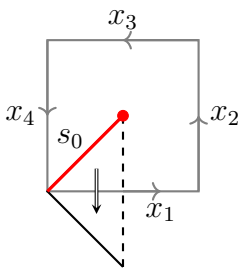

Figure 2.6. A counter-example of a ribbon for which Equation 2.59 fails in the original Kitaev model.

2.3.4 Properties of ribbon operators

In this section, we establish a few properties of ribbon operators. Recall that the ribbon operators $F^{h,f}(\tau)$ only act non-trivially on the Hilbert space $\mathcal{H}_\tau$.

Proposition 2.3.1. *Let τ_L and τ_R be a locally clockwise and a locally counterclockwise ribbon, respectively. Then,*

$$F^{h_1,f_1}(\tau_L) \cdot F^{h_2,f_2}(\tau_L) = F^{h_1h_2,f_2f_1}(\tau_L), \tag{2.61}$$

$$F^{h_1,f_1}(\tau_R) \cdot F^{h_2,f_2}(\tau_R) = F^{h_2h_1,f_1f_2}(\tau_R). \tag{2.62}$$

In another words, the operators $F^{h,f}(\tau)$ define a representation of $D(H)^{*,op}$ on $\mathcal{H}_\tau$ if τ is locally clockwise, and a representation of $D(H)^*$ if τ is locally counterclockwise.

Proof. In Appendix A.3, we show in details that the above two equations hold for elementary ribbons. Then it can be proved inductively that they also hold for general ribbons using the compatibility condition between multiplication and comultiplication in a Hopf algebra.

Notice that $D(H)^{*,op}$ and $D(H)^*$ share the same comultiplication. Below we only give the proof for τ_R since that of the other case is similar.

Let τ_R be a locally counterclockwise ribbon. Assume Equation 2.62 holds for any ribbon whose length is shorter than that of τ_R. Decompose τ_R as $\tau_R = \tau_1 \sqcup \tau_2$ such that $\partial_1\tau_1 = \partial_0\tau_2$. Then,

$$
\begin{aligned}
& F^{h_1\otimes f_1}(\tau_R)\cdot F^{h_2\otimes f_2}(\tau_R) \\
=& \sum_{(h_1\otimes f_1)} F^{(h_1\otimes f_1)'}(\tau_1)F^{(h_1\otimes f_1)''}(\tau_2) \ \cdot \sum_{(h_2\otimes f_2)} F^{(h_2\otimes f_2)'}(\tau_1)F^{(h_2\otimes f_2)''}(\tau_2) \\
=& \sum_{(h_1\otimes f_1)}\sum_{(h_2\otimes f_2)} F^{(h_1\otimes f_1)'}(\tau_1)F^{(h_2\otimes f_2)'}(\tau_1)\ F^{(h_1\otimes f_1)''}(\tau_2)F^{(h_2\otimes f_2)''}(\tau_2) \\
=& \sum_{(h_1\otimes f_1)}\sum_{(h_2\otimes f_2)} F^{(h_1\otimes f_1)'(h_2\otimes f_2)'}(\tau_1)\ F^{(h_1\otimes f_1)''(h_2\otimes f_2)''}(\tau_2) \\
=& \sum_{(h_2h_1\otimes f_1f_2)} F^{(h_2h_1\otimes f_1f_2)'}(\tau_1)\ F^{(h_2h_1\otimes f_1f_2)''}(\tau_2) \\
=& F^{h_2h_1, f_1f_2}(\tau_R).
\end{aligned}
$$

In the above derivation, the first and the last equality are due to Equation 2.58, the third by induction, the fourth by the compatibility condition between multiplication and comultiplication in $D(H)^*$, and the second by the commutativity between ribbon operators on τ_1 and those on τ_2. □

Next, we examine the commutation relation between ribbon operators and local operators. Let $|GS\rangle \in \mathcal{H}$ be the ground state[5]. Then at any site s, the local operators act on $|GS\rangle$ as follows,

$$
\begin{aligned}
& A_a(s)|GS\rangle = |GS\rangle, \\
& B_f(s)|GS\rangle = f(1)|GS\rangle, \quad a \in H, f \in H^*.
\end{aligned}
$$

Let τ be a ribbon with initial site $s_0 = \partial_0\tau$ and terminal site $s_1 = \partial_1\tau$. Assume the length of τ, i.e., the number of triangles contained in τ, is greater than one. The following is a

[5]↑To the interest of the current paper, we can assume the lattice is defined on the sphere or the infinite plane, and so there is a unique ground state.

technical lemma concerning the commutation relation between ribbon operators on τ and local operators on its ends.

Lemma 2.3.1. Let τ_L and τ_R be a locally clockwise and a locally counterclockwise ribbon, respectively, as described above.

(1) At s_0, we have

$$A_a(s_0)F^{(h,f)}(\tau_L) = \sum_{(a)} F^{\{a'hS(a'''),f[S(a'')?]\}}(\tau_L)A_{a^{(4)}}(s_0), \tag{2.63a}$$

$$A_a(s_0)F^{(h,f)}(\tau_R) = \sum_{(a)} F^{\{a''hS(a^{(4)}),f[S(a''')?]\}}(\tau_R)A_{a'}(s_0), \tag{2.63b}$$

$$B_t(s_0)F^{(h,f)}(\tau_L) = \sum_{(h)} F^{(h'',f)}(\tau_L)B_{t[?S(h')]}(s_0), \tag{2.63c}$$

$$B_t(s_0)F^{(h,f)}(\tau_R) = \sum_{(h)} F^{(h'',f)}(\tau_R)B_{t[S(h')?]}(s_0). \tag{2.63d}$$

(2) At s_1, we have

$$A_a(s_1)F^{(h,f)}(\tau_L) = \sum_{(a)} F^{[h,f(?a'')]}(\tau_L)A_{a'}(s_1), \tag{2.64a}$$

$$A_a(s_1)F^{(h,f)}(\tau_R) = \sum_{(a)} F^{[h,f(?a')]}(\tau_R)A_{a''}(s_1), \tag{2.64b}$$

$$B_t(s_1)F^{(h,f)}(\tau_L) = \sum_{(i),(h),i} f(i'')F^{(h',g_i)}(\tau_L)B_{t[S(i''')h''i'?]}(s_1), \tag{2.64c}$$

$$B_t(s_1)F^{(h,f)}(\tau_R) = \sum_{(i),(h),i} f(i'')F^{(h',g_i)}(\tau_R)B_{t[?S(i''')h''i']}(s_1). \tag{2.64d}$$

In the above, $\{i\}$ is an orthogonal complete basis of H, and $g_i = \langle i, \ \rangle$ is the corresponding functional in H^*.

Proof. For a detailed proof, see Appendix A.4. The idea is that we first prove the above equations for ribbons with shortest possible length, and then extend the equality to longer ribbons using the decomposition formula in Equation 2.58. The shortest possible ribbons for the equalities in Equation 2.63 are illustrated in Figure 2.7, and those in Equation 2.64 illustrated in Figure 2.8. □

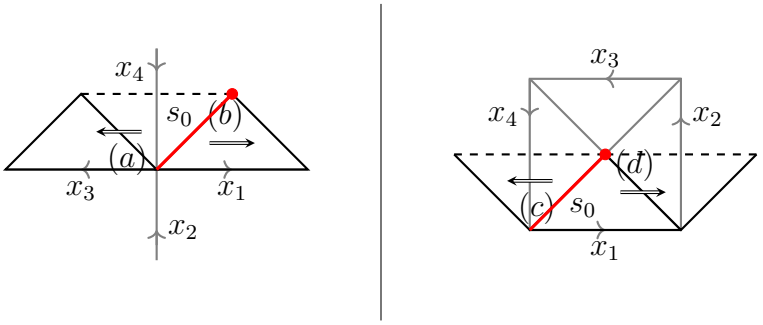

Figure 2.7. Ribbons marked with (a)-(d) correspond the Equation 2.63 a-d.

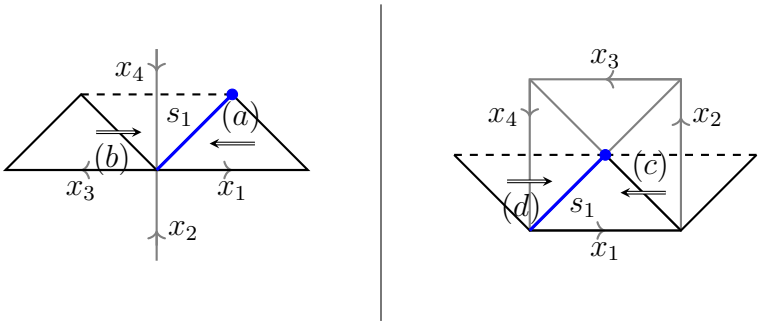

Figure 2.8. Ribbons marked with (a)-(d) correspond the Equation 2.64 a-d.

Using Lemma 2.3.1, we can also deduce that ribbon operators commute with all terms in the Hamiltonian except for those associated with the ends of the ribbon.

Proposition 2.3.2. *Let τ be a ribbon and s be a site on τ such that s has no overlap with $\partial_i\tau$. Denote the terms associated to s in the Hamiltonian by $A(s) = A_{h_0}(s), B(s) = B_\phi(s)$ where $h_0 \in H$ is the Haar integral of H and $\phi \in H^*$ is the Haar integral of H^*. Then,*

$$A(s)F^{(h,f)}(\tau) = F^{(h,f)}(\tau)A(s), \tag{2.65a}$$

$$B(s)F^{(h,f)}(\tau) = F^{(h,f)}(\tau)B(s). \tag{2.65b}$$

Proof. See Appendix A.5 for a proof. □

The commutation relation between ribbon operators and local operators at the ends in Lemma 2.3.1 may look complicated. However, if we restrict ribbon operators on the ground

state, then those relations reduce to more compact formulas. Let V_τ be the Hilbert space of ribbon operators on τ acting on the ground state,

$$V_\tau = \mathrm{span}_{\mathbb{C}}\{|h \otimes f\rangle \equiv F^{h\otimes f}(\tau)|GS\rangle \ : \ h \otimes f \in D(H)^*\}.$$

Then, V_τ is naturally identified with the space $D(H)^*$. Recall from Equations 2.38 and 2.39, $D(H)$, as a Hopf algebra, has two natural representations on $D(H)^*$ denoted by L and R, where L is induced from the left multiplication of $D(H)$ on itself and R is induced from the right multiplication (precomposed by the antipode). Apparently, these two actions commute with each other.

Proposition 2.3.3. *Let τ be a ribbon of either local orientation with $s_i = \partial_i \tau$. Identify V_τ with $D(H)^*$. Then the local operators $B_t(s_0)A_a(s_0)$ define a representation of $D(H)$ on V_τ isomorphic to L, and $B_t(s_1)A_a(s_1)$ define a representation isomorphic to R.*

Proof. The statement can be proved by restricting the identities in Equations 2.63 and 2.64 on the ground state. It is straightforward to see that, at s_0, the two identities in Equations 2.63a and 2.63b corresponding to the two cases of local orientations both reduce to,

$$A_a(s_0) \mid h \otimes f\rangle = \sum_{(a)} \mid a'hS(a'''), f\,[S(a'')?]\rangle, \tag{2.66}$$

which agrees with Equation 2.38, the action L on $D(H)^*$:

$$L(a) \mid (h \otimes f)\rangle = \mid (h \otimes f)(S(a)?)\rangle = \sum_{(a)} \mid a'hS(a''') \otimes f\,[S(a'')?]\rangle. \tag{2.67}$$

Similarly, at s_1, for either local orientation we have

$$A_a(s_1) \mid h \otimes f\rangle = \mid h, f(?a)\rangle, \tag{2.68}$$

which agrees with Equation 2.39, the action R on $D(H)^*$:

$$R(a) \mid h \otimes f\rangle = \mid (h \otimes f)(?a)\rangle = \mid h \otimes f(?a)\rangle. \tag{2.69}$$

We leave the verification for the actions of $B_f(s_0)$ and $B_f(s_1)$ as an exercise. □

To summarize, ribbon operators on a sufficiently long ribbon τ commute with all terms in the Hamiltonian except those associated with the ends of τ. Hence, ribbon operators create excitations only at the ends of a ribbon. When acting on the ground state, the space of ribbon operators on τ is naturally identified with $D(H)^*$. The action of local operators on $\partial_i\tau$ preserve $D(H)^*$. Thus, $D(H)^*$ can be thought of as the space of elementary excitations. More specifically, the action on $\partial_0\tau$ define a representation of $D(H)$ on $D(H)^*$ coinciding with L, and that on $\partial_1\tau$ a representation of $D(H)$ on $D(H)^*$ coinciding with R. These two actions commute. By standard representation theory (see Equation 2.36), we have the decomposition,

$$D(H)^* \simeq \bigoplus_{\mu\in \mathrm{Irr}_{D(H)}} \mu\otimes\mu^*, \tag{2.70}$$

where L acts on the first factor and R acts on the second factor. Therefore, the local operators on the ends of τ can map a state in a sector $\mu^*\otimes\mu$ to any other state within the same sector, but cannot permute states of different sectors. This implies that the types of elementary excitations are labelled by irreducible representations of $D(H)$. Using Fourier transformation, it is not hard to find a specific basis $\{\langle \nu ab \mid :\ \nu\in \mathrm{Irr}_{D(H)}, a, b = 1, \cdots, dim(\nu)\}$ of $D(H)^*$ so that L acts only on the a index and R acts only on the b index (See Appendix A.6). That is, for $m\in D(H)$,

$$L(m)(\langle \nu ab \mid) = \sum_k D^\nu(m)_{ka}\langle \nu kb \mid, \tag{2.71}$$

$$R(m)(\langle \nu ab \mid) = \sum_k D^{\nu^*}(m)_{kb}\langle \nu ak \mid . \tag{2.72}$$

2.4 Conclusion and outlook

In this paper, we provided a concrete definition of ribbon operators in the generalized Kitaev quantum double model, which is constructed over a semisimple Hopf algebra. We introduced the notion of local orientation on ribbons which we must distinguish in defining the operators on them. It was shown that even in the original Kitaev model based on non-Abelian groups, the issue of local orientation has to be addressed. Otherwise, certain

properties of ribbon operators that are expected to hold would fail. We derived some properties of ribbon operators in the generalized model. For instance, they create quasi-particle excitations only at the end of the ribbon, and the types of the quasi-particles correspond to irreducible representations of the Drinfeld double of the input Hopf algebra. While these properties are a folklore, their derivations are technically complicated.

There are several future directions to proceed. Firstly, since this Hopf-algebra-model can be further replaced by a weak Hopf algebra (or quantum groupoid) [62], it will be interesting to define and study ribbon operators in that case. Secondly, the generalized Kitaev model may find applications in topological quantum computing. For example, which Hopf algebras support universal quantum computing? Lastly, in [68], the authors gave a Hamiltonian formulation for gapped boundaries in the original Kitaev model. It will be interesting to generalize the formulation to the case of Hopf algebras.

3. GENERALIZED KITAEV SPIN LIQUID MODEL AND EMERGENT TWIST DEFECT

This chapter contains work from the article entitled "Generalized Kitaev spin liquid model and emergent twist defect" written by the author, Penghua Chen, and Shawn X. Cui published on Annals of Physics [2].

3.1 Introduction

Since Kitaev proposed the Kitaev Quantum Double model [10], it has garnered considerable attention due to its typical anyon behavior and the paradigm it provides for topological quantum computation. The model demonstrates how one can circumvent local errors by encoding information into anyon types and executing gates through anyon braiding, whose information is completely described by Unitary Modular Tensor Categories (UMTC). It has been proven that certain non-Abelian cases, such as the Fibonacci Anyon, can support universal quantum computation.

Following this development, numerous lattice models have been proposed with the objective of identifying different types of anyons. Two significant classes of these include the Kitaev Quantum Double model [10] and the Levin-Wen model [69]. These models actualize anyon models from varying perspectives, which are described by the Drinfeld center of a fusion category.

The realization of the actual topological phase is a complex and pivotal task. Renowned models, such as the Kitaev Quantum Double model and the Levin-Wen model, necessitate multi-body interactions, making them challenging to implement in a real-world laboratory setting. While some comparatively achievable cases, such as the toric code, are not suitable for universal computation because they only support Abelian anyons. This reality has led to an increased interest in the twist defect, as introduced by [34]. This defect exemplifies a non-Abelian Ising anyon, which stems from the lattice dislocation of the Abelian anyon case, the toric code model. Recent experimental observations of the Ising anyon statistics, as reported by [70], attest to this. It should be noted that the defect is dependent on the disruption of the lattice's local two-colorability.

Another intriguing model is the Kitaev spin liquid Model [4], which supports Abelian anyons in the gapped phase region, as well as non-Abelian anyons upon the introduction of a magnetic field to the gapless phase. This model is simple yet fruitful. However, the definition of the model relies heavily on the geometry of the honeycomb lattice, which deviates from the idea of a topological phase and is the main question to be solved in this paper. Moreover, it has also been pointed out that a spin liquid model on a honeycomb lattice with lattice dislocation will generate the twist defect as in [71]. The generalization to Z_n rotor model has been shown in [72]. This model is potentially easily realizable in a real laboratory due to the two-body nearest interaction.

Considerable theoretical progress has been made in the generalization of this model. Examples include those on a translationally invariant two-dimensional lattice with higher-coordination vertices [28][29][30], on a two-dimensional amorphous lattice [31], a three-dimensional diamond lattice [32], and works on trivalent 3D lattices [33]. It is clear that the overall phase diagram is strongly influenced by the geometric specifics of the lattice, thus also deviating our traditional understanding of "topological" phases.

In this paper, we demonstrate that the entire theory can be formulated on a generic planar lattice. The main motivation relies on the toric code limit of the original honeycomb spin liquid model as mentioned before, which is briefly reviewed in Section 3.2. We sketch the main idea here, and details are in the following sections.

The Hamiltonian of the honeycomb spin liquid system is a summation of weighted check operators, which are two-body nearest Pauli operators. The Hamiltonian is frustrated due to the non-commutation of the check operators. We say a check operator in the Hamiltonian is dominant if the coefficient of the operator is much larger than others. Kitaev selected what he refers to as "z-link" check operators to take dominance in the Hamiltonian. As a result, the vicinity of the ground state in the spectrum can be accurately described by a toric code model. The exact choice of "z-link" check operators is not important. The key is that "z-link" check operators compose a maximum set of commuting operators, which is denoted as the **stabilizer center** S_c in this paper. S_c satisfies that any check operator outside this set should anticommute with exactly two elements in S_c. We find that if one can find a

proper S_c on an arbitrary planar lattice, a toric code model always appears in the vicinity of the ground state, provided all elements in the S_c are dominant.

Moreover, we get a toric code with defects if we slightly break the requirement of S_c. Further, we propose that linearly interpolating Hamiltonians, which statically have different dominant S_cs, could be a natural way to create, move, and fuse defects in a physical system. This approach circumvents the need for introducing multi-body interaction or longer-range interactions. This proposal might inspire real material realization since we only need to establish and adjust the strength of two-body interactions, as illustrated in Section 3.4. Moreover, a circuit description is plausible since these operations are facilitated by time evolution operators, which are naturally unitary.

This paper is organized as follows:

In Section 3.2, we provide a concise review of the original honeycomb model and reintroduce necessary notations, such as the shrunken lattice.

Section 3.3 introduces our method of generalization, to describe the Hamiltonian over an arbitrary lattice. Initially, we rewrite the toric code on a lattice where qubits are positioned on vertices rather than edges, as discussed in Section 3.3.1. This rewriting is inspiring, as the recovery of the toric code typically results in a lattice with qubits placed on vertices. Subsequently, in Sections 3.3.2 and 3.3.3, we demonstrate how to define check operators on arbitrary lattices where vertices have degrees greater than 3, and given an appropriate choice of a Stabilizer Center (S_c), the toric code can be recovered if the shrunken lattice is 2-colorable. It should be noted that a local disruption in the two-colorability of the shrunken lattice leads to the emergence of a twist defect.

Section 3.4 illustrates the process of creation, movement, and fusion of defects through time evolution operators.

Next, in Section 3.5, we demonstrate that the entire model can be treated as a zero-logic-qubit subsystem code in the context of an error-correcting code.

Finally, Section 3.6 concludes the paper and discusses potential future extensions.

3.2 Kitaev Honeycomb Model

Let us briefly revisit the Kitaev Honeycomb Model and establish some notations. The lattice, depicted in Figure 3.1a and denoted by $\Gamma = (V, E, P)$, consists of vertices (V), edges (E), and plaquettes (P).

The notation $\partial_1 e$ and $\partial_2 e$ are used to refer to the two vertices at the end of edge $e \in E$, and $\partial e = \{\partial_1 e, \partial_2 e\}$ indicates the set. $N(A)$ is the count of the set A. A frequently used symbol, d_v, denotes the count of set $e \mid e \in E, v \in \partial e$, i.e., the degree of the vertex v. $Bo(p) \subseteq E$, for $p \in P$, represents the edges that border the plaquette p.

Each vertex houses a qubit. The total Hilbert Space is defined as:

$$\mathcal{H} := \bigotimes_{v \in V} \mathcal{H}_v \tag{3.1}$$

Each edge on the lattice is associated with a symbol x, y, z. For the honeycomb lattice, we label all the edges as illustrated in Figure 3.1a, consistent with the original paper [4]. These edges are referred to as "x-edges", "y-edges", and "z-edges". The edge associated with $x(y, z)$ involves a two-body Pauli operator $X \otimes X$ ($Y \otimes Y$, $Z \otimes Z$) acting on the qubits at the ends of the edge. The operators linked to edges are defined as check operators, denoted by P_e. We say that two check operators are unconnected if the edges associated with these operators are not connected. In this paper, we use X, Y, Z to represent Pauli Operators $\sigma_x, \sigma_y, \sigma_z$:

$$\sigma_x = \begin{pmatrix} 0 & 1 \\ 1 & 0 \end{pmatrix}, \quad \sigma_y = \begin{pmatrix} 0 & -i \\ i & 0 \end{pmatrix}, \quad \sigma_z = \begin{pmatrix} 1 & 0 \\ 0 & 1 \end{pmatrix}$$

The Hamiltonian is the summation of weighted check operators:

$$H = -J_x \sum_{x-edges} X \otimes X - J_y \sum_{y-edges} Y \otimes Y - J_z \sum_{Z-edges} Z \otimes Z \tag{3.2}$$

As depicted in Figure 3.1b, the phase diagram of the Honeycomb model is well-defined. In region A (B), it represents a gapped (gapless) phase. Kitaev explicitly demonstrated, using perturbation theory, that the gapped phase is the toric code phase, where one of the

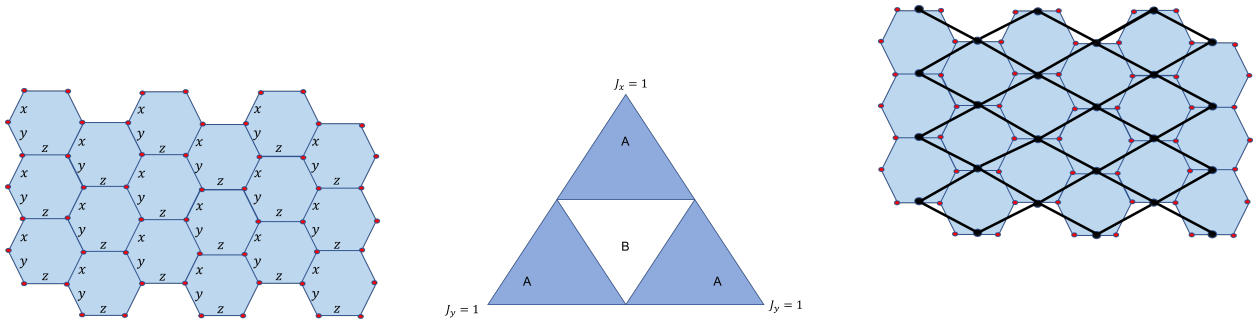

(a) (b) (c)

Figure 3.1. (a) The original Honeycomb Lattice. This lattice serves as the foundational structure for discussing the Kitaev model. (b) Phase diagram depicting the gapped phases. When one of J_x, J_y, or J_z is dominant, the system is mathematically equivalent to a toric code model. This equivalence is pivotal for understanding the model's topological properties. (c) Depiction of the shrunken lattice when J_z is dominant, illustrated by the reduction of two physical qubits to one effective qubit in the ground state of the "z-edge" check operators. This reduction highlights the effective simplification in the systems complexity under dominant conditions.

parameters J_x, J_y, J_z is much larger than the others. Then, the two qubits connected by z-edges will remain in the ground state of the check operator $Z \otimes Z$. We say these two qubits are effectively "shrunk" to a single qubit. Subsequently, the lattice is also shrunk by replacing each z-edge with a single vertex, as shown in Figure 3.1c. This process leads to what is referred to as the "shrunken" lattice.

In our notations, we denote these check operators associated with z-edges as the Stabilizer center S_c. We obtain a shrunken lattice when this S_c is dominant. The ground state under this limit is twofold: it is simultaneously the ground state of S_c and the ground state of all plaquette terms W_p, where W_p is the product of check operators associated with edges in $Bo(p)$.

Generally, on a trivalent lattice, a Hamiltonian of the following form can be considered:

$$H = -\sum_{e \in E} J_e P_e \tag{3.3}$$

The definition of check operators can vary as long as the following commutative relation remains:

The commutation relations between check operators are defined as follows:

$$[P_e, P_{e'}] = 0 \quad \text{if} \quad \partial e \cap \partial e' = \emptyset, \tag{3.4}$$

$$\{P_e, P_{e'}\} = 0 \quad \text{if} \quad \partial e \cap \partial e' \neq \emptyset, \tag{3.5}$$

for any $e \neq e'$. This means that check operators should anticommute if they intersect at exactly one vertex and commute under other scenarios. We require all check operators in the Stabilizer center S_c to be unconnected. Allowing S_c to be dominant, we obtain a shrunken lattice by replacing the edges of S_c with a single vertex. We will demonstrate that this configuration results in a specific surface code. Indeed, the shrunken lattice can vary with different S_c settings. For example, in this honeycomb lattice, the shrunken lattice at dominant x-edges and z-edges forms square lattices. However, in the work by Hastings and Haah [73], their shrunken lattice is a kagome lattice when the qubits are considered to be placed on vertices. The concept of a shrunken lattice at a given S_c will be frequently utilized.

3.3 Generalized Method

3.3.1 Toric Code on a lattice where qubits are placed on vertices

The toric code model is defined on an arbitrary planar lattice $\Gamma = (V, E, P)$, with one qubit placed on each edge. The Hamiltonian is:

$$H = -\sum_{v} A_v - \sum_{p} B_p \tag{3.6}$$

Here, $A_v = \bigotimes_{e|v\in\partial e} X_e$ and similarly, $B_p = \bigotimes_{e|e\in Bo(p)} Z_e$. The symbols X_e and Z_e indicate that the Pauli operator X and Z acts on the qubit placed on the edge e. For our purposes, we need to reshape the lattice into a more convenient form as shown in figure 3.2. The process is as follows. First, we attach a new vertex on each edge e, denoted by red dots. We add one edge to connect red dots on e_1 and e_2 if they satisfy:

$$e_1 \neq e_2 \tag{3.7}$$

$$N(\partial e_1 \cap \partial e_2) = 1 \tag{3.8}$$

$$\exists p \in P, e_1, e_2 \subseteq Bo(p) \tag{3.9}$$

We will add two edges to connect e_1 and e_2 if $N(\partial e_1 \cap \partial e_2) = 2$ in the above requirement. This results in a new lattice $\Gamma' = (V', E', P')$, where V' is the set of red dots and $V' = E$ as sets. E' is the set of newly added edges connecting red dots and $P' = V \cup P$ as sets.

Notably, the degree of the new vertex is automatically 4. The new plaquettes are two-colored by vertices and plaquettes of Γ. Consequently, the toric code becomes a lattice model on Γ', with one qubit placed on each vertex. In the new lattice as in figure 3.2c, the plaquette $p_g(p_r)$ with a green(red) circle has a plaquette term that is $\bigotimes X(Z)$ on each qubit on the boundary of $p_g(p_r)$, corresponding to previous $A_v(B_p)$ operators.

3.3.2 Generalized model on a lattice with all vertices having even degree

To generalize the model, one has to define check operators on arbitrary planar lattices $\Gamma = (V, E, P)$, where vertices can have any number as their degrees d_v. The original Honeycomb

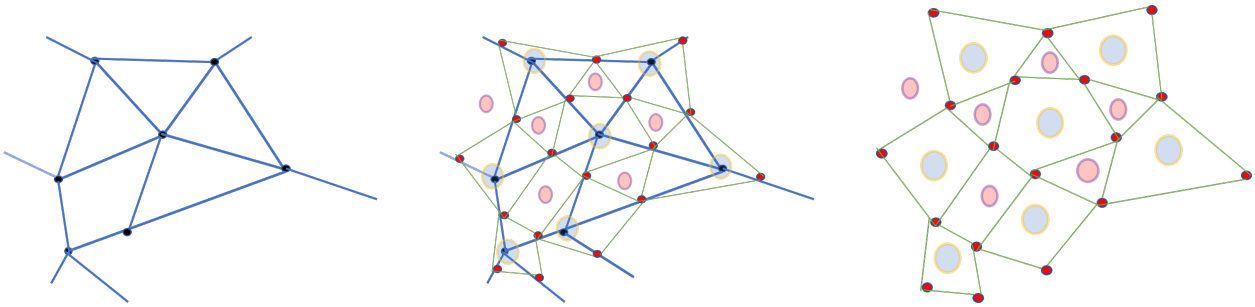

(a) (b) (c)

Figure 3.2. (a) Figure 1: Original lattice model with qubits placed on edges. Black dots represent vertices E.(b) Figure 2: Transformation process of the lattice. Red dots label the center of edges. Two red dots are connected if they belong to the same plaquette and are connected. New plaquettes are colored in red and grey circles.(c) Figure 3: The transformed lattice with qubits on vertices. The original lattice is removed. A_v and B_p operators act on the two types of plaquettes, labeled by red and grey circles respectively.

model provides a good definition for vertices that have degrees d_v less than or equal to 3; thus, we must address vertices with degrees greater than 3. We begin with a lattice, where each vertex $v \in V$ has an even degree d_v, which proves to be a simple and inspiring case. The check operator P_e should take the form of a tensor product of Pauli operators acting on the ends of edge e, namely $P_e = P_{\partial_1 e} \otimes P_{\partial_2 e}$. To maintain the property that check operators anticommute if they are connected, additional operators are required that anticommute with each other when the vertex has a higher degree. We find that placing $d_v/2 - 1$ qubits on each vertex facilitates this. For k qubits, there are $2k + 1$ mutually anti-commuting Pauli operators as follows:

$$\begin{array}{rcccccc}
P_1 & = & 1\otimes & 1\otimes & 1\otimes & \cdots & X \\
P_2 & = & 1\otimes & 1\otimes & 1\otimes & \cdots & Y \\
 & \vdots & \vdots & \ddots & \vdots & & \\
P_{2t+1} & = & \underbrace{1\cdots\otimes 1}_{k-t-1}\otimes & X\otimes & Z\otimes & \cdots & Z \\
P_{2t+2} & = & \underbrace{1\cdots\otimes 1}_{k-t-1}\otimes & Y\otimes & Z\otimes & \cdots & Z \\
 & \vdots & \vdots & \ddots & \vdots & & \\
P_{2k+1} & = & Z\otimes & Z\otimes & Z\otimes & \cdots & Z
\end{array} \tag{3.10}$$

Importantly, because we ultimately aim to reach the toric code, the signs of each term do not significantly matter, as different sign configurations are related by unitary transformations. This allows us to consider each operator within the Pauli group $\mathcal{P} = \{G/\{+1, -1, +i, -i\}\}$, where G is designated to represent the set of all possible tensor products of Pauli operators.

Within the Pauli group, the phase gate P_{gate} interchanges X and Y, while leaving Z unaffected. This can swap P_{2t+1} with P_{2t+2} for any $0 \leq t < k$. Subsequently, the Hadamard gate H_{gate} flips X and Z, which in turn flips P_{2k+1} with P_{2k-1}. The gate $S_{\text{gate}} = P_{\text{gate}} \circ H_{\text{gate}} \circ P_{\text{gate}}$ flips Y and Z. CNOT gate is a unitary operator. Elementary actions by conjugating CNOT gate on two-qubits Pauli operators are given by:

$$\begin{aligned}
&\text{CNOT}(IX) = IX, \quad \text{CNOT}(XI) = XX, \\
&\text{CNOT}(IZ) = ZZ, \quad \text{CNOT}(ZI) = ZI.
\end{aligned} \tag{3.11}$$

A sequence of conjugations of operators above is then sufficient to flip P_1 with P_4, noting that it is sufficient to consider only the last two qubits. Here is how to flip $X \otimes Z$ with $1 \otimes Y$, without changing the other operators:

$$X \otimes Z \xrightarrow{H_{gate} \otimes \mathrm{Id}} Z \otimes Z \xrightarrow{\mathrm{CNOT}} 1 \otimes Z \xrightarrow{S_{gate} \otimes S_{gate}} 1 \otimes Y \xrightarrow{P_{gate} \otimes 1} 1 \otimes Y$$

$$1 \otimes Y \xrightarrow{H_{gate} \otimes \mathrm{Id}} 1 \otimes Y \xrightarrow{\mathrm{CNOT}} Z \otimes Y \xrightarrow{S_{gate} \otimes S_{gate}} Y \otimes Z \xrightarrow{P_{gate} \otimes 1} X \otimes Z$$

(a) (b)

Figure 3.3. (a) Figure 1: A local part of the entire lattice diagram. (b) Figure 2: A simplified illustration of the assignment of Pauli operator P_1 through P_4 from each vertex v to the surrounding P_e, while P_5 is assigned to the P_v. Each P_e is the tensor product of operators from the two end vertices of e. For example, the operator on the orange edge is $(1 \otimes X) \otimes (Y \otimes Z)$, or simply $P_3 \otimes P_2$.

This approach is sufficient to exchange any P_i with P_j by stacking the aforementioned operations, asserting that any distribution of these operators is equivalent. Consider a lattice where all vertices have a degree of four. The check operator on an edge, P_e, can be defined as the tensor product of Pauli operators supported on the vertices at the end of the edge e. It is important to note that the actual assignment of a Pauli operator for one P_e is not crucial, as long as P_e operators anticommute with each other when they are connected. Figure 3.3 provides an example of the assignment of Pauli operators, and any other assignment is equivalent up to a unitary transformation. An operator P_v represents a new type of check operator that is associated with only one vertex v, which, for our convenience, is chosen as $P_v = P_5$. The Hamiltonian is as follows:

$$H = -\sum_v J_v P_v - \sum_e J_e P_e \tag{3.12}$$

Now let J_v dominate. Note that these operators commute with each other, hence they share common eigenspaces. Let $J_e \ll J_v$, with $J_v = 1$, and examine the corresponding perturbation theory where $H_0 = \sum_v P_v$ and $H' = \lambda \sum_e J_e P_e$, the perturbation Hamiltonian. Here, λ is a small factor to denote the perturbation order. Denote $\mid GS\rangle$ as the ground state of H_0. As in Kitaev's paper [4], the effective Hamiltonian around the ground state is given by:

$$H_{\text{eff}} = T\left(H' + H'G_0'H' + H'G_0'H'G_0'H' + \ldots\right)T \tag{3.13}$$

where $T = \mid GS\rangle\langle GS \mid$ is the projector onto the ground state of H_0, and $G_0' = \left(\frac{1}{E_0 - H_0}\right)'$ is the Green's function, where the prime notation implies that G_0' vanishes on the ground state and acts normally on the excited states.

Appendix B.1 provides an explicit treatment of the perturbation method; here, we derive the effective Hamiltonian:

$$H_{eff} = (-1)^{\gamma_p} \sum_p \alpha_p \lambda^{l_p} W_p + constant \tag{3.14}$$

W_p is the plaquette operator, which is the product of check operators bordering the plaquette. l_p indicates the perturbation order and $(-1)^{\gamma_p}$ is used to fullfill the gap between the perturbed effective Hamiltonian with W_p. They are explained in the appendix. α_p is an interesting path-dependent factor arises from the perturbation and we leave an interesting discussion of the zero point property in the appendix B.1.

When P_v is dominant, the two qubits placed on the vertex effectively become one qubit. The corresponding shrunken lattice, illustrated in Figure 3.4a, has $d_v = 4$, and the action of plaquette terms W_p around each vertex exerts the same local action on the vertex as in the toric code case, as shown in Figure 3.3.1.

Vertices with $d_v = 2k$ can be treated similarly, where $k > 2$ and k is an integer. Generally, for a vertex with an even d_v, we place $k = d_v/2 - 1$ qubits on the vertex, and designate

$\bigotimes_k Z$, or P_{2k+1}, to be P_v and distribute the remaining d_v Pauli operators to the surrounding edges. The check operator is defined similarly to the case where $d_v = 4$. Then, the phase we are investigating is when all P_vs are dominant. We illustrate the example of a vertex with $d_v = 6$ in Diagram 3.4b. The computation is grounded on the mapping table to find the effective Hamiltonian, as in Table 3.1. Essentially, we provide a specific distribution of operators around the vertex and calculate the effective action of the plaquette terms on this vertex. We observe that the effective two qubits split into two connected vertices with $d_v = 4$. It is clear that both vertices maintain consistent and identical local properties as of the toric code. The generic mapping table for a vertex with degree $d_v \geq 4$ is shown in Appendix B.2. When we examine the ground state of dominant P_vs, each vertex with degree $d_v = 2k$ will split into $k - 1$ vertices with degree 4.

Table 3.1. Mapping Table for a vertex with $d_v = 6$

Operator	Effective operator
$X \otimes X \otimes 1$	$X \otimes 1$
$1 \otimes X \otimes X$	$1 \otimes X$
$1 \otimes 1 \otimes Z$	$1 \otimes Z$
$1 \otimes Z \otimes 1$	$Z \otimes Z$
$Z \otimes 1 \otimes 1$	$Z \otimes 1$

After splitting all vertices with $d_v = 2k$, we obtain the shrunken lattice. We conclude that a $\mathbf{Z_2}$ phase is recovered in the generalized Kitaev model with even degree vertices when the shrunken lattice is two-colorable.

3.3.3 Generalized model on arbitrary planar lattice

The remaining question concerns how to address vertices with an odd degree $d_v \geq 5$. It is logical to place $(d_v - 1)/2$ qubits on each vertex and distribute d_v Clifford operators to

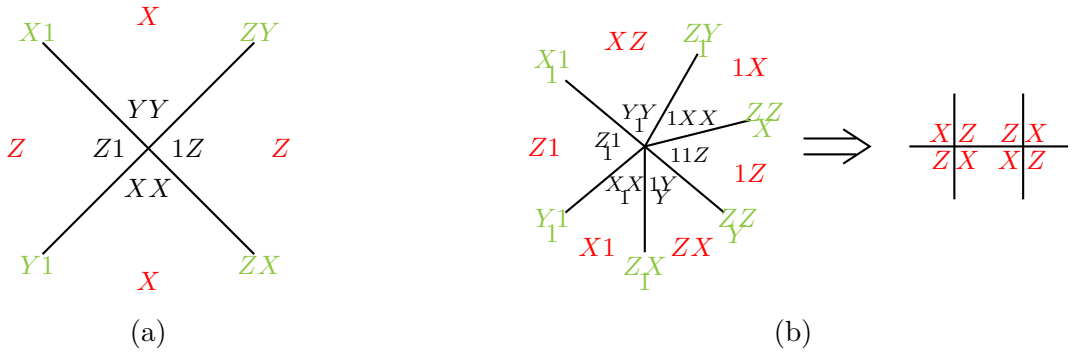

(a) (b)

Figure 3.4. (a) Figure 1: This illustration demonstrates how the effective plaquette terms are obtained on the ground state of the P_es. Each operator in the figure represents the action of either a check operator or a plaquette operator on the qubits located at the vertices. The green operator represents one of the anticommuting Clifford operators associated with edges. The black operator illustrates the plaquette term on a given vertex, and the red operator presents the effective plaquette term on the same vertex. (b) Figure 2: This depiction also shows how a vertex with degree $d_v = 6$ is transformed into two connected vertices, each with a degree of $d_v = 4$. It is essential to note that the effective action is consistent with the toric code case.

the surrounding edges so that all check operators are defined. The general Hamiltonian on a lattice $\Gamma = (V, E, P)$ is given by:

$$H = -\sum_{\{v|d_v=2k,k\in\mathbb{Z}\}} J_v P_v - \sum_{e\in E} J_e P_e, \tag{3.15}$$

$$P_e = P_{\partial_1 e} \otimes P_{\partial_2 e}. \tag{3.16}$$

We designate the stabilizer center S_c as H_0, which includes all $\{P_v \mid v \in V\}$ and a subset S_e of $\{P_e \mid e \in E\}$ such that any two $P_e \in S_e$ commute with each other and with $\{P_v \mid v \in V\}$. In other words, S_e consists of check operators on the edges that connect vertices with an odd d_v. If we further require that the shrunken lattice at S_c is a two-colorable degree-4 lattice, or equivalently, that any two vertices with an odd degree are shrunk, then the effective Hamiltonian resembles the toric code model when the coefficients of S_c are dominant.

The proof involves transforming the lattice into one where all vertices have even degrees. Notably, if we make the operators on the edge connecting two vertices with odd degrees d_1 and d_2 dominant, it is algebraically equivalent to a single vertex with degree $d_1 + d_2 - 2$ and a dominant P_v. An example is illustrated in Figure 3.5, and the general case follows similarly. However, a vertex of odd degree cannot be made equivalent to the combination of two vertices with lower degree, thus making the generalization nontrivial.

We now conclude that on a general lattice Γ, if there exists a set S_c such that all vertices are shrunk and the resulting shrunk lattice is 2-colorable, the generalized Kitaev Spin liquid model resides in the $\mathbf{Z_2}$ phase.

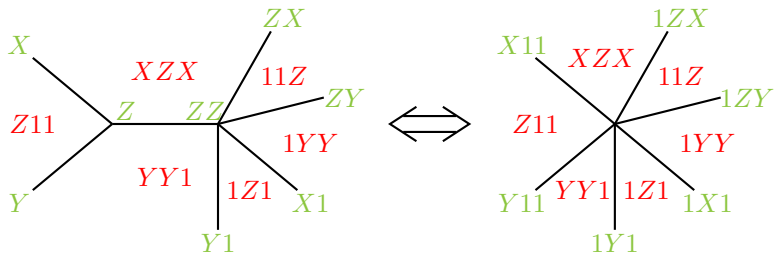

Figure 3.5. This illustration demonstrates that a vertex of degree 3 combined with a vertex of degree 5 is equivalent to a single vertex of degree 6. In the left above, a $P_e = Z \otimes Z \otimes Z$ over the red edge is put into the S_c, and in the right above, a $P_v = Z \otimes Z \otimes Z$ is put into the S_c. They have the same action of surrounding plaquette, hence these two cases are equivalent for our purpose.

3.4 Emergent Twist Defect in the gapped phase

In all previous instances, we selected S_c such that vertices with odd degrees were paired with each other, ensuring that any check operator would violate two terms in S_c. However, what happens if there is an odd-degree vertex, such as a trivalent vertex, that has not been paired with another odd-degree vertex? Revisiting the Honeycomb lattice, as depicted in Figure 3.7b, the effective Hamiltonian resembles a toric code model with two defects, similar to the findings in [34]. Notably, in our case, there is one additional plaquette as well as one more qubit within the defect line. As studied in [74], this type of lattice dislocation defect could capture unpaired Majorana modes in the original Honeycomb model.

Remarkably, keeping the nearest interaction and altering the strength of S_c is simpler than introducing more interactions between qubits. We will demonstrate in the following that a linearly interpolating Hamiltonian with different S_c choices can manipulate the defects.

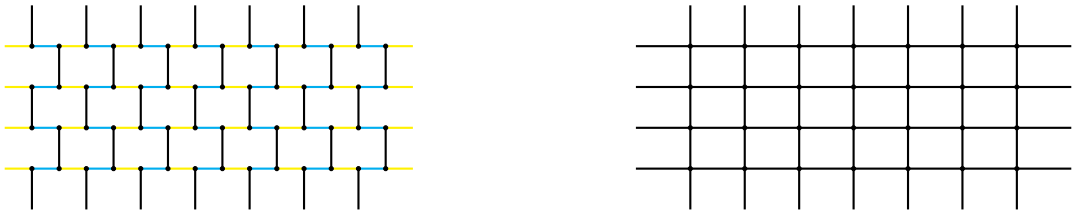

(a) (b)

Figure 3.6. (a) Shows a honeycomb lattice where all vertices have been paired and shrunk by dominating the yellow edges. (b) The resulting effective or shrunk lattice where a toric code Hamiltonian acts.

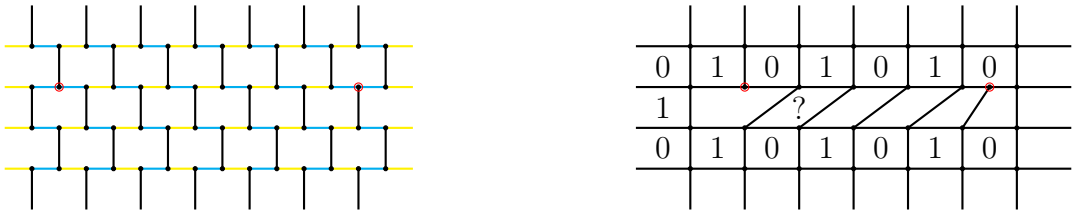

(a) (b)

Figure 3.7. (a) Displays a situation where two trivalent vertices (labelled by red circles) are not shrunk with another vertex. (b) shows the underlined phase where all check operators on yellow edges are dominant. This represents the toric code with a pair of defects.

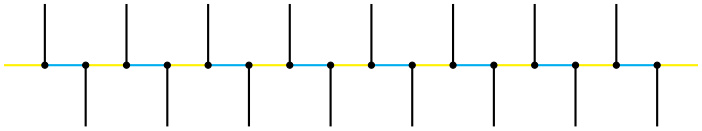

(a) toric code with no defect

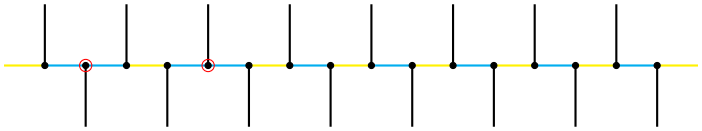

(b) toric code with a pair of defects labelled by red circles

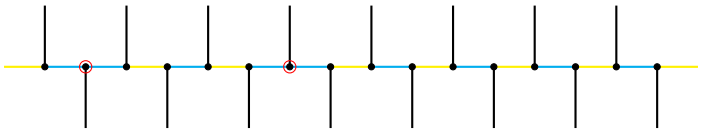

(c) Illustrates The right defect being moved one step to the right.

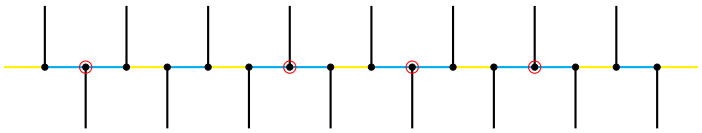

(d) Toric code with two pairs of defects

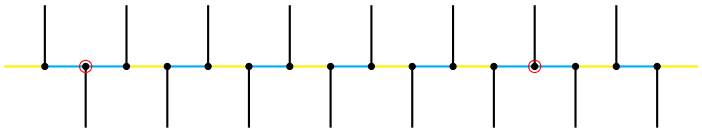

(e) Illustrates the process of fusing the two middle defects, which merges the separate pairs into a single pair.

Figure 3.8. The figures presented above depict the static Hamiltonian on a portion of the lattice. It is required that all check operators on yellow edges be dominant. Different choices of dominant check operators will lead to various cases of the effective toric code Hamiltonian, with or without defects.

The defect remains at the trivalent vertex, as a degree of three disrupts the local 2-colorability, as indicated in Figure 3.7a. Therefore, moving the defect involves relocating the trivalent vertex.

Consider Figure 3.8, which depicts a section of a larger lattice, similar to those shown in Figures 3.6 and 3.7. All check operators on yellow edges are designated as dominant. The configuration outside this localized area remains unchanged. This setup presents five potential configurations, where the effective Hamiltonian can represent the toric code, with or without defects. To transition between these static states, we introduce time evolution, facilitating the creation, movement, and fusion of defects.

Focusing on the movement of a defect as a detailed example (the other processes are analogous), we examine a more specific local structure in Figure 3.9, which illustrates the transformation from Figure 3.8b to Figure 3.8c. We use $H(0)$ and $H(T)$ to denote their respective static Hamiltonians. The linear interpolation between them is introduced as follows:

$$H(t) = H(0)\left(1 - \frac{t}{T}\right) + H(T)\frac{t}{T} \tag{3.17}$$

$H(0)$ and $H(T)$ represents the Hamiltonian with dominant coefficients of $S_c(0)$ and $S_c(T)$ and all perturbation terms were shut down to avoid subtlety. $H(t)$ commutes with all the plaquette terms so the action of all plaquette terms remains unchanged. Therefore, the action of the time evolution operator on the stabilizer centerS_c is crucial. We expect the state will transition into the spectrum of new stabilizer centers.

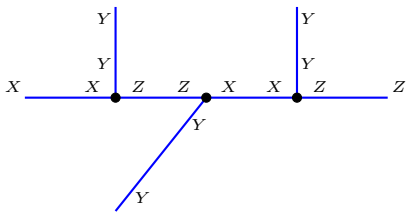

(a)

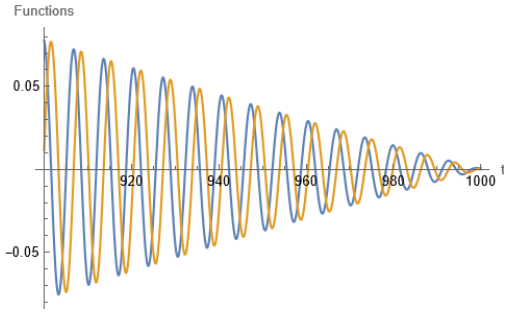

(b)

Figure 3.9. The figure on the left depicts a detailed local part of a honeycomb lattice to elucidate the movement of a defect, with the check operator explicitly labeled. On the right, the numerical results are displayed, illustrating that the real and imaginary differences between β_1 and β_2 vanish at $T = 1000$. Furthermore, this pattern persists for all $T > 1000$.

Note that most terms remain unchanged, contributing to a constant phase, as the state is always their eigenstate with an eigenvalue of $+1$. The only non-trivial terms are:

$$H = -\frac{t}{T}Z \otimes Z \otimes 1 + -(1 - \frac{t}{T})1 \otimes X \otimes X \tag{3.18}$$

The time evolution operator(TEO):

$$O(t) = \mathcal{T} \int e^{iH} dt \tag{3.19}$$

This is a formal notation; calculations need to be done by explicitly applying the Time Order operator $\mathcal{T}$. But we realize that after expanding $O(t)$, the general form is:

$$O(t) = a(t) + b(t)Z \otimes Z \otimes 1 + c(t)1 \otimes X \otimes X + d(t)Z \otimes Y \otimes X \tag{3.20}$$

Where a, b, c, and d are complex, time-dependent functions. Since the operator $O(t)$ acts on the ground state of $1 \otimes X \otimes X$, a simplified representation is allowed due to the trivial action of $1 \otimes X \otimes X$:

$$O(t) = \beta_1 + \beta_2 Z \otimes Z \otimes 1 \tag{3.21}$$

Utilizing the differential equation

$$\frac{dO(t)}{dt} = HO(t) \tag{3.22}$$

we numerically solve for $O(t)$, finding that at time T, $O(T) = \beta(1 + Z \otimes Z \otimes 1)$. Here, β is a complex number whose significance is determined by the value of T. Assuming the ground state initiates as

$$\mid GS\rangle_{t=0} = \Pi_{p \in P} \frac{W_p + 1}{2} \bigotimes_{v' \in V'} \mid 0\rangle_{v'} \tag{3.23}$$

Remember V' is the set of vertices on the shrunken lattice. Since the plaquette operators commute with the time evolution operator, the ground state transitions to:

$$\mid GS\rangle_{t=T} = \Pi_{p \in P} \frac{W_p + 1}{2} \left\{ O(T) \bigotimes_{v \in V'} \mid 0\rangle \right\} \tag{3.24}$$

This is equivalent to the ground state of $H(T)$! Thus we claim we are able to move the defect.

It is instructive to concentrate on a single chain as depicted in Figure 3.10. In this illustration, red edges correspond to the check operator $X \otimes X$, and blue edges to $Z \otimes Z$.

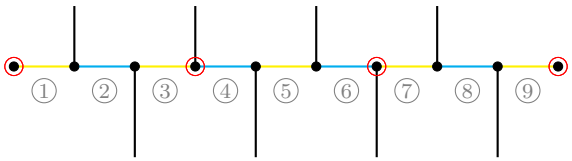

Figure 3.10. The image displays a local section of the lattice, where alternating red and blue edges represent the $X \otimes X$ and $Z \otimes Z$ checks respectively. Each edge is labeled by a unique number, with the check operator of the corresponding edge identified accordingly. The red circles indicate the positions intended for defect placement.

These operators are denoted by Op_i, where i signifies the numerical assignment to the edges. Initially, all blue checks are designated as part of the Stabilizer center.

Within this framework, we explore several critical processes. The initial process entails the creation of defects via the application of the Hamiltonian:

$$H(t) = -(Op_1 + Op_3)\left(1 - \frac{t}{T}\right) - (Op_2)\frac{t}{T} \tag{3.25}$$

Terms that commute with $H(t)$ are omitted. A numerical solution reveals that the time evolution operator is expressed as:

$$O^{creation}(T) = \beta(T)(1 + Op_2) \tag{3.26}$$

This implies that the state will be projected onto the ground state of Op_2, as anticipated, leading to the creation of a pair of defects. This transformation is represented in the transition from Figure 3.8a to Figure 3.8b.

In the second scenario, the movement of one of the defects is achieved through the following process:

$$H(t) = -(Op_2 + Op_5)\left(1 - \frac{t}{T}\right) - (Op_2 + Op_4)\frac{t}{T} \tag{3.27}$$

As explicitly demonstrated above, this time evolution is as expected to move defects.

The final process to consider is the fusion of defects. The initial case of fusion involves creating a pair of defects and subsequently fusing them back together, essentially reversing the creation process:

$$H(t) = -Op_2\left(1 - \frac{t}{T}\right) - (Op_1 + Op_3)\frac{t}{T} \tag{3.28}$$

The numerical solution for the time evolution operator is given by:

$$\begin{aligned} O(T) = {} & \beta_3(T)(1 + Op_1)(1 + Op_3) \\ & + \beta_4(T)\left[(1 - Op_1)(1 + Op_3) + (1 + Op_1)(1 - Op_3)\right] \end{aligned} \tag{3.29}$$

In this scenario, only $(1+Op_1)(1+Op_3)$ has non-zero action by examining energy levels. This indicates that upon fusing the pair created from the vacuum, we algebraically regain the vacuum state as expected. A more intriguing case of fusion involves creating two pairs of defects from the vacuum, as depicted in Figure 3.8d, and then fusing the two central defects. Denote the state before fusion as $\mid GS_4\rangle$, derived from creating four defects from $\mid GS\rangle$, as seen in Equation 3.23. The process then transitions these two pairs into a single pair:

$$H(t) = -Op_5(1-\frac{t}{T}) - (Op_4+Op_6)\frac{t}{T} \tag{3.30}$$

The TEO is similar as 3.29:

$$O(T) = \beta_5(T)(1+Op_4)(1+Op_6) + \beta_6(T)[(1-Op_4)(1+Op_6)+(1+Op_4)(1-Op_6)] \tag{3.31}$$

To check the fusion rule of the defects. We should check the normalization of the projectors. We will see $\langle GS_4 \mid (1\pm Op_4)(1\pm Op_6) \mid GS_4\rangle$ is consistently identical. To understand this, notice that:

$$\langle GS_4 \mid Op_4 \mid GS_4\rangle = \langle GS_4 \mid Op_6 \mid GS_4\rangle = 0 \tag{3.32}$$

This is because $Op_4(Op_6) \mid GS_4\rangle$ has different energy from $\mid GS_4\rangle$, as $\frac{1+Op_5}{2} \mid GS_4\rangle = \mid GS_4\rangle$ and $Op_4\frac{1+Op_5}{2} \mid GS_4\rangle = \frac{1-Op_5}{2}Op_4 \mid GS_4\rangle$. The intricate part is:

$$\langle GS_4 \mid Op_4\otimes Op_6 \mid GS_4\rangle = \left(\bigotimes_{v'\in V'}\langle 0\mid_{v'}\right)\Pi_{p\in P}\frac{W_p+1}{2}Op_4\otimes Op_6\left(\bigotimes_{v''\in V'}\mid 0\rangle_{v''}\right) \tag{3.33}$$

Remember V' here represents the set of vertices of the shrunken lattice. Notice:

$$\left(\bigotimes_{v'\in V'}\langle 0\mid_{v'}\right)\Pi_{p\in P'}W_pOp_4\otimes Op_6\left(\bigotimes_{v''\in V'}\mid 0\rangle_{v''}\right) = 0 \tag{3.34}$$

Because, for any $P'\subset P$, the product of W_ps always acts on a trivial loop of the lattice, which can not match the action of the $Op_4\otimes Op_6$ on an open cut. And $Op_4\otimes Op_6$ itself can not act trivially on $\bigotimes_{v\in V'}\mid 0\rangle_v$.

Naturally, $(1+Op_4)(1+Op_6)$ yields the vacuum, while $(1-Op_4)(1+Op_6)+(1+Op_4)(1-Op_6)$ gives rise to a free fermion. If fusion rule obeys the rule of the Ising Anyon, their coefficients should satisfy:

$$\beta_5(T) = \sqrt{2}\beta_6(T) \tag{3.35}$$

Numerical solutions suggest that $\mid \beta_5(T) \mid = \sqrt{2} \mid \beta_6(T) \mid$, with a surprisingly introduced phase. However, we can account for this by moving the phase into the definition of the state or choose the T carefully to let the phase vanish. As highlighted in [4], the free fermion excitation exhibits the same algebra as the composite quasi-particle of electric and magnetic charge ϵ of the toric code, even though they differ in energy. Kitaev proposed that the free fermion would decay to ϵ when exposed to a certain thermal bath. Consequently, we can deduce that the defects explicitly comply with the nontrivial fusion rule of the Ising Anyon as demonstrated in [34]:

$$\sigma \times \sigma = 1 + \epsilon \tag{3.36}$$

σ represents the twist defect. ϵ represents the fermion. The last thing we have to care is that although the action of plaquette terms are fixed during time evolution, the effective Hamiltonian may flip its sign so it may have excitations which violates plaquette terms.

To see this, rewrite the overall Hamiltonian in a simplified manner:

$$H = -S_c - c_p W_p \tag{3.37}$$

c_p absorbs all coefficients of the plaquette operators and S_c are dominant. From explicit numerical evaluation in appendix(B.1.1), the sign of two plaquette operator flips after creating or fusing a pair of defects. So two extra excitations appear or annihilate but moving defects won't create any excitation as shown in diagram3.11. The yellow plaquette is the one that is excited while white plaquette stays at the ground state of the corresponding W_p. The overall picture is: create two pairs of defects and four plaquettes carry plaquette excitations. Then the central two defects fused with two plaquette excitation annihilates, leaving a superposition of vacuum and free fermion excitation, which agrees with the picture that the defects capture the Majorana fermion and behaves like Ising anyon.

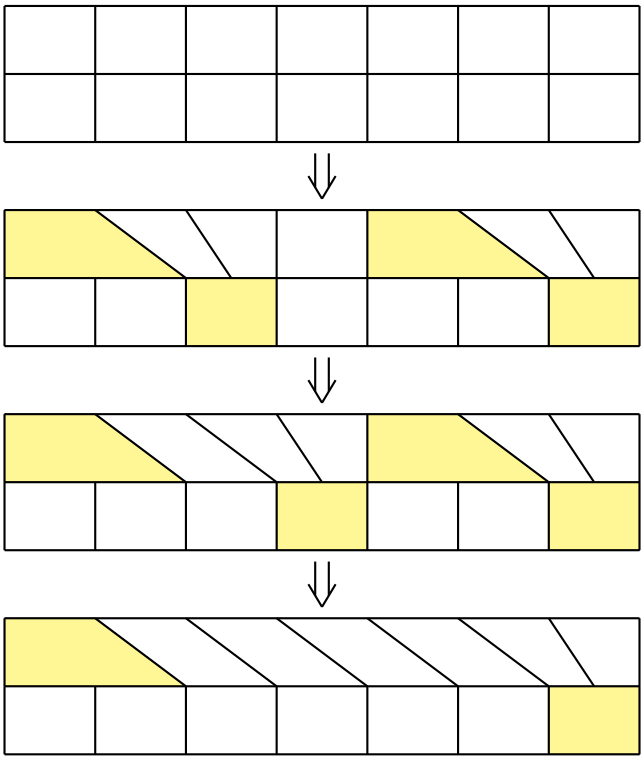

Figure 3.11. Demonstration of the excited plaquettes. Yellow plaquettes are the excited ones while white plaquettes stays at the ground state of the corresponding plaquette operators. The first figure is a part of regular surface code case and the state stays at the ground state. When two pairs of defects are created, two pairs of plaquettes, which have the trivalent vertex, will be excited. Moving defects will move the excited plaquettes accordingly with no more excitation created. After fusing the central two defects, the corresponding excitation annihilates, leaving two remaining defects at ends.

3.5 Subsystem Code aspects

In recent work by [75], the Kitaev spin liquid code on trivalent and 3-colorable lattices has been proved to be a zero-logical-qubit subsystem code. Here, we generalize this to our case. We describe the lattice using n_v for the number of vertices, n_e for the number of edges, and n_p for the number of plaquettes. We focus on orientable lattices, which could be easily extended to non-orientable cases. Initially, we prove this is true when all the vertices of the lattice have odd degrees. The gauge group is generated by $P_e \mid e \in E$. The number of gauge group generators is $n_e - 1$ due to the $\Pi_{e \in E} P_e = 1$. The generators of the stabilizer group S are generated by $\{W_p \mid p \in P\} \cup \{W_l\}$, where W_l denotes the set of operators formed by the

product of check operators along non-trivial loops of the lattice. The number of generators of S is given by $n_p - 1 + k$, where k is the number of non-trivial loops on the lattice. Assuming a vertex v has degree d_v and t_v qubits are placed on it, then:

$$n_v - n_e + n_p = 2 - k, \tag{3.38}$$

$$2n_e = \sum_v d_v, \tag{3.39}$$

$$n_q = \sum_v t_v, \tag{3.40}$$

where n_q is the total number of qubits. The number of logical qubits n_L of this subsystem code is given by:

$$\begin{aligned} n_L &= n_q - (n_g - n_s)/2 - n_s, && (3.41)\\ &= \frac{1}{2}(2n_q - n_g - n_s), && (3.42)\\ &= \frac{1}{2}(2n_q - n_e - n_p + 2 - k), && (3.43)\\ &= \frac{1}{2}(2n_q - n_e + n_v - n_e), && (3.44)\\ &= \frac{1}{2}\left(\sum_{v\in V}(2t_v + 1 - d_v)\right). && (3.45) \end{aligned}$$

In our setup, the number of qubits on an odd degree vertex is given by $t_v = (d_v - 1)/2$. This automatically results in $n_L = 0$. An even degree vertex could be treated as two connected odd degree vertices, as depicted in Fig. 3.5, but in a converse manner. This splitting does not change any of the aforementioned total quantities. Thus, our generalized two-dimensional Kitaev spin liquid model always forms a zero-logical-qubit subsystem. The implications of Floquet code are possible but are outside the scope of this paper.

3.6 Conclusion and outlook

In this paper, we have generalized the Kitaev spin liquid model on a general planar lattice. We proposed that if we can identify a stabilizer center S_c to satisfy certain requirement, that S_c contains maximum amount of commuting check operators, the vicinity of the ground

state of S_c will be effectively toric code model. If a single trivalent vertex remains in the shrunken lattice, a pair of twist defects would emerge, exhibiting Non-Abelian statistics as Ising Anyons. We have conclusively shown that we can manipulate and fuse the defect as long as the Hamiltonian is altered slowly. Furthermore, the processes of creation, movement, and fusion are all achieved by the time evolution operator, which are inherently unitary operators. It is equivalent to say we can use unitary operators to create, move and fuse defects, which aligns with our usual taste of manipulating anyons. Nonetheless, braiding continues to pose a challenge in this context. In conclusion, the generalized spin liquid model appears to be a versatile platform for realizing a general surface code.

Several promising directions for future research emerge from this study. For instance, the nature of a defect resulting from a left vertex of degree 5 remains to be explored. The algebra looks similar but it creates defect disrupting more plaquettes. An extension to describe three dimensional topological phases or Fractonic phases would also be an intriguing prospect, and is currently under preparation. An analytical calculation of the geometric factor α_p may be interesting since the numerical calculation yields highly regular and interesting results. Moreover, a more general and analogous generalization that could support the non-Abelian Kitaev Quantum Double model would be of significant interest and importance.

4. FLOQUET CODES FROM COUPLED SPIN CHAIN

This chapter contains work from the article entitled "Floquet Codes from Coupled Spin Chains" written by the author, Penghua Chen, and Shawn X. Cui published on arXiv [1].

4.1 Introduction

Kitaev proposed the paradigm for topological quantum computation via manipulating anyons [76]. The information is stored in the fusion space of anyons, and quantum gates are accessed by braiding, thus not affectable at the microscopic level, making them naturally fault-tolerant to local perturbations. This paradigm opens new horizons for quantum computation, while the anyon theory itself, or the topological phase of matter that supports anyons, remains a topic of great theoretical interest. Among these, exactly solvable topological lattice models, such as the Kitaev quantum double model [76], the string-net model [12], and the Kitaev spin liquid model [77][78], are excellent examples that exhibit the typical nature of topological phases of matter.

Exactly solvable topological models are typically associated with frustration-free Hamiltonians, which makes them natural quantum stabilizer codes where their ground states are considered as code subspaces. They are inherently error-correcting, though their multi-qubit syndrome operators are costly to measure. The introduction of the Floquet code [39] offers an explicit approach to mitigating the complexity of measuring multi-qubit syndrome operators by periodically measuring two-qubit operators, which has been shown to have good error correction properties [79][80][81].

One interesting aspect of the Floquet code is its instantaneous phase. At each round of measuring checks, the Floquet state is stabilized by a round-varying stabilizer, the Instantaneous Stabilizer Group (ISG). The original honeycomb code exhibits an instantaneous topological $\mathbf{Z}_2$ phase on a honeycomb lattice, further generalized to any 2D trivalent and 3-colorable planar lattices [82]. In 3D, based on the idea of coupling layers [83][84], 3D X-cube Floquet codes [85] and 3D toric code Floquet codes [86] have been introduced. Moreover, the latter introduced the rewinding technique to ensure that all instantaneous phases of the Floquet code are topological. On the other hand, the original honeycomb code [39] exhibits a

self-automorphism of instantaneous topological phases. This idea has been further explored through the concept of dynamical automorphism codes [40], where Floquet codes are constructed from adiabatic paths of gapped Hamiltonians. A 3D Floquet color code has been demonstrated based on this idea [87]. These aforementioned codes are always associated with a parent subsystem code, or equivalently can be described by a Kitaev spin liquid model with varying parameters. However, Floquet codes without parent subsystem codes are also possible, as shown in [88][89].

Inspired by the coupling layers construction, we recognized that it inherently possesses the characteristics of coupled spin chains. We present an explicit construction of Floquet codes using coupling spin chains, applicable to a large family of general lattices in any dimension greater than 2, as announced in Section 4.3. It is shown that the previous requirement of trivalent and 3-colorable lattices can be unified into a vertex-2-colorable physical lattice. We provide two different constructions based on the placement of coupling spin chains, which exhibit instantaneous $(n, 1)$ toric code topological phases [90] and n-dimensional X-cube fractonic phases, respectively, while the latter agrees with the construction by coupling layers in 3D [85] on a 3D cubic lattice. Our construction also demonstrates that topological phases can be realized through coupling spin chains, which broadens the applicability of coupling spin chains [91][92][93]. It naturally leads to the n-dimensional X-cube model, where we show that, on a hypercubic lattice of size L, the leading order of ground state degeneracy for the generalized model is given by $2^{n(n-1)\cdot L^{n-2}}$. The excitations are also composed of lineons and hyper-planons. We show that lineons must form $(n-2)$-dimensional multipoles to unlock extended mobility.

In the 3D construction, unlike in the 2D case, the syndrome operators can no longer survive throughout the measurement routine. They appear at certain rounds, persist for several rounds, and are then removed from the ISG. We need to be cautious about this process regarding error correction: errors are detected by observing changes of the measurement outcomes of the syndrome operators, so the measurement outcomes must be obtained at least twice before being removed from the ISG. If this is achieved, it can correct errors occurring during the rounds when the syndrome operators persist, at low error rate. However, errors outside these rounds need to be detected via other sets of syndromes. Therefore, the

synchronization of syndrome operators in the ISG is crucial to ensure error detection for all rounds of the Floquet codes. In our spin chain construction, however, we select a Steady Stabilizer Group (SSG) that persists throughout the Floquet routine and enables a unified decoder. We will show that the ISG forming topological phases is not sufficient for error correction in Floquet codes, but SSG forming classical error-correcting codes is. We present a simple 2-step Floquet Bacon-Shor code [94] that fits completely within this framework.

The paper is organized as follows.

In Section 4.2, we first present a clean formulation of the Floquet code in 2D, demonstrating how the 3-colorability of the interactions naturally arises on any 2D lattice. In Section 4.2.3, we give a detailed explanation of when and how we can get the effective measurement value of syndrome operators so that we can continue the error correction in section 4.2.4.

We then extend this construction to three dimensions in Section 4.3, where we place one spin chain on each plaquette and show how this generates the 3D Floquet toric code on a cubic lattice. Next, we focus on error correction in Section 4.3.2, which differs from previous works to accommodate general lattices. The error correction relies on a subgroup of the Instantaneous Stabilizer Group (ISG), called the Steady Stabilizer Group (SSG), which persists throughout the measurement routine. In Section 4.3.3, we explain that the Floquet code remains error-correctable when the SSG forms a classical error-correcting code at each round. The Floquet Bacon-Shor code is presented as an example that fits this paradigm. This method can be easily generalized to higher-dimensional lattices.

In Section 4.3.5, we place closed spin chains around vertices, rather than on plaquettes, to construct the X-cube Floquet code, which can be generalized to higher-dimensional, locally hypercubic-like lattices. The properties of the generalized X-cube model are also discussed.

Finally, in Section 4.4, we conclude the paper and provide a discussion on error correction, automorphisms of Floquet codes, and future directions for research.

Appendix A explicitly shows the instantaneous phases of the Floquet code, which are of particular interest. Appendix B briefly review the Laurent polynomial method and presents a special 3D Kitaev Spin Liquid model on a trivalent lattice that contains a topological phase

similar to the 3D toric code. Appendix C analyzes the properties of the generalized X-cube code on higher-dimensional hypercubic lattices with periodic boundary conditions.

4.2 2D Floquet Code from Spin Chain Construction

4.2.1 Spin Chain

A spin chain is a one-dimensional chain of spins, or qubits, of length $2n$, where nearest-neighbor interactions alternate between $X \otimes X$ and $Y \otimes Y$ terms:

$$H = -\sum_{k=0}^{n-1} \left(X_{2k} \otimes X_{2k+1} + Y_{2k+1} \otimes Y_{2k+2} \right), \tag{4.1}$$

where X, Y, and Z represent the Pauli matrices, also denoted as σ_x, σ_y, and σ_z:

$$X = \sigma_x = \begin{pmatrix} 0 & 1 \\ 1 & 0 \end{pmatrix}, \quad Y = \sigma_y = \begin{pmatrix} 0 & -i \\ i & 0 \end{pmatrix}, \quad Z = \sigma_z = \begin{pmatrix} 1 & 0 \\ 0 & -1 \end{pmatrix} \tag{4.2}$$

These matrices satisfy the following relation:

$$\sigma_i \cdot \sigma_j = \delta_{ij} + i\epsilon_{ijk}\sigma_k, \tag{4.3}$$

where δ_{ij} is the Kronecker delta and ϵ_{ijk} is the Levi-Civita symbol.

The $Z \otimes Z$ operator is introduced to couple between spin chains, as shown in Figure 4.1. Qubits are placed on the black dots. These two-body interactions are called check operators. Specifically, $X \otimes X$ and $Y \otimes Y$ are nearest-neighbor interactions within the same spin chain, referred to as inner-chain check operators, depicted by green and blue edges. On the other hand, $Z \otimes Z$ couples the spin chains and is represented by red edges, named inter-chain operators. Note that all the edges shown in the figure represent interactions, rather than "real" lattice edges. We will refer to these as checks, and the figure composed of these checks will be called the interaction diagram throughout this paper.

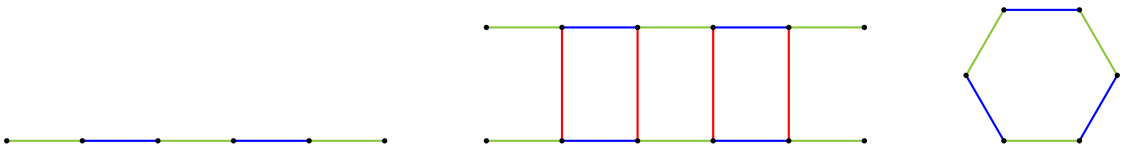

Figure 4.1. A demonstration of three different interaction diagrams of spin chains. The left diagram represents an open chain that contains nearest-neighbor $X \otimes X$ and $Y \otimes Y$ interactions, marked by green and blue edges, respectively. The middle diagram shows two spin chains coupled by $Z \otimes Z$ inter-chain check operators, marked by red edges. The right diagram represents a closed hexagonal spin chain.

4.2.2 2D Floquet Code

We begin by restating the 2D Floquet code for further generalization. Throughout this paper, we will only consider lattices with periodic boundary conditions unless specifically mentioned otherwise. Consider a 2D physical lattice Γ, represented by the lattice connected by black edges in Figure 4.2. Let E, V, and P represent the sets of edges, vertices, and plaquettes, respectively. For each plaquette p of the physical lattice, we place a closed spin chain that turns at the boundary edges, with one qubit located at each turning point. We slightly deform the turning points away from the edges to emphasize the independence of the qubits from different spin chains, though it is important to note that these qubits are still placed on the physical edges.

As a simple example, we take the 2D square lattice shown in Figure 4.2a, where black edges represent the physical lattice. One closed spin chain is placed on each plaquette. Since each black edge borders two plaquettes, two spin chains will coincide at the edge from different directions. In this case, we place a $Z \otimes Z$ operator, marked by red edges, to couple the two qubits that coincide at the same edge.

The edge-colored lattice represents the interaction diagram, denoted as Γ'. This lattice is automatically trivalent in 2D, as each edge borders only two plaquettes. Interestingly, when the original lattice Γ is 2-colorable at all vertices, Γ' becomes a trivalent and 3-colorable lattice, which has been shown to support a planar Floquet code in [82].

In the figure, we match the edge colors in Γ' to the vertex colors of Γ as follows: - All edges of Γ' crossing a black edge are colored red. - All edges of Γ' contained within plaquettes of Γ are colored according to the nearest vertices of Γ. The plaquettes of Γ' are then colored as: - Green if bordered only by green and red checks, - Blue if bordered only by blue and red checks, - Red if bordered only by blue and green checks.

We break the 3-color symmetry here, as this symmetry naturally breaks in higher dimensions. The interaction diagram obtained from the physical square lattice in Figure 4.2a explicitly represents the 2D Floquet code on a 4.8.8 lattice. In the original lattice Γ, the red-colored plaquettes correspond to the original plaquettes, while the green and blue plaquettes correspond to the two-colored vertices of Γ.

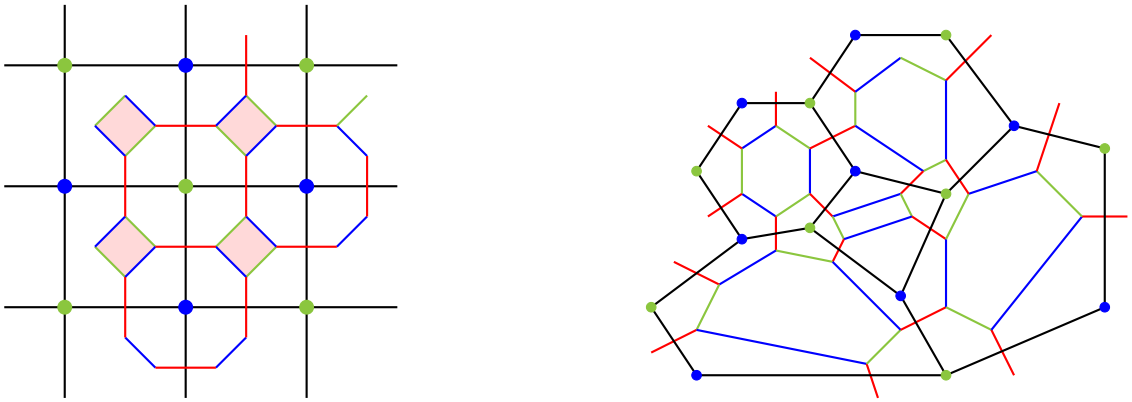

(a) (b)

Figure 4.2. The two figures above show two physical lattices connected by black edges. The vertices of the lattices are colored green and blue, with no adjacent vertices sharing the same color. In both cases, a closed spin chain is placed on each plaquette, and spin chains are coupled by red edges ($Z \otimes Z$) where they meet at a black edge. The interaction diagram is represented by the colored edges, and one qubit is placed at each vertex of the interaction diagram. Figure 4.2a depicts a square lattice, while Figure 4.2b shows a general planar lattice. It is clear that as long as the vertices connected by black edges can be 2-colored, the interaction diagram forms a trivalent, 3-colorable lattice, which has been shown to support a planar Floquet code [82].

Now we can conclude that on a 2D lattice where the vertices are 2-colorable, we can place closed spin chains over the plaquettes, which will support a 2D Floquet code. Specifically, immediately after the measurement of the red checks, or at the strong coupling limit, the instantaneous phase corresponds explicitly to the toric code on Γ, where qubits are placed on the edges of Γ.

Alternatively, we can place closed spin chains on the faces of the dual lattice $\bar{\Gamma}$ of Γ, which can also be viewed as placing them on the vertices of Γ, as shown in Figure 4.3. The 3-coloring of the new interaction diagram is determined by the 2-coloring of the vertices of $\bar{\Gamma}$, or equivalently, the 2-coloring of the faces of Γ.

It is clear that these two different placements of closed spin chains are equivalent due to the duality of the 2D toric code, and they yield equivalent 2D Floquet codes. However, as we will see, in higher dimensions, these two placements lead to different outcomes.

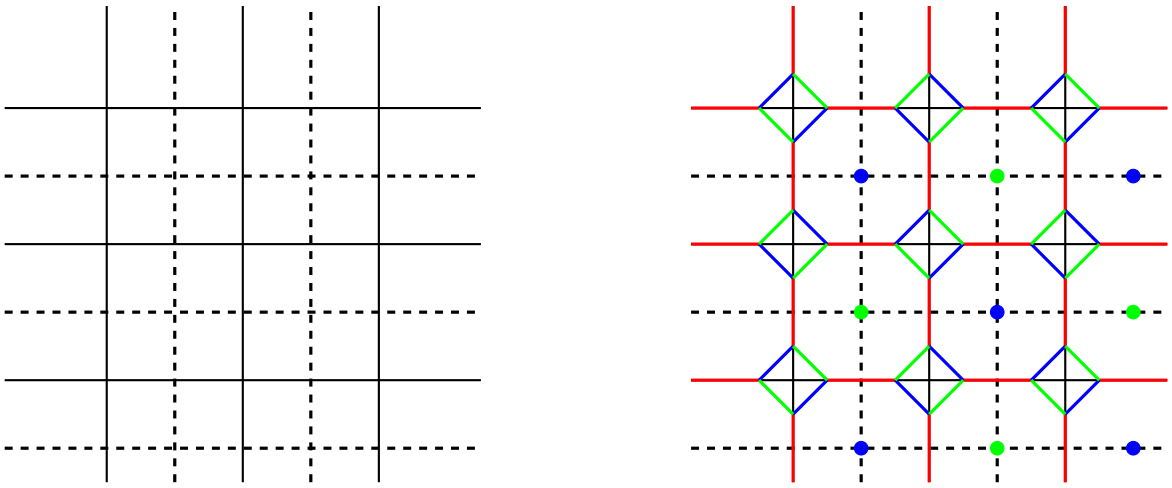

(a) (b)

Figure 4.3. Figure 4.3a shows the dual lattice Γ' of a square lattice Γ. Γ is connected by thin black edges, and Γ' by dashed edges. Γ and Γ' are dual to each other. Figure 4.3b illustrates the case where the closed spin chains are placed on the plaquettes of Γ', or equivalently around the vertices of Γ. Note that in this case, the inner-chain checks are colored based on the 2-coloring of the plaquettes of Γ.

4.2.3 Referred Syndrome Operators

The essence of the Floquet code is to avoid directly measuring the syndrome operators, although we still need the measurement results of syndromes for error detection and correction. Here, we provide a detailed explanation of how and when the measurement outcomes are inferred from the measurement results of check operators.

With the coupled spin chain construction, the Floquet routine proceeds as follows: at step $3r$, we measure the red checks; at step $3r + 1$, we measure the blue checks; and at step $3r + 2$, we measure the green checks, as shown in Table 4.1. Suppose that the green check operators are labeled as O_g, and the projectors on the eigenstate with eigenvalue $+1$ are labeled as P_g. Similarly, blue and red checks are associated with O_b, O_r, and P_b, P_r, respectively. Starting with an initial state Starting with an initial state $\mid \phi\rangle$, the state after round 2 can be written as:

$$\mid \phi_2\rangle = P_g \cdot P_b \cdot P_r \cdots \mid \phi\rangle \tag{4.4}$$

We abbreviate the notation so that each P_i in the above equation, where $i \in \{r, b, g\}$, represents the product of all projectors of the same color. Here, we assume that all measurement results are $+1$, although other outcomes can be treated equivalently.

To better understand how the measurement outcome of a red plaquette operator is inferred from the measurement outcomes of the checks, consider the example shown in Figure 4.2. Take a red plaquette that is bordered by two green checks, two blue checks, and four red checks attached to its boundary, each labeled by a number. We can then rewrite the state $\mid \phi_2\rangle$ at round 2 as:

$$\mid \phi_2\rangle = P_{g1}P_{g2} \cdot P_{b1}P_{b2} \cdot P_{r1}P_{r2}P_{r3}P_{r4} \mid \phi\rangle \tag{4.5}$$

Note that we neglect all other projectors that have no common support with this red plaquette operator in the above equation. The plaquette operators are denoted by W_i, where each W_i is the product of the check operators on the boundary of a plaquette of

color i, with $i \in \{r, b, g\}$. For this example, a red plaquette can be written explicitly as $W_r = O_{g1}O_{b1}O_{g2}O_{b2}$. When applied to the state $\mid \phi_{3r+2}\rangle$, we have:

$$\begin{aligned}
&O_{g1}O_{b1}O_{g2}O_{b2}P_{g1}P_{g2} \cdot P_{b1}P_{b2} \cdot P_{r1}P_{r2}P_{r3}P_{r4} \mid \phi\rangle \\
&= -O_{g1}O_{g2}O_{b1}O_{b2}P_{g1}P_{g2} \cdot P_{b1}P_{b2} \cdot P_{r1}P_{r2}P_{r3}P_{r4} \mid \phi\rangle \\
&= -O_{g1}O_{g2}P_{g1}P_{g2} \cdot O_{b1}O_{b2}P_{b1}P_{b2} \cdot P_{r1}P_{r2}P_{r3}P_{r4} \mid \phi\rangle \\
&= -P_{g1}P_{g2} \cdot P_{b1}P_{b2} \cdot P_{r1}P_{r2}P_{r3}P_{r4} \mid \phi\rangle
\end{aligned} \tag{4.6}$$

The equation above holds because, for any operator O, we have $O^2 = \mathrm{Id}$, and the corresponding projector onto the $+1$ eigenstate is $P = \frac{1+O}{2}$, thus $OP = P$. Additionally, $O_{b1}O_{b2}$ can pass through P_g from the second to the third line, since the product of the blue checks around a red plaquette commutes with the green checks.

The entire Floquet state is the eigenstate of W_r with eigenvalue -1, and its value is determined, or we say "inferred", from the measurements of check operators, immediately after the measurement of the green checks at step $3r + 2$, where $r \in \mathbf{Z}$. This process works similarly for other plaquette operators. The plaquette operators form the Steady Stabilizer Group (SSG), a subgroup of the Instantaneous Stabilizer Group (ISG). We simply have $\mathrm{ISG}_r = \mathrm{SSG} \cup \{r\text{-checks}\}$. Elements in SSG will have fixed values if no error occurs and can be effectively "measured" in the Floquet code, enabling error detection by reading their updated measurement outcomes.

Table 4.1. Measurement routine of the 2D Floquet code. At each step, one type of plaquette operator is referred, allowing the measurement result of the syndrome operator to be updated without directly measuring it.

Steps	**3r**	**3r+1**	**3r+2**	**3r+3**	**...**
Measure checks	Red	Blue	Green	Red	...
Updated stabilizers	Blue	Green	Red	Blue	...

4.2.4 Error Correction

Note that elements in the Steady Stabilizer Group (SSG) survive throughout the measurement routine and are updated periodically. As a result, they can be used as syndrome operators to detect the occurrence of errors. Here, we briefly outline the error correction method, which is largely similar to the approach presented in [39].

The interaction diagram has a trivalent nature, meaning any error must be surrounded by exactly three plaquettes with distinct actions on the qubit. Thus, any Pauli error will anticommute with two of the plaquette operators.

We refer to Pauli X, Y, and Z errors as green, blue, and red errors, respectively. Any single Pauli error can be detected by observing that two measurement results have flipped. For example, a green error, as shown in Figure 4.4, will flip the nearest green and red plaquette operators. Conversely, if the measurement of one red and one green plaquette operator flips, we can deduce that a green error occurred at the shared edge, the thickened edge in the figure, which must be a green edge under our assignment.

It is not possible to distinguish between green errors at either end of a green check, since $X \otimes I = (X \otimes X) \cdot (I \otimes X)$, and plaquette operators always commute with all check operators. However, this does not affect the correctability of the error. We can simply apply a green operator to either end of the green edge. For example, applying $X \otimes I$ to the first vertex will either cancel the error if it was indeed $X \otimes I$, or result in $X \otimes X$ acting on the Floquet state if the error was $I \otimes X$. This $X \otimes X$ is a check error, which will disappear automatically, as pointed out in the original paper, and can also be verified in Equation 4.2.3, since the check operator will contribute only an overall constant after it is measured.

The above argument applies similarly to any Pauli error on any vertex where surrounding plaquette operators are recorded. Thus, the entire Floquet code is error-correctable under a low error rate.

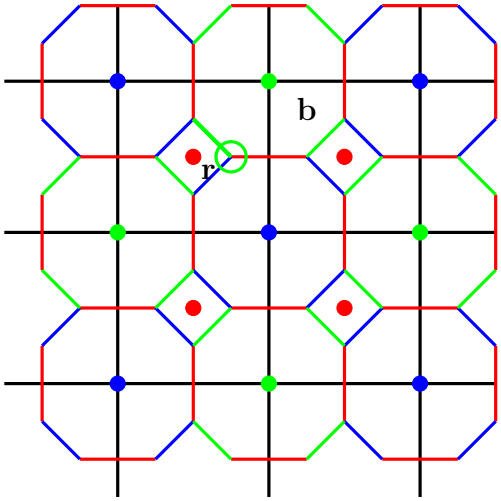

Figure 4.4. This figure shows the colored interaction diagram of the 2D Floquet code over a physical black square lattice. Each colored edge represents a check operator. Each plaquette is colored based on the color of its center dot and is associated with a plaquette operator. When a green error, marked by a green circle, occurs, the two plaquette operators on the plaquettes marked by r and b will be flipped. Conversely, when the values of these two plaquette operators are flipped, we know that a green error occurred at the thickened green edge. We can simply apply a green operator to either end of the green edge, which will either correct the error or create a green check error that will disappear automatically.

4.3 3D Error-Correctable Floquet Code

4.3.1 3D Floquet Toric Code

In two dimensions, there is only one topological phase that can be realized by a frustration-free Pauli Hamiltonian: the 2D toric code. However, in higher dimensions, there are clearly more topological phases. Therefore, we can expect different Floquet codes with distinct instantaneous topological phases arising from the coupling spin chain construction.

We take a 3D cubic physical lattice Γ as an example, as shown in Figure 4.5a, where the physical cubic lattice is represented by dashed lines. This is a direct generalization of the 2D case shown in Figure 4.2. On each plaquette of the lattice, we place a closed spin chain, and we introduce $Z \otimes Z$ interactions between spin chains where they meet at the same physical edge. As before, this leads to an interaction diagram Γ'. For convenience in coloring, we slightly deform the figure by aligning the inner-chain links to their nearest physical vertices.

We 2-color the vertices of Γ, and the edges of Γ' (the inner-chain checks) are colored based on their nearest physical vertex. The inter-chain checks are further divided into two parts. One part, colored red, consists of a set of check operators whose product covers all qubits on one edge of Γ. For example, in the 3D cubic lattice, assigning a closed spin chain to each plaquette results in four qubits surrounding one edge of Γ. To handle this, we select two non-overlapping inter-chain checks to be red, while the remaining one is marked black, as shown in Figure 4.5a. Note that in 2D, this black inter-chain check naturally disappears because the entire lattice is trivalent.

The measurement routine and ISG at each round is given by table 4.2. Green/Blue stabilizers W_g/W_b are the product of green/blue and red checks bordering the octahedron centered on the green/blue vertex. Red stabilizers are still operators formed by the product of inner-chain checks within each closed spin chain. We observe that only these three color operators commute with all checks and survive throughout the measurement routine, and thus we refer to them as the Steady Stabilizer Group (SSG). However, the Instantaneous Stabilizer Group (ISG) at round r is given by $\text{ISG}_r = \text{SSG} \cup r\text{-checks} \cup \text{NSSG}_r$, where the Non-Steady Stabilizer Group (NSSG_r) contains instantaneous stabilizers whose values are

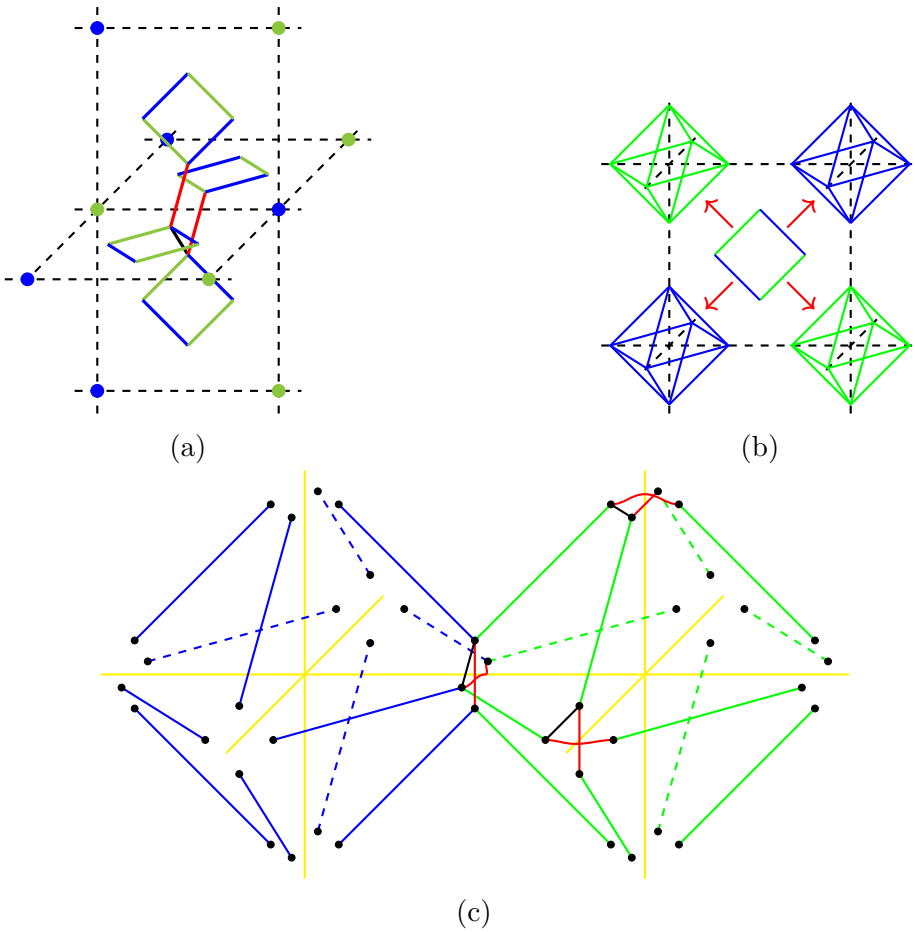

Figure 4.5. The above diagrams show the 3D Floquet toric code. Figure 4.5a depicts a physical cubic lattice Γ, represented by dashed black edges. A closed qubit chain is placed on each plaquette of Γ. Note that four qubits are located on each edge of Γ, though we separate them a little apart for clarity. We introduce three $Z \otimes Z$ check operators to couple them: two colored red and one black, with the two red checks disjoint from each other. In Figure 4.5b, the inner-chain checks are moved closer to the vertices, forming octahedra centered on the vertices of Γ. The inner-chain checks are colored according to the color of the vertex at the center of the octahedron they belong to. In the 3D Floquet code, the product of check operators (excluding the black checks) bordering each octahedron forms a stabilizer in the Steady Stabilizer Group. Figure 4.5c shows an explicit arrangement of the colored checks. In this case, the yellow edges represent the physical edges. For clarity, only three groups of red and black checks are shown, but in reality, these checks are placed on any four qubits adjacent to a physical edge.

Table 4.2. This table shows the Instantaneous Stabilizer Group (ISG) at each round of the measurement routine, containing the Steady Stabilizer Group (SSG), possible Non-Steady Stabilizer Groups (NSSG), and the check operators measured in the current round. The triangular operators in the table are depicted in Figure 4.6. The actual NSSG_{3,4,5} is not shown explicitly, as it varies depending on the choice of red checks.

Round	Check measured	ISG
6r	Red + Black	SSG + red checks + black checks
6r+1	Green	SSG + triangular-green + green checks
6r+2	Blue	SSG + triangular-green + blue checks
6r+3	Red	SSG + NSSG_3 + red checks
6r+4	Green	SSG + NSSG_4 + blue checks
6r+5	Blue	SSG + NSSG_5 + green checks

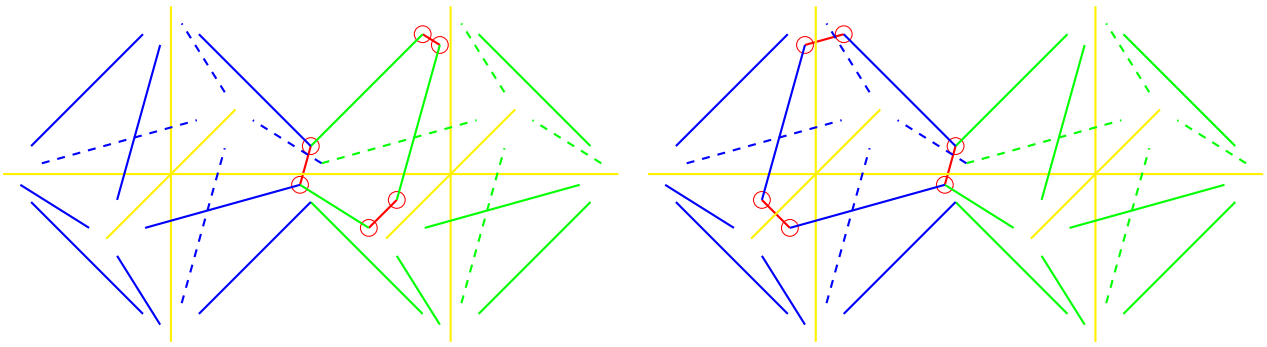

(a) (b)

Figure 4.6. This diagram shows two triangular operators. Figure 4.6a illustrates an operator that is the product of checks along a loop on the green octahedron, marked by red circles. As expected, there are eight such operators on the green octahedron. We refer to this operator as a triangular-green operator. Similarly, Figure 4.6b shows the triangular-blue operator. These triangular operators commute with all elements of the SSG, as well as the blue and green checks, but they do not commute with the red or black checks and do not always mutually commute.

randomized at certain rounds. We did not show explicit NSSG_r as they will depend on the choice of the black check.

In Appendix C.1, we show that the SSG are equivalent to the stabilizers of the 3D toric code at step $6r + 5$, using the language of the 3D Kitaev spin liquid model.

The 3D toric code Hamiltonian, defined as the negative summation of all its stabilizers, follows the definition of the (3,1) toric code in [90]. One qubit is placed on each edge:

$$H = -\sum_{v \in V} A_v - \sum_{p \in P} B_p, \tag{4.7}$$

The vertex term A_v is defined as the application of the Pauli operator X over the six edges connected to the vertex v, while B_p refers to the application of the Pauli operator Z over the four edges that form the boundary of the plaquette p. It is straightforward to see that these newly defined operators satisfy the relations $A_v^2 = B_p^2 = 1$ and commute with each other, i.e., $[A_v, B_p] = 0$.

4.3.2 Error Correction

The 3D Floquet error correction is similar to the 2D case. We still label Pauli errors by color, corresponding to the action of the check operators (e.g., $X/Y/Z$ errors are labeled green / blue / red). There are four qubits placed on an edge (since four closed spin chains intersect at that edge), and six stabilizer operators have nontrivial action on these four qubits. These six stabilizers belong to the Steady Stabilizer Group (SSG), and are periodically updated, as listed in Table 4.3, making them useful for error detection.

Now, suppose that a green error occurs. One of the red stabilizers and the green stabilizer will flip. The flipped red stabilizer shares only one common edge with the green stabilizer, and this edge is, naturally, green. It is not surprising that the green errors at either end of the green check are indistinguishable. However, similar to the 2D case, we can apply a green operator to either end of the check, and it will correct the error regardless.

The blue error behaves similarly: it flips one red stabilizer and one blue stabilizer. We can apply a blue operator to either end of the common blue edge shared by the two flipped stabilizers to correct the error.

Table 4.3. The elements of the SSG are the product of check operators. The green/blue stabilizer is the product of the blue/green, red, and black checks on the octahedron centered at the green/blue vertex of Γ. The red stabilizer is the product of inner-chain checks along each closed spin chain. This table shows the operators in the SSG, whose values are updated immediately after each round of measurement.

steps	**6 r**	**6 r+1**	**6 r +2**	**6 r +3**	**6 r +4**	**6 r +5**
Measure checks	Red and Black	Green	Blue	Red	Green	Blue
Updated SSG	Green	Blue	Red	—	—	red

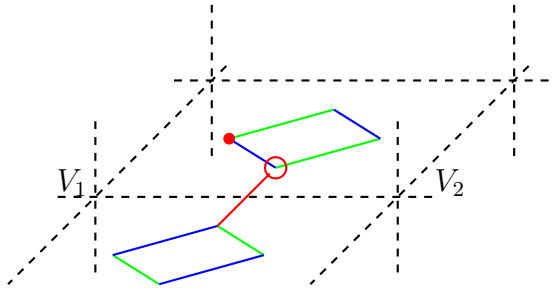

Figure 4.7. An example of a red error: it will flip the octahedron operators centered on the vertices labeled V_1 and V_2. Conversely, when these two octahedron operators are flipped, we know that a red error has occurred. As before, we can apply a red operator to either end of the red check shown, which will either cancel the error or form a red or black check that will disappear automatically.

In 2D, all three colors are symmetric because the lattice is trivalent. However, even in the simplest 3D cubic cases, while the blue, red, and green checks still form a 3D trivalent lattice, the black checks break this symmetry in 3D. When a red error occurs, only the blue and green stabilizers are flipped. The common support for these two operators consists of four qubits on the same edge. We can apply another red error to any qubit around the same edge, which will either cancel the error or become part of the group generated by the red and black check operators, disappearing at step $6r + 5$. Thus, the entire code is proven to correct any single Pauli error.

One may ask why we don't use three colors and create a 3-step routine, given that error correction works. This leads us to consider logical information, which must commute with all stabilizers and remain invariant throughout the Floquet routine. The product of check operators along loops forms the inner logical information, while the outer logical operators are effectively the string operators on non-trivial loops on the 3-torus at step $6r + 5$. While the 3-step Floquet routine can correct errors, the logical operator collapses.

In the cubic lattice case, the red checks can be chosen so that the construction can be viewed as coupling layers, where the blue, green, and red checks form separate 2D toric code layers, and the black checks couple these layers into a 3D toric code. The string logical operator of the 3D toric code is the 2D toric code's electric logical operator, which commutes with the black checks. However, if a 3-step routine is applied, the 2D electric operator becomes a magnetic logical operator, which is randomized when the black checks are measured, as it does not commute with the black checks.

To address this, we adopt the "rewinding" technique from [88], where doubling the measurement of blue, green, and red checks eventually maps the 2D electric logical operator back to itself, allowing it to survive the entire measurement routine. Details are provided in Appendix C.3.

4.3.3 Criteria for the Error Correction of Floquet Codes

It is common to require each instantaneous phase to be topological so that it can be framed within the automorphism codes framework [40]. However, we argue that this does not directly lead to an error-correctable Floquet code. First, having an instantaneous topological phase means that the elements in the ISG can detect errors as syndrome operators.

Consider a Floquet code where three types of checks, $X \otimes X$, $Y \otimes Y$, and $Z \otimes Z$, are measured at specific steps, and ISG is always topological. For simplicity, we assume that all the measurement outcomes of the checks are $+1$.

Suppose $X \otimes X$ is measured at round r. This implies that the two qubits connected by $X \otimes X$ effectively become one qubit. The $\mathrm{ISG}_r = \mathrm{SSG} \cup r\text{-checks} \cup \mathrm{NSSG}_r$. The fact that the instantaneous phase at round r is topological means that $\mathrm{SSG} \cup \mathrm{NSSG}_r$ forms a

topological phase on the effective qubits. Thus, any effective single-qubit error, such as $X_{\text{eff}} = X \otimes 1 = 1 \otimes X$, $Z_{\text{eff}} = Z \otimes Z$, and $Y_{\text{eff}} = Y \otimes Z = Z \otimes Y$, must be distinguishable by SSG$\cup$NSSG$_r$. Interestingly, X_{eff} corresponds to a single-qubit error in the Floquet code. The topological nature at round r ensures that a single-qubit X error is detectable and therefore error-correctable. Although $1 \otimes X$ and $X \otimes 1$ are indistinguishable (as they represent the same effective operator), this poses no issue for error correction since these two form a check operator, as discussed in Section 4.3.2.

Similarly, single Y and Z errors are distinguishable at rounds where $Y \otimes Y$ and $Z \otimes Z$ are measured. Thus, if all ISGs form topological phases, all single Pauli errors are detectable by elements in the ISG. However, for the Floquet code to function, these operators must be referenced at least twice during the measurement routine before they are removed from the ISG, as syndrome operators are not measured directly in Floquet codes.

A direct example can be seen at step $6r + 3$ in Table 4.2. If we treat the construction as coupling layers, with red checks within each layer and black checks coupling layers, green and blue plaquette operators within each 2D layer as in Section 4.2 will appear. The red, blue, and green plaquette operators together form the full stabilizer group for uncoupled 2D toric code layers, similar to what is described in [85]. However, only the blue plaquette operator is referenced again at round $6r + 4$, while the green plaquette operator is not referenced again before being removed from the ISG. Thus, these NSSG operators cannot be used for error correction. A similar situation occurs with the triangular-green operators, which appear in round $6r + 1$ and are removed after round $6r + 3$.

In contrast, elements in SSG are periodically referenced because they are not removed from ISG. Any change in the referred value of SSG can be used to detect errors as expected. Therefore, it is clearer for SSG to handle error correction, as discussed throughout this paper. The key observation is that it is sufficient if an effective σ_i error, which is a single-qubit σ_i error, can be distinguished by SSG when $\sigma_i \otimes \sigma_i$ is measured, where $i \in \{x, y, z\}$. In other words, in each instantaneous phase, SSG should behave as a classical error-correcting code.

We find that the Floquet version of the Bacon-Shor code [95] fits explicitly within this framework. For our purposes, we adopt a two-step measurement routine on a $L \times L$ square lattice, preserving only the inner logical operator, which corresponds to the logical operator

of the parent Bacon-Shor subsystem code. In round $2r$, red checks are measured, and in round $2r+1$, green checks are measured. Each round yields an effective L-length repetition code, which is a classical error-correcting code. An explicit example is shown in Figure 4.8 on a 3×3 lattice. Thus, a well-aligned classical code may be used to construct an error-correctable Floquet code, which we leave for future work.

4.3.4 Construction on General Lattices and Higher Dimensions

The coupling spin chain construction is purely localized, making it applicable to more general lattices. In 3D, if a lattice Γ satisfies the following requirements: 1. All vertices are 2-colorable. 2. Each edge of Γ borders an even number of plaquettes.

Then, a 3D error-correctable Floquet code can be defined. The assignment of colors is quite similar: we assign blue and green colors to the vertices, and the inner-chain checks are colored by the nearest vertex of Γ. For any edge e bordering N_q plaquettes, N_q qubits are placed on the edge. The inter-spin chain checks are again separated into red and black. Half of the non-overlapping inter-chain checks ($\frac{N_q}{2}$) will be colored red, while the remaining ones will be black. This can be achieved under the second requirement above. The Floquet routine follows the same sequence as in Table 4.3, and the decoder is the same as in the 3D cubic case, using the SSG as syndrome operators.

An interesting example is a translationally invariant lattice composed of hexagonal prisms as its unit cell. This lattice is vertex-2-colorable, but the vertical edges border three plaquettes, which do not meet the above requirement. However, this can be compensated by introducing extra vertical spin chains, as shown in Figure 4.9. New checks are assigned in the same way as usual checks, and an error-correctable Floquet code can be defined similarly. This further loosens the requirements for constructing a Floquet toric code to the following: 1. All vertices are 2-colorable. 2. Edges of Γ that border an odd number of plaquettes form several closed loops.

Interestingly, since the current checks are 3-colored (except for the black checks), this naturally opens the possibility of a CSS Floquet code, which is a dynamical code that does not have a proper parent subsystem code, as explained in [88]. The checks are associated with

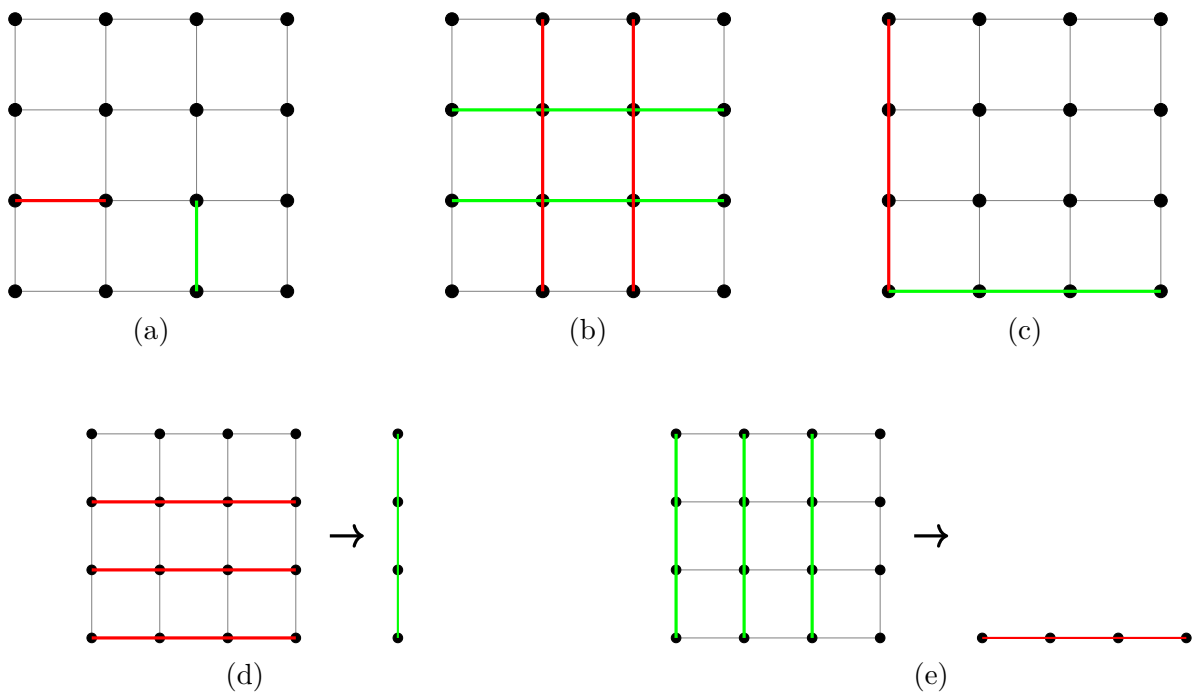

Figure 4.8. A simple illustration of the 2-step Floquet Bacon-Shor code is provided. In this example, the code is defined on a 3×3 square lattice. Figure 4.8a shows the lattice with one qubit placed on each vertex. Each horizontal edge is associated with a $Z \otimes Z$ check, shown in red, and each vertical edge is associated with an $X \otimes X$ check, shown in green. Figure 4.8b shows the elements of the Stabilizer Group. The first type is the tensor product of Z operators on qubits along any two consecutive vertical lines (red example), and the second type is the tensor product of X operators on qubits along any two consecutive horizontal lines (green example). Figure 4.8c shows the logical operators of the subsystem code. The tensor product of Z operators along the red line serves as the logical Z_L operator, and the tensor product of X operators along the green line serves as the logical X_L operator. Figure 4.8d shows that when all red checks are measured at round $2r$, the four qubits on each horizontal line effectively become a single qubit, and an effective $Z \otimes Z$ acts on adjacent effective qubits. Figure 4.8e shows the case at round $2r + 1$, where all green checks are measured, resulting in a similar effect. Essentially, both form a repetition code on different bases. It is important to note that the only logical information retained in this Floquet code is the inner logical information. Outer logical information can be found in [41] by adjusting the measurement routine.

different operators throughout the routine. In this case, the coupling spin chain construction only provides the coloring of the edges in the interaction diagram, without attaching fixed check operators. Therefore, we distinguish between "check" and "edge" here.

The measurement routine is shown in Table 4.4. At each measurement step, the two-body operator of the specified type is measured on the two qubits at the ends of the given edge color. This arrangement yields a CSS Floquet code with preserved outer logical information, as described in [88].

Table 4.4. Measurement routine for the CSS Floquet code. At each round, a two-body operator of the specified type is measured on the two qubits at the ends of the edges of the given color.

Steps	**6r**	**6r+1**	**6r+2**	**6r+3**	**6r+4**	**6r+5**
Edge Color	Blue and Red	Green	Red	Blue	Green	Red and Black
Operator Type	Green	Red	Green	Red	Green	Red

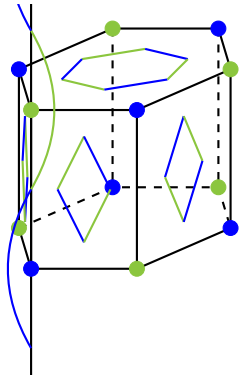

Figure 4.9. The unit cell of a translationally invariant lattice with hexagonal symmetry does not support a coupling layer construction, as it does not satisfy the requirement that each edge must border an even number of plaquettes. However, extra closed spin chains can be introduced along each vertical axis, as shown. The checks of the vertical spin chains are colored similarly, enabling the construction of a valid error-correctable Floquet code.

This generalization naturally extends to higher dimensions, using the same color arrangement for the edges, the same measurement routine shown in Table 4.3, and the same decoder introduced in Section 4.3. The result is an n-dimensional error-correctable Floquet code with an instantaneous n-dimensional $(n, 1)$ toric code phase, following the definition in

[90], where one qubit is placed on each 1-cell (the edge), and the Hamiltonian consists of the 0-cell terms (the vertex terms A_v) and the 2-cell terms (the plaquette terms B_p), similar to equation 4.3.1:

$$H = -\sum_{v \in V} A_v - \sum_{p \in P} B_p, \tag{4.8}$$

The vertex term A_v is defined as the application of the Pauli operator X over the all edges connected to the vertex v, while B_p refers to the application of the Pauli operator Z over the edges on the boundary of the plaquette p.

4.3.5 n-Dimensional Floquet X-Cube Code

In 2D, there are two ways to place closed spin chains, both leading to the same Floquet code, as discussed in Section 4.2.3. Generalizing this approach by placing spin chains on the faces of Γ results in the n-dimensional toric code Floquet code. In this section, we extend this idea based on the diagram in Figure 4.3. A 3D cubic lattice can be treated as intersecting transversal planar slices, as shown in Figure 4.10. We place closed spin chains around the vertices in the planes x-y, x-z, and y-z, respectively. When the spin chains intersect at an edge, a $Z \otimes Z$ coupling is introduced to enable interaction between them.

Interestingly, the coloring of checks must be determined within each planar slice. On each 2D slice of the lattice, the plaquettes are 2-colored, and the inner-chain checks are assigned the color of the plaquette to which they belong, similar to the 2D coloring in Figure 4.3b. Furthermore, there is no flexibility in separating red and black checks: the red checks must be the inter-chain checks within each 2D planar slice, while the remaining checks are colored black. Following this coloring scheme, we can apply the same measurement routine as outlined in Table 4.3 to realize the 3D X-cube Floquet code.

The 3D X-cube code is defined on a 3D cubic lattice, with one qubit placed on each edge of the lattice:

$$H = -\sum_{v \in V} (A_v^{x,y} + A_v^{y,z} + A_v^{x,z}) - \sum_{c \in C} B_c, \tag{4.9}$$

where V and C represent the sets of vertices and cubes, respectively. The operator $A_v^{i,j}$, with $i, j \in \{x, y, z\}$, applies the Pauli Z operator to the qubits on the four edges connected to

vertex v within the planar slice spanned by the i and j axes. The term B_c applies the Pauli X operator to the twelve edges within the cube c. These operators satisfy $(A_v^{i,j})^2 = B_c^2 = 1$ and $[A_v^{i,j}, B_c] = 0$.

The Steady Stabilizer Group (SSG) of this Floquet code consists of two types of terms. The first type is the vertex term, which is the product of inner-chain checks along each closed spin chain. The second type is the cubic term, which is the product of all checks within each unit cube, as shown in Figure 4.10b. Error correction can again be performed using the SSG alone. Note that all closed spin chains are connected by inter-chain coupling checks, ensuring they never overlap. When a red error (Pauli Z) occurs on a qubit, four cubic terms will flip. The common support of these four cubic terms consists of the four qubits connected by inter-chain $Z \otimes Z$ couplings. If a green or blue error occurs, it will flip two cubic terms and one vertex term. The common support of these three operators involves a single check of the same color as the error. Thus, the error correction process is similar to that of the Floquet toric code.

At round $6r$, the vertex terms correspond to $A_v^{i,j}$, and the cubic terms correspond to B_c, as expected. This construction recovers the X-cube Floquet code in three dimensions [85], but with a different decoding scheme.

Moreover, this construction is purely localized, avoiding the need for global coupling layers, and can be easily applied to construct the X-cube Floquet code on any manifold, consistent with previous results [96]. More interestingly, on n-dimensional lattices composed of transversely intersecting surfaces, we can place spin chains around each vertex, with each spin chain lying in a 2D plane within the local cube. The coloring of edges follows the same rules as in the 3D case. As a result, we obtain an extended X-cube model on an n-dimensional lattice Γ at round $6r$:

$$H = -\sum_{v \in V} \sum_{x_i, x_j} A_v^{x_i, x_j} - \sum_{c \in C} B_c, \tag{4.10}$$

where x_i indexes the spatial axes, and $A_v^{x_i, x_j}$ applies the Pauli Z operator to the nearest qubits on the local 2D plane spanned by x_i and x_j. Here, c denotes the n-cell of Γ, and B_c acts on the qubits within the n-cell c.

The extended model yields results similar to those of the 3D X-cube model, where the logarithm of the ground-state degeneracy scales as $\log(\text{GSD}) \approx L^{n-2}$ on an n-dimensional cubic lattice of length L. It is also a fracton model, exhibiting lineon and hyper-planon excitations. Further details can be found in Appendix C.4.

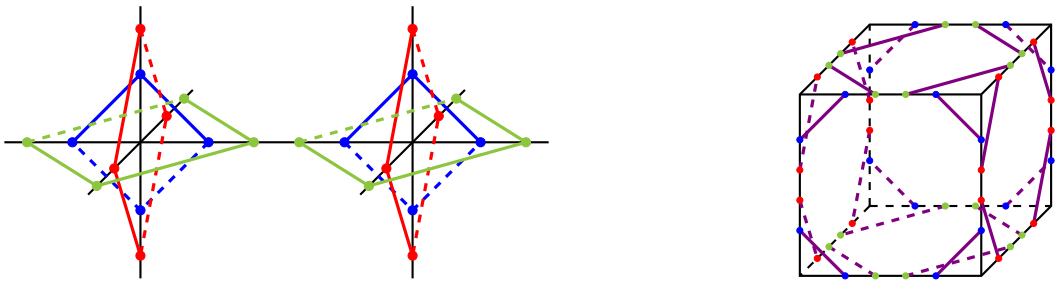

(a) (b)

Figure 4.10. Figure 4.10a illustrates the placement of spin chains on a 3D cubic lattice. Spin chains of the same color are confined to the same planar slide. Within each planar slide, the coloring of checks follows the same scheme as in Figure 4.3b. This setup generalizes the placement of spin chains on the faces of the dual lattice in 2D, placing three closed spin chains around each vertex of Γ. Each physical edge is crossed by four spin chains. Figure 4.10b shows the unit cell of this construction. All purple-colored edges represent inner-chain checks, which are colored within each planar slide. The product of all checks within the unit cell gives the cubic stabilizers.

4.4 Conclusion

In this paper, we demonstrate how the 2D Floquet code can be generally integrated into a coupling spin chain construction. We distinguish real lattice edges from the interaction diagrams composed of interaction checks. Under this construction, the previous requirement of a trivalent and 3-colorable check network is replaced by the simpler condition that the real lattice vertices are 2-colorable. By generalizing the placement of closed spin chains over the plaquettes of the lattice, we provide an explicit construction of an n-dimensional Floquet code with an instantaneous n-dimensional $\mathbf{Z}_2$ phase. Since the coupling spin chain construction is purely localized, our Floquet code can be applied to any dimensional lattice, as long as its vertices are 2-colorable.

We also describe how the Floquet state evolves and explain the emergence of an exact n-dimensional $(n, 1)$ toric code. It is important to note that the n-dimensional toric code only appears instantaneously, and the Floquet routine does not obviously induce an automorphism of topological orders. However, we demonstrate that it is sufficient to use the Steady Stabilizer Group (SSG) for error correction, with logical information preserved in the 6-step measurement routine. Therefore, a topological Floquet code is error-correctable without requiring all instantaneous phases to be topological. As outlined in Section 4.3.3, the Floquet code remains error-correctable if the SSG forms an instantaneous classical error-correcting code at all times. We explicitly present the 2-step Floquet Bacon-Shor code, which holds instantaneous repetition codes at each round.

Additionally, the 3-coloring of checks provides a natural framework for constructing a CSS Floquet code when periodic check measurements are implemented. We argue that this CSS Floquet code is error-correctable and capable of carrying logical information, serving as a counterexample to the general assumption that coupling wires or spin chains always lead to fractonic phases, as suggested in [84], [91]–[93], [97], [98].

The X-cube Floquet code [85] can be understood by placing closed spin chains around vertices within each planar slice, generalizing the placement of closed spin chains on the dual lattice plaquettes as seen in Figure 4.3b. Error correction can also be performed using the Steady Stabilizer Group (SSG) alone.

Our localized construction allows us to explicitly visualize the foliation structure. Further analysis can extend the construction to any lattice that is locally cubic-like, aligning with the general 3D X-cube model on arbitrary manifolds [96]. This approach also extends naturally to higher dimensions, where we obtain an error-correctable Floquet code with instantaneous higher-dimensional X-cube behavior. Using the Laurent polynomial method on an n-dimensional hypercubic lattice of size L with periodic boundary conditions, we show that the ground state degeneracy (GSD) satisfies:

$$\log_2(\text{GSD}) = N_q - N_S = 2 \cdot C_n^2 L^{n-2} + \text{poly}(L, n-3), \tag{4.11}$$

where poly$(L, n-3)$ is a polynomial of degree $n-3$. This model is topological, exhibiting lineon and hyper-planon excitations. Lineons, in particular, can move in extended dimensions as long as an $n-2$ dimensional multipole is paired.

In conclusion, the coupling spin chain construction localizes the traditional coupling layer approach, naturally providing a parent subsystem code. Two different families of Floquet codes can be constructed in dimensions higher than two and on more general lattices. Both are error-correctable and carry logical information. We argue that Floquet codes remain error-correctable when the SSG forms an instantaneous classical error-correcting code, as demonstrated by the Floquet Bacon-Shor code. This suggests that a well-aligned classical error-correcting code could provide a more general framework for constructing quantum Floquet codes, a topic we leave for future work.

We also identify a special type of subsystem code that behaves similarly to the 3D toric code when a maximal commuting set of gauge checks is added to the stabilizer group. This demonstrates the potential of the spin chain construction in discovering new topological phases. In the future, we aim to explore more topological phases that can be constructed using this approach and investigate how the coupling spin chain might offer new Floquet code possibilities. Additionally, CSS Floquet codes, although not typically associated with a useful parent code, might be described through anyon condensation of certain color codes. This is particularly interesting in our case, as it may lead to symmetry-broken higher-dimensional color codes.

Acknowledgement. The authors are partially supported by NSF grant CCF-2006667, Quantum Science Center sponsored by DOE's Office of Science, and ARO MURI.

REFERENCES

[1] B. Yan, P. Chen, and S. X. Cui, "Floquet codes from coupled spin chains," 2024. [Online]. Available: arXiv:2410.18265.

[2] B. Yan, P. Chen, and S. X. Cui, "Generalized kitaev spin liquid model and emergent twist defect," *Annals of Physics*, vol. 466, p. 169 682, 2024. DOI: https://doi.org/10.1016/j.aop.2024.169682.

[3] B. Yan, P. Chen, and S. X. Cui, "Ribbon operators in the generalized kitaev quantum double model based on hopf algebras," *Journal of Physics A: Mathematical and Theoretical*, vol. 55, no. 18, p. 185 201, 2022. DOI: 10.1088/1751-8121/ac552c.

[4] A. Kitaev, "Anyons in an exactly solved model and beyond," *Annals of Physics*, vol. 321, pp. 2–111, 2006. DOI: 10.1016/j.aop.2005.10.005.

[5] P. Shor, "Algorithms for quantum computation: Discrete logarithms and factoring," in *Proceedings 35th Annual Symposium on Foundations of Computer Science*, 1994, pp. 124–134. DOI: 10.1109/SFCS.1994.365700.

[6] R. P. Feynman, "Simulating physics with computers," *International Journal of Theoretical Physics*, vol. 21, pp. 467–488, 1999. DOI: https://doi.org/10.1007/BF02650179.

[7] M. A. Nielsen and I. L. Chuang, *Quantum computation and quantum information*. Cambridge; New York: Cambridge University Press, 2000. DOI: https://doi.org/10.1017/CBO9780511976667.

[8] P. W. Shor, "Fault-tolerant quantum computation," 1997. [Online]. Available: http://arxiv.org/abs/quant-ph/9605011.

[9] M. H. Freedman, A. Kitaev, and Z. Wang, "Simulation of topological field theories by quantum computers," *Communications in Mathematical Physics*, vol. 227, pp. 587–603, 2002. DOI: 10.1007/s002200200635.

[10] A. Y. Kitaev, "Fault-tolerant quantum computation by anyons," *Annals of Physics*, vol. 303, pp. 2–30, 2003. DOI: 10.1016/S0003-4916(02)00018-0.

[11] A. Y. Kitaev, "Fault-tolerant quantum computation by anyons," *Annals of Physics*, vol. 303, no. 1, pp. 2–30, 2003. DOI: https://doi.org/10.1016/S0003-4916(02)00018-0.

[12] M. A. Levin and X.-G. Wen, "String-net condensation: A physical mechanism for topological phases," *Physical Review BCondensed Matter and Materials Physics*, vol. 71, no. 4, p. 045 110, 2005. DOI: https://doi.org/10.1103/PhysRevB.71.045110.

[13] O. Buerschaper and M. Aguado, "Mapping kitaevs quantum double lattice models to levin and wens string-net models," *Physical Review B*, vol. 80, no. 15, p. 155 136, 2009. DOI: 10.1103/PhysRevB.80.155136.

[14] H. Bombin and M. A. Martin-Delgado, "A family of non-abelian kitaev models on a lattice: Topological confinement and condensation," *Physical Review B*, vol. 78, p. 115 421, 2008. DOI: 10.1103/PhysRevB.78.115421.

[15] A. Kitaev and L. Kong, "Models for gapped boundaries and domain walls," *Communications in Mathematical Physics*, vol. 313, pp. 351–373, 2012. DOI: 10.1007/s00220-012-1500-5.

[16] S. B. Bravyi and A. Y. Kitaev, "Quantum codes on a lattice with boundary," *arXiv preprint quant-ph/9811052*, 1998. [Online]. Available: https://arxiv.org/abs/quant-ph/9811052.

[17] I. Cong, M. Cheng, and Z. Wang, "Hamiltonian and algebraic theories of gapped boundaries in topological phases of matter," *Communications in Mathematical Physic s*, vol. 355, pp. 645–689, 2017. DOI: 10.1007/s00220-017-2960-4.

[18] I. Cong, M. Cheng, and Z. Wang, "Hamiltonian and algebraic theories of gapped boundaries in topological phases of matter," *Communications in Mathematical Physics*, vol. 355, pp. 645–689, 2017. DOI: 10.1007/s00220-017-2960-4.

[19] S. Beigi, P. W. Shor, and D. Whalen, "The quantum double model with boundary: Condensations and symmetries," *Communications in Mathematical Physics*, vol. 306, pp. 663–694, 2011. DOI: 10.1007/s00220-011-1294-x.

[20] A. Cowtan and S. Majid, "Algebraic aspects of boundaries in the kitaev quantum double model," 2022. [Online]. Available: http://arxiv.org/abs/2208.06317.

[21] E. Dennis, A. Kitaev, A. Landahl, and J. Preskill, "Topological quantum memory," *Journal of Mathematical Physics*, vol. 43, pp. 4452–4505, 2002. DOI: 10.1063/1.1499754.

[22] O. Buerschaper, J. M. Mombelli, M. Christandl, and M. Aguado, "A hierarchy of topological tensor network states," *Journal of Mathematical Physics*, vol. 54, no. 1, p. 012 201, 2013. DOI: 10.1063/1.4773316.

[23] Z. Wang, "Topological quantum computation," [Online]. Available: https://bookstore.ams.org/cbms-112/.

[24] V. G. Turaev, *Quantum invariants of knots and 3-manifolds* (De Gruyter studies in mathematics), 2nd rev. ed. Berlin; New York: De Gruyter, 2010. DOI: https://doi.org/10.1515/9783110435221.

[25] J. Kaidi, Z. Komargodski, K. Ohmori, S. Seifnashri, and S.-H. Shao, "Higher central charges and topological boundaries in 2+1-dimensional tqfts," *SciPost Physics*, vol. 13, p. 067, 2022. DOI: 10.21468/SciPostPhys.13.3.067.

[26] V. Ostrik, "Module categories, weak hopf algebras and modular invariants," 2001. [Online]. Available: http://arxiv.org/abs/math/0111139.

[27] *Tensor categories* (Mathematical surveys and monographs). Providence, Rhode Island: American Mathematical Society, 2015. [Online]. Available: https://bookstore.ams.org/surv-205.

[28] V. Chua, H. Yao, and G. A. Fiete, "Exact chiral spin liquid with stable spin fermi surface on the kagome lattice," *Physical Review B*, vol. 83, no. 18, p. 180 412, 2011. DOI: 10.1103/PhysRevB.83.180412.

[29] C. Wu, D. Arovas, and H.-H. Hung, "Γ -matrix generalization of the kitaev model," *Physical Review B*, vol. 79, no. 13, p. 134 427, Apr. 2009. DOI: 10.1103/PhysRevB.79.134427.

[30] H. Yao, S.-C. Zhang, and S. A. Kivelson, "Algebraic spin liquid in an exactly solvable spin model," *Physical Review Letters*, vol. 102, p. 217 202, 2009. DOI: 10.1103/PhysRevLett.102.217202.

[31] G. Cassella, P. DOrnellas, T. Hodson, W. M. H. Natori, and J. Knolle, "An exact chiral amorphous spin liquid," 2022. [Online]. Available: http://arxiv.org/abs/2208.08246.

[32] S. Ryu, "Three-dimensional topological phase on the diamond lattice," *Physical Review B*, vol. 79, p. 075 124, 2009. DOI: 10.1103/PhysRevB.79.075124.

[33] T. Eschmann, P. A. Mishchenko, K. OBrien, *et al.*, "Thermodynamic classification of three-dimensional kitaev spin liquids," *Physical Review B*, vol. 102, no. 7, p. 075 125, Aug. 2020. DOI: 10.1103/PhysRevB.102.075125.

[34] H. Bombin, "Topological order with a twist: Ising anyons from an abelian model," *Physical Review Letters*, vol. 105, p. 030 403, 2010. DOI: 10.1103/PhysRevLett.105.030403.

[35] F. Haldane, "Many-particle translational symmetries of two-dimensional electrons at rational landau-level filling," *Physical review letters*, vol. 55, no. 20, p. 2095, 1985. DOI: https://doi.org/10.1103/PhysRevLett.55.2095.

[36] C. Nayak, S. H. Simon, A. Stern, M. Freedman, and S. D. Sarma, "Non-abelian anyons and topological quantum computation," *Reviews of Modern Physics*, vol. 80, no. 3, pp. 1083–1159, 2008. DOI: 10.1103/RevModPhys.80.1083.

[37] H. Bombin, "Topological subsystem codes," *Physical Review A*, vol. 81, no. 3, p. 032 301, 2010. DOI: 10.1103/PhysRevA.81.032301.

[38] D. Poulin, "Stabilizer formalism for operator quantum error correction," *Physical Review Letters*, vol. 95, no. 23, p. 230 504, 2005. DOI: 10.1103/PhysRevLett.95.230504.

[39] M. B. Hastings and J. Haah, "Dynamically generated logical qubits," *Quantum*, vol. 5, p. 564, 2021. DOI: https://doi.org/10.22331/q-2021-10-19-564.

[40] D. Aasen, Z. Wang, and M. B. Hastings, "Adiabatic paths of hamiltonians, symmetries of topological order, and automorphism codes," *Physical Review B*, vol. 106, no. 8, p. 085 122, 2022. DOI: https://doi.org/10.1103/PhysRevB.106.085122.

[41] M. S. Alam and E. Rieffel, "Dynamical logical qubits in the bacon-shor code," 2024. [Online]. Available: arXiv:2403.03291.

[42] A. Kitaev and J. Preskill, "Topological entanglement entropy," *Physical Review Letters*, vol. 96, p. 110 404, 2006. DOI: 10.1103/PhysRevLett.96.110404.

[43] H.-C. Jiang, Z. Wang, and L. Balents, "Identifying topological order by entanglement entropy," *Nature Physics*, vol. 8, no. 12, pp. 902–905, 2012. DOI: 10.1038/nphys2465.

[44] S. Bravyi, M. Hastings, and S. Michalakis, "Topological quantum order: Stability under local perturbations," *Journal of Mathematical Physics*, vol. 51, no. 9, p. 093 512, 2010. DOI: 10.1063/1.3490195.

[45] L. Cincio and G. Vidal, "Characterizing topological order by studying the ground states of an infinite cylinder," *Physical Review Letters*, vol. 110, no. 6, p. 067 208, 2013. DOI: 10.1103/PhysRevLett.110.067208.

[46] P. Fendley, "Topological order from quantum loops and nets," *Annals of Physics*, vol. 323, no. 12, pp. 3113–3136, 2008. DOI: 10.1016/j.aop.2008.04.011.

[47] P. Wunderlich, F. Ferrari, and R. Valentí, "Detecting topological phases in the square-octagon lattice with statistical methods," 2022. [Online]. Available: http://arxiv.org/abs/2212.04519.

[48] R. Alicki, M. Fannes, and M. Horodecki, "On thermalization in kitaevs 2d model," *Journal of Physics A: Mathematical and Theoretical*, vol. 42, no. 6, p. 065 303, 2009. DOI: 10.1088/1751-8113/42/6/065303.

[49] K. Walker and Z. Wang, "(3+1)-tqfts and topological insulators," no. arXiv:1104.2632, 2011. [Online]. Available: http://arxiv.org/abs/1104.2632.

[50] A. Bauer, "Disentangling modular walker-wang models via fermionic invertible boundaries," *Physical Review B*, vol. 107, no. 8, p. 085 134, 2023. DOI: 10.1103/PhysRevB.107.085134.

[51] C. Castelnovo and C. Chamon, "Topological order in a three-dimensional toric code at finite temperature," *Physical Review B*, vol. 78, no. 15, p. 155 120, 2008. DOI: 10.1103/PhysRevB.78.155120.

[52] H. Bombin and M. A. Martin-Delgado, "Exact topological quantum order in d = 3 and beyond: Branyons and brane-net condensates," *Physical Review B*, vol. 75, no. 7, p. 075 103, 2007. DOI: 10.1103/PhysRevB.75.075103.

[53] J. Haah, "Local stabilizer codes in three dimensions without string logical operators," *Physical Review A*, vol. 83, no. 4, p. 042 330, 2011. DOI: 10.1103/PhysRevA.83.042330.

[54] J. Haah, "Lattice quantum codes and exotic topological phases of matter," 2013. [Online]. Available: http://arxiv.org/abs/1305.6973.

[55] J. Haah, "Bifurcation in entanglement renormalization group flow of a gapped spin model," *Physical Review B*, vol. 89, no. 7, p. 075 119, 2014. DOI: 10.1103/PhysRevB.89.075119.

[56] K. Ohmori and S. Shimamura, "Foliated-exotic duality in fractonic bf theories," 2023. [Online]. Available: http://arxiv.org/abs/2210.11001.

[57] M. Pretko, X. Chen, and Y. You, "Fracton phases of matter," *International Journal of Modern Physics A*, vol. 35, no. 06, p. 2 030 003, 2020. DOI: 10.1142/S0217751X20300033.

[58] W. Shirley, K. Slagle, Z. Wang, and X. Chen, "Fracton models on general three-dimensional manifolds," *Physical Review X*, vol. 8, p. 031 051, 2018. DOI: 10.1103/PhysRevX.8.031051.

[59] S. Vijay, J. Haah, and L. Fu, "Fracton topological order, generalized lattice gauge theory, and duality," *Physical Review B*, vol. 94, no. 23, p. 235 157, 2016. DOI: 10.1103/PhysRevB.94.235157.

[60] M. H. Freedman, M. Larsen, and Z. Wang, "A modular functor which is universal for quantum computation," *Communications in Mathematical Physics*, vol. 227, no. 3, pp. 605–622, 2002. DOI: https://doi.org/10.1007/s002200200645.

[61] O. Buerschaper, J. M. Mombelli, M. Christandl, and M. Aguado, "A hierarchy of topological tensor network states," *Journal of Mathematical Physics*, vol. 54, no. 1, p. 012 201, 2013. DOI: https://doi.org/10.1063/1.4773316.

[62] L. Chang, "Kitaev models based on unitary quantum groupoids," *Journal of Mathematical Physics*, vol. 55, no. 4, p. 041 703, 2014. DOI: https://doi.org/10.1063/1.4869326.

[63] O. Buerschaper and M. Aguado, "Mapping Kitaev's quantum double lattice models to Levin and Wen's string-net models," *Physical Review B*, vol. 80, no. 15, p. 155 136, 2009. DOI: https://doi.org/10.1103/PhysRevB.80.155136.

[64] O. Buerschaper, M. Christandl, L. Kong, and M. Aguado, "Electric–magnetic duality of lattice systems with topological order," *Nuclear Physics B*, vol. 876, no. 2, pp. 619–636, 2013. DOI: https://doi.org/10.1016/j.nuclphysb.2013.08.014.

[65] H. Bombin and M. Martin-Delgado, "Family of non-Abelian Kitaev models on a lattice: Topological condensation and confinement," *Physical Review B*, vol. 78, no. 11, p. 115 421, 2008. DOI: https://doi.org/10.1103/PhysRevB.78.115421.

[66] D. E. Radford, *Hopf algebras*. World Scientific, 2011, vol. 49. [Online]. Available: https://www.worldscientific.com/worldscibooks/10.1142/8100.

[67] C. Kassel, *Quantum groups*. Springer Science & Business Media, 2012, vol. 155. [Online]. Available: https://link.springer.com/book/10.1007/978-1-4612-0783-2.

[68] I. Cong, M. Cheng, and Z. Wang, "Hamiltonian and algebraic theories of gapped boundaries in topological phases of matter," *Communications in Mathematical Physics*, vol. 355, no. 2, pp. 645–689, 2017. DOI: https://doi.org/10.1007/s00220-017-2960-4.

[69] M. A. Levin and X.-G. Wen, "String-net condensation: A physical mechanism for topological phases," *Physical Review B*, vol. 71, no. 4, p. 045 110, Jan. 2005. DOI: 10.1103/PhysRevB.71.045110.

[70] T. I. Andersen, Y. D. Lensky, K. Kechedzhi, *et al.*, "Non-abelian braiding of graph vertices in a superconducting processor," *Nature*, May 11, 2023, ISSN: 1476-4687. DOI: 10.1038/s41586-023-05954-4. [Online]. Available: https://doi.org/10.1038/s41586-023-05954-4.

[71] H. Zheng, A. Dua, and L. Jiang, "Demonstrating non-abelian statistics of majorana fermions using twist defects," *Physical Review B*, vol. 92, no. 24, p. 245 139, Dec. 2015. DOI: 10.1103/PhysRevB.92.245139.

[72] Y.-Z. You and X.-G. Wen, "Projective non-abelian statistics of dislocation defects in a Z_N rotor model," *Physical Review B*, vol. 86, no. 16, p. 161 107, Oct. 2012. DOI: 10.1103/PhysRevB.86.161107.

[73] M. B. Hastings and J. Haah, "Dynamically generated logical qubits," *Quantum*, vol. 5, p. 564, 2021. DOI: 10.22331/q-2021-10-19-564.

[74] O. Petrova, P. Mellado, and O. Tchernyshyov, "Unpaired majorana modes on dislocations and string defects in kitaev's honeycomb model," *Phys. Rev. B*, vol. 90, p. 134 404, 13 Oct. 2014. DOI: 10.1103/PhysRevB.90.134404. [Online]. Available: https://link.aps.org/doi/10.1103/PhysRevB.90.134404.

[75] C. Vuillot, "Planar floquet codes," Dec. 2021. [Online]. Available: http://arxiv.org/abs/2110.05348.

[76] A. Y. Kitaev, "Fault-tolerant quantum computation by anyons," *Annals of physics*, vol. 303, no. 1, pp. 2–30, 2003. DOI: https://doi.org/10.1016/S0003-4916(02)00018-0.

[77] A. Kitaev, "Anyons in an exactly solved model and beyond," *Annals of Physics*, vol. 321, no. 1, pp. 2–111, 2006. DOI: https://doi.org/10.1016/j.aop.2005.10.005.

[78] C. G. Brell, S. T. Flammia, S. D. Bartlett, and A. C. Doherty, "Toric codes and quantum doubles from two-body hamiltonians," *New Journal of Physics*, vol. 13, no. 5, p. 053 039, 2011. DOI: 10.1088/1367-2630/13/5/053039.

[79] C. Gidney, M. Newman, and M. McEwen, "Benchmarking the planar honeycomb code," *Quantum*, vol. 6, p. 813, 2022. DOI: https://doi.org/10.22331/q-2022-09-21-813.

[80] C. Gidney, M. Newman, A. Fowler, and M. Broughton, "A fault-tolerant honeycomb memory," *Quantum*, vol. 5, p. 605, 2021. DOI: https://doi.org/10.22331/q-2021-12-20-605.

[81] A. Paetznick, C. Knapp, N. Delfosse, *et al.*, "Performance of planar floquet codes with majorana-based qubits," *PRX Quantum*, vol. 4, no. 1, p. 010 310, 2023. DOI: https://doi.org/10.1103/PRXQuantum.4.010310.

[82] C. Vuillot, "Planar floquet codes," 2021. [Online]. Available: arXiv:2110.05348.

[83] S. Vijay, "Isotropic layer construction and phase diagram for fracton topological phases," 2017. [Online]. Available: arXiv:1701.00762.

[84] H. Ma, E. Lake, X. Chen, and M. Hermele, "Fracton topological order via coupled layers," *Physical Review B*, vol. 95, no. 24, p. 245 126, 2017. DOI: https://doi.org/10.1103/PhysRevB.95.245126.

[85] Z. Zhang, D. Aasen, and S. Vijay, "X-cube floquet code: A dynamical quantum error correcting code with a subextensive number of logical qubits," *Physical Review B*, vol. 108, no. 20, p. 205 116, 2023. DOI: https://doi.org/10.1103/PhysRevB.108.205116.

[86] A. Dua, N. Tantivasadakarn, J. Sullivan, and T. D. Ellison, "Engineering 3d floquet codes by rewinding," *PRX Quantum*, vol. 5, no. 2, p. 020 305, 2024. DOI: https://doi.org/10.1103/PRXQuantum.5.020305.

[87] M. Davydova, N. Tantivasadakarn, S. Balasubramanian, and D. Aasen, "Quantum computation from dynamic automorphism codes," *Quantum*, vol. 8, p. 1448, 2024. DOI: https://doi.org/10.22331/q-2024-08-27-1448.

[88] M. Davydova, N. Tantivasadakarn, and S. Balasubramanian, "Floquet codes without parent subsystem codes," *PRX Quantum*, vol. 4, no. 2, p. 020 341, 2023. DOI: https://doi.org/10.1103/PRXQuantum.4.020341.

[89] M. S. Kesselring, J. C. Magdalena de la Fuente, F. Thomsen, J. Eisert, S. D. Bartlett, and B. J. Brown, "Anyon condensation and the color code," *PRX Quantum*, vol. 5, no. 1, p. 010 342, 2024. DOI: https://doi.org/10.1103/PRXQuantum.5.010342.

[90] M. H. Freedman and M. B. Hastings, "Double semions in arbitrary dimension," *Communications in Mathematical Physics*, vol. 347, no. 2, pp. 389–419, 2016. DOI: https://doi.org/10.1007/s00220-016-2604-0.

[91] G. B. Halász, T. H. Hsieh, and L. Balents, "Fracton topological phases from strongly coupled spin chains," *Physical review letters*, vol. 119, no. 25, p. 257 202, 2017. DOI: https://doi.org/10.1103/PhysRevLett.119.257202.

[92] D. J. Williamson and T. Devakul, "Type-ii fractons from coupled spin chains and layers," *Physical Review B*, vol. 103, no. 15, p. 155 140, 2021. DOI: https://doi.org/10.1103/PhysRevB.103.155140.

[93] T. H. Hsieh and G. B. Halász, "Fractons from partons," *Physical Review B*, vol. 96, no. 16, p. 165 105, 2017. DOI: https://doi.org/10.1103/PhysRevB.96.165105.

[94] A. Bauer, "Topological error correcting processes from fixed-point path integrals," *Quantum*, vol. 8, p. 1288, 2024. DOI: https://doi.org/10.22331/q-2024-03-20-1288.

[95] D. Bacon, "Operator quantum error-correcting subsystems for self-correcting quantum memories," *Physical Review AAtomic, Molecular, and Optical Physics*, vol. 73, no. 1, p. 012 340, 2006. DOI: https://doi.org/10.1103/PhysRevA.73.012340.

[96] W. Shirley, K. Slagle, Z. Wang, and X. Chen, "Fracton models on general three-dimensional manifolds," *Physical Review X*, vol. 8, no. 3, p. 031 051, 2018. DOI: https://doi.org/10.1103/PhysRevX.8.031051.

[97] Y. Fuji and A. Furusaki, "From coupled wires to coupled layers: Model with three-dimensional fractional excitations," *Physical Review B*, vol. 99, no. 24, p. 241 107, 2019. DOI: https://doi.org/10.1103/PhysRevB.99.241107.

[98] J. Sullivan, A. Dua, and M. Cheng, "Fractonic topological phases from coupled wires," *Physical Review Research*, vol. 3, no. 2, p. 023 123, 2021. DOI: https://doi.org/10.1103/PhysRevResearch.3.023123.

[99] J. Haah, *Lattice quantum codes and exotic topological phases of matter*. California Institute of Technology, 2013. DOI: https://doi.org/10.48550/arXiv.1305.6973.

A. SUPPLEMENTARY MATERIAL FOR CHAPTER 3

This chapter contains work from the article entitled "Ribbon operators in the generalized Kitaev quantum double model based on Hopf algebras" written by the author, Penghua Chen, and Shawn X. Cui published on Journal of Physics A [3].

A.1 Straightening equation of A_a and B_f

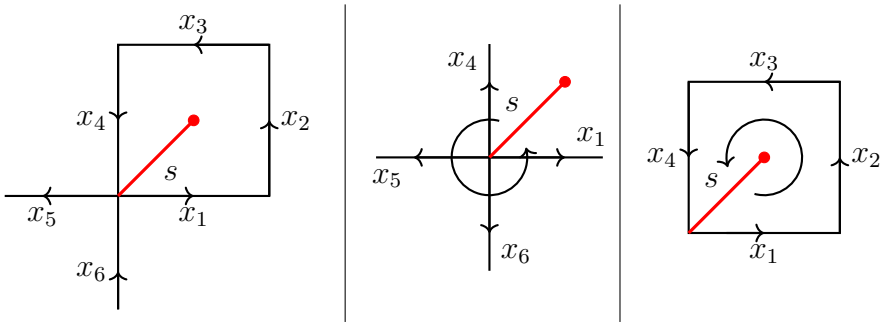

This equation holds no matter how the edges are oriented. We check the case as shown above.

$$
\begin{aligned}
&A_a(s)B_f(s) \mid x_1\ x_2\ x_3\ x_4\ x_5\ x_6\rangle \\
&= A_a(s)\sum_{(x_i)} f(x_1''x_2''x_3''x_4'') \mid x_1'\ x_2'\ x_3'\ x_4'\ x_5\ x_6\rangle \\
&= \sum_{(x_i),(a)} f(x_1''x_2''x_3''x_4'') \mid a^{(4)}x_1'\ x_2'\ x_3'\ x_4'S(a')\ a''x_5\ x_6S(a''')\rangle \\
&= \sum_{(x_i),(a)} f[S(a^{(8)})a^{(7)}x_1''x_2''x_3''x_4''S(a'')a'] \\
&\qquad\qquad \mid a^{(6)}x_1'\ x_2'\ x_3'\ x_4'S(a''')\ a^{(4)}x_5'\ x_6S(a^{(5)})\rangle \\
&= \sum_{(x_i),(a)} B_{f[S(a^{(6)})?a']}(s) \mid a^{(5)}x_1\ x_2\ x_3\ x_4S(a'')\ a'''x_5\ x_6S(a^{(4)})\rangle \\
&= \sum_{(a)} B_{f[S(a''')?a']}(s)A_{a''}(s) \mid x_1\ x_2\ x_3\ x_4\ x_5\ x_6\rangle
\end{aligned}
$$

This is exactly the straightening equation.

A.2 Violation and correction in group algebra

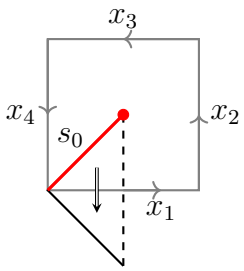

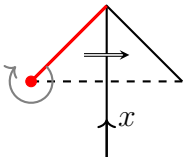

$F^{(h,g)}(\tau) \mid x\rangle = \delta_{g,e} \mid x\bar{h}\rangle$

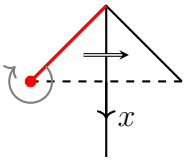

$F^{(h,g)}(\tau) \mid x\rangle = \delta_{g,e} \mid hx\rangle$

We show Equation 2.59 is violated for the ribbon τ in the first figure above for the original Kitaev model where H is taken to be the group algebra of a non-Abelian group G. In [65], only two formulas are provided for dual triangles as shown in the second and third figure above. However, we can not get the desired commutation relation using either of them:

$$
\begin{aligned}
& B_{h'}(s_0)F^{(h,g)}(\tau) \mid x_1\ x_2\ x_3\ x_4\rangle \\
&= B_{h'}(s_0)\delta_{g,e} \mid x_1\bar{h}\ x_2\ x_3\ x_4\rangle \\
&= \delta_{h',x_1\bar{h}x_2x_3x_4}\delta_{g,e} \mid x_1\bar{h}\ x_2\ x_3\ x_4\rangle \\
&\neq \delta_{g,e}\delta_{hh',x_1x_2x_3x_4} \mid x_1\bar{h}\ x_2\ x_3\ x_4\rangle \\
&= F^{(h,g)}(\tau)\delta_{hh',x_1x_2x_3x_4} \mid x_1\ x_2\ x_3\ x_4\rangle \\
&= F^{(h,g)}(\tau)B_{hh'}(s_0) \mid x_1\ x_2\ x_3\ x_4\rangle
\end{aligned}
$$

$$
\begin{aligned}
& B_{h'}(s_0)F^{(h,g)}(\tau) \mid x_1\ x_2\ x_3\ x_4\rangle \\
&= B_{h'}(s_0)\delta_{g,e} \mid hx_1\ x_2\ x_3\ x_4\rangle \\
&= \delta_{h',hx_1x_2x_3x_4}\delta_{g,e} \mid hx_1\ x_2\ x_3\ x_4\rangle \\
&\neq \delta_{g,e}\delta_{hh',x_1x_2x_3x_4} \mid hx_1\ x_2\ x_3\ x_4\rangle \\
&= F^{(h,g)}(\tau)\delta_{hh',x_1x_2x_3x_4} \mid x_1\ x_2\ x_3\ x_4\rangle \\
&= F^{(h,g)}(\tau)B_{hh'}(s_0) \mid x_1\ x_2\ x_3\ x_4\rangle
\end{aligned}
$$

Moreover, the issue can not be removed by making τ longer. Roughly, this is because for the current τ, the initial site and terminal site already lie in different plaquettes, and thus lengthening it will not affect the action of the plaquette operator at the initial site.

To resolve the issue, we recognize that τ has locally counterclockwise orientation, and hence we need to apply the following formulas for the ribbon operators,

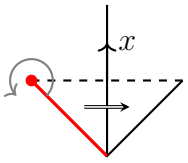

$$F^{(h,g)}(\tau) \mid x\rangle = \delta_{g,e} \mid \bar{h}x\rangle$$

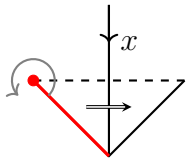

$$F^{(h,g)}(\tau) \mid x\rangle = \delta_{g,e} \mid xh\rangle$$

With the new formula above, we have,

$$\begin{aligned}
& B_{h'}(s_0)F^{(h,g)}(\tau) \mid x_1\ x_2\ x_3\ x_4\rangle \\
= \ & B_{h'}(s_0)\delta_{g,e} \mid \bar{h}x_1\ x_2\ x_3\ x_4\rangle \\
= \ & \delta_{h',\bar{h}x_1x_2x_3x_4}\delta_{g,e} \mid \bar{h}x_1\ x_2\ x_3\ x_4\rangle \\
= \ & \delta_{g,e}\delta_{hh',x_1x_2x_3x_4} \mid \bar{h}x_1\ x_2\ x_3\ x_4\rangle \\
= \ & F^{(h,g)}(\tau)\delta_{hh',x_1x_2x_3x_4} \mid x_1\ x_2\ x_3\ x_4\rangle \\
= \ & F^{(h,g)}(\tau)B_{hh'}(s_0) \mid x_1\ x_2\ x_3\ x_4\rangle
\end{aligned}$$

A.3 Multiplication of ribbon operators on elementary ribbons

A.3.1 For locally clockwise ribbons τ_L

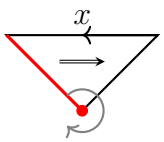

$$
\begin{aligned}
& F^{(h_1,f_1)}(\tau_L)F^{(h_2,f_2)}(\tau_L) \mid x\rangle \\
= & \sum_{(x)} F^{(h_1,f_1)}(\tau_L)\epsilon(h_2)f_2[S(x'')] \mid x'\rangle \\
= & \sum_{(x)} \epsilon(h_2)\epsilon(h_1)f_2[S(x''')]f_1[S(x'')] \mid x'\rangle \\
= & \sum_{(x)} \epsilon(h_1h_2)\langle f_2 \otimes f_1, \Delta[S(x'')]\rangle \mid x'\rangle \\
= & F^{(h_1h_2,f_2f_1)}(\tau_L) \mid x\rangle
\end{aligned}
$$

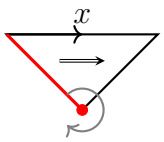

$$
\begin{aligned}
& F^{(h_1,f_1)}(\tau_L)F^{(h_2,f_2)}(\tau_L) \mid x\rangle \\
= & \sum_{(x)} F^{(h_1,f_1)}(\tau_L)\epsilon(h_2)f_2(x') \mid x''\rangle \\
= & \sum_{(x)} \epsilon(h_2)\epsilon(h_1)f_2(x')f_1(x'') \mid x'''\rangle \\
= & \sum_{(x)} \epsilon(h_1h_2)\langle f_2 \otimes f_1, \Delta(x')\rangle \mid x''\rangle \\
= & F^{(h_1h_2,f_2f_1)}(\tau_L) \mid x\rangle
\end{aligned}
$$

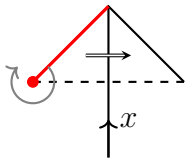

$$
\begin{aligned}
& F^{(h_1,f_1)}(\tau_L)F^{(h_2,f_2)}(\tau_L) \mid x\rangle \\
= \;& F^{(h_1,f_1)}(\tau_L)\epsilon(f_2) \mid xS(h_2)\rangle \\
= \;& \epsilon(f_2)\epsilon(f_1) \mid xS(h_2)S(h_1)\rangle \\
= \;& \epsilon(f_2f_1) \mid xS(h_1h_2)\rangle \\
= \;& F^{(h_1h_2,f_2f_1)}(\tau_L) \mid x\rangle
\end{aligned}
$$

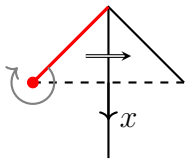

$$
\begin{aligned}
& F^{(h_1,f_1)}(\tau_L)F^{(h_2,f_2)}(\tau_L) \mid x\rangle \\
= \;& F^{(h_1,f_1)}(\tau_L)\epsilon(f_2) \mid h_2x\rangle \\
= \;& \epsilon(f_2)\epsilon(f_1) \mid h_1h_2x\rangle \\
= \;& F^{(h_1h_2,f_2f_1)}(\tau_L) \mid x\rangle
\end{aligned}
$$

A.3.2 For locally counterclockwise ribbons τ_R

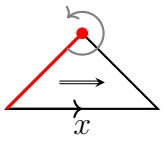

$$
\begin{aligned}
& F^{(h_1,f_1)}(\tau_R)F^{(h_2,f_2)}(\tau_R) \mid x\rangle \\
= \;& \sum_{(x)} F^{(h_1,f_1)}(\tau_R)\epsilon(h_2)f_2(x'') \mid x'\rangle \\
= \;& \sum_{(x)} \epsilon(h_2)\epsilon(h_1)f_2(x''')f_1(x'') \mid x'\rangle \\
= \;& \sum_{(x)} \epsilon(h_2h_1)\langle f_1 \otimes f_2, \Delta(x'')\rangle \mid x'\rangle \\
= \;& F^{(h_2h_1,f_1f_2)}(\tau_R) \mid x\rangle
\end{aligned}
$$

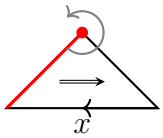

$$
\begin{aligned}
& F^{(h_1,f_1)}(\tau_R)F^{(h_2,f_2)}(\tau_R) \mid x\rangle \\
= & \sum_{(x)} F^{(h_1,f_1)}(\tau_R)\epsilon(h_2)f_2[S(x')] \mid x''\rangle \\
= & \sum_{(x)} \epsilon(h_2)\epsilon(h_1)f_2[S(x')]f_1[S(x'')] \mid x'''\rangle \\
= & \sum_{(x)} \epsilon(h_2h_1)\langle f_1 \otimes f_2, \Delta[S(x')]\rangle \mid x''\rangle \\
= & F^{(h_2h_1,f_1f_2)}(\tau_R) \mid x\rangle
\end{aligned}
$$

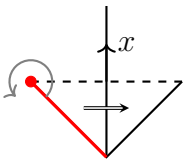

$$
\begin{aligned}
& F^{(h_1,f_1)}(\tau_R)F^{(h_2,f_2)}(\tau_R) \mid x\rangle \\
= & F^{(h_1,f_1)}(\tau_R)\epsilon(f_2) \mid S(h_2)x\rangle \\
= & \epsilon(f_2)\epsilon(f_1) \mid S(h_1)S(h_2)x\rangle \\
= & \epsilon(f_1f_2) \mid S(h_2h_1)x\rangle \\
= & F^{(h_2h_1,f_1f_2)}(\tau_R) \mid x\rangle
\end{aligned}
$$

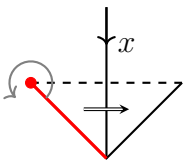

$$
\begin{aligned}
& F^{(h_1,f_1)}(\tau_R)F^{(h_2,f_2)}(\tau_R) \mid x\rangle \\
= & F^{(h_1,f_1)}(\tau_R)\epsilon(f_2) \mid xh_2\rangle \\
= & \epsilon(f_2)\epsilon(f_1) \mid xh_2h_1\rangle \\
= & \epsilon(f_1f_2) \mid xh_2h_1\rangle \\
= & F^{(h_2h_1,f_1f_2)}(\tau_R) \mid x\rangle
\end{aligned}
$$

A.4 Proof of Lemma 2.3.1

The idea is to first prove the equations in Lemma 2.3.1 for ribbons as short as possible, and then extend them to longer ribbons. It turns out that the shortest ribbon for some of the equations to hold is a triangle (direct or dual), while for others is a 2-triangle. For example, see the ribbon in Subsection A.4.1. Equation 2.63a does not hold for the rightmost triangle alone. This is roughly because for that triangle, its initial site and terminal site share the same vertex so that $A_a(s_0)$ would also act on s_1, which is unexpected. As will be shown below, the equation does hold as long as we make the triangle a bit longer. This is not a problem since we are only interested in properties of sufficiently long ribbons.

Subsections A.4.1-A.4.8 each addresses an identity in Equations 2.63a - 2.64d for the shortest possible ribbon. For each of the eight equations, there are two types of triangles (direct or dual) to consider. To avoid lengthy calculations, we only present the details for one of the two types for each equation. The proof for the other cases is similar. If a triangle does not work, then we lengthen it to a 2-triangle. In Subsection A.4.9 we extend the results to longer ribbons for Equations 2.63b and 2.63c while leave the other six cases as an exercise (whose proof is similar as well).

A.4.1 Equation 2.63a for short ribbons

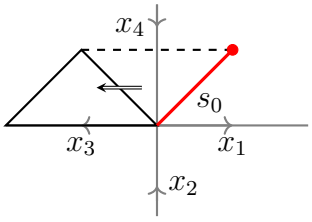

$$
\begin{aligned}
&A_a(s_0)F^{(h,f)}(\tau_L) \mid x_1\ x_4\ x_3\ x_2\rangle \\
&= A_a(s_0) \sum_{(i),i,(h)} F^{(h',g_i)}(\tau_1)F^{[S(i''')h''i',f(i''?)]}(\tau_2) \mid x_1\ x_4\ x_3\ x_2\rangle \\
&= A_a(s_0) \sum_{(h),(i),i,(x_3)} F^{(h',g_i)}(\tau_1)\epsilon[S(i''')h''i']f(i''x_3') \mid x_1\ x_4\ x_3''\ x_2\rangle \\
&= A_a(s_0) \sum_{(h),(i),i,(x_3)} \epsilon(g_i)\epsilon[S(i''')h''i']f(i''x_3') \mid x_1\ x_4S(h')\ x_3''\ x_2\rangle \\
&= A_a(s_0) \sum_{(e),(x_3),(h)} \epsilon(e''')\epsilon(h'')\epsilon(e')f(e''x_3') \mid x_1\ x_4S(h')\ x_3''\ x_2\rangle \\
&= \sum_{(a),(x_3),(h)} f(ex_3') \mid a^{(4)}x_1\ x_4S(h')S(a')\ a''x_3''\ x_2S(a''')\rangle \\
&= \sum_{(a),(x_3)} f[\epsilon(a'')x_3'] \mid a^{(5)}x_1\ x_4\epsilon(a^{(6)})S(h)S(a')\ a'''x_3''\ x_2S(a^{(4)})\rangle \\
&= \sum_{(a),(x_3)} f[S(a'')ea'''x_3'] \mid a^{(6)}x_1\ x_4S(h)S(a')\ a^{(4)}x_3''\ x_2S(a^{(5)})\rangle \\
&= \sum_{(i),i,(h),(x_3),(a)} \epsilon(g_i)\epsilon(i''')\epsilon\{[a''h''S(a^{(4)})]\}\epsilon(i')f[S(a''')i''a^{(7)}x_3'] \\
&\qquad \mid a^{(10)}x_1\ x_4S(a^{(6)})S\{[a'h'S(a^{(5)})]\}\ a^{(8)}x_3''\ x_2S(a^{(9)})\rangle \\
&= \sum_{(i),i,(x_3),(a),(x_3)} F^{\{[a'hS(a''')]',g_i\}}(\tau_1)\epsilon\{S(i''')[a'hS(a''')]''i'\}f[S(a'')i''(a''')'x_3'] \\
&\qquad \mid a^{(7)}x_1\ x_4S(a^{(4)})\ (a^{(5)})''x_3''\ x_2S(a^{(6)})\rangle \\
&= \sum_{(i),i,(a),(a'hS(a'''))} F^{\{[a'hS(a''')]',g_i\}}(\tau_1)F^{\{S(i''')[a'hS(a^{(3)})]''i',f[S(a'')i''?]\}}(\tau_2) \\
&\qquad \mid a^{(7)}x_1\ x_4S(a^{(4)})\ a^{(5)}x_3\ x_2S(a^{(6)})\rangle \\
&= \sum_{(i),(a)} F^{\{a'hS(a'''),f[S(a'')?]\}}(\tau_L) \mid a^{(7)}x_1\ x_4S(a^{(4)})\ a^{(5)}x_3\ x_2S(a^{(6)})\rangle \\
&= \sum_{(i),(a)} F^{\{a'hS(a^{(3)}),f[S(a'')?]\}}(\tau_L)A_{a^{(4)}}(s_0) \mid x_1\ x_4\ x_3\ x_2\rangle
\end{aligned}
$$

From the fourth line to the fifth line above, we used $\epsilon(g_i) = g_i(e)$ and

$$\sum_{(i),i} g_i(a)i'f(i'') = \sum_{(a)} a'f(a'').$$

To derive the above equality, note that,

$$\sum_{(a)} a' f(a'') = (Id \otimes f)\Delta(a) = (Id \otimes f)\Delta\left(\sum_i g_i(a) i\right).$$

A.4.2 Equation 2.63b for short ribbons

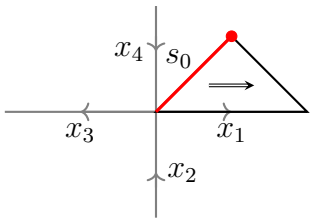

$$\begin{aligned}
&A_a(s_0)F^{(h,f)}(\tau_R) \mid x_1\ x_4\ x_3\ x_2\rangle \\
&= A_a(s_0)\sum_{(x_1)} \epsilon(h) f(x_1'') \mid x_1'\ x_4\ x_3\ x_2\rangle \\
&= \sum_{(x_1),(a)} \epsilon(h) f(x_1'') \mid a^{(4)}x_1'\ x_4 S(a')\ a'' x_3\ x_2 S(a''')\rangle \\
&= \sum_{(x_1),(a)} \epsilon(a^{(6)})\epsilon(h)\epsilon(a^{(8)}) f[S(a^{(7)})a^{(5)}x_1''] \mid a^{(4)}x_1'\ x_4 S(a')\ a'' x_3\ x_2 S(a''')\rangle \\
&= \sum_{(x_1),(a)} \epsilon[a^{(5)}hS(a^{(7)})] f[S(a^{(6)})(a^{(4)}x_1)''] \mid (a^{(4)}x_1)'\ x_4 S(a')\ a'' x_3\ x_2 S(a''')\rangle \\
&= \sum_{(a)} F^{\{a^{(5)}hS(a^{(7)}), f[S(a^{(6)})?]\}}(\tau_R) \mid a^{(4)}x_1\ x_4 S(a')\ a'' x_3\ x_2 S(a''')\rangle \\
&= \sum_{(a)} F^{\{a''hS(a^{(4)}), f[S(a''')?]\}}(\tau_R) A_{a'}(s_0) \mid x_1\ x_4\ x_3\ x_2\rangle
\end{aligned}$$

A.4.3 Equation 2.63c for short ribbons

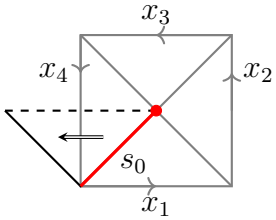

$$
\begin{aligned}
& B_t(s_0)F^{(h,f)}(\tau_L) \mid x_1\ x_2\ x_3\ x_4\rangle \\
&= B_t(s_0)\epsilon(f) \mid x_1\ x_2\ x_3\ x_4 S(h)\rangle \\
&= \sum_{(x_i),(h)} \epsilon(f)t[x_1'' x_2'' x_3'' x_4'' S(h')] \mid x_1'\ x_2'\ x_3'\ x_4' S(h'')\rangle \\
&= \sum_{(x_i),(h)} F^{(h'',f)}(\tau_L)t[x_1'' x_2'' x_3'' x_4'' S(h')] \mid x_1'\ x_2'\ x_3'\ x_4'\rangle \\
&= \sum_{(h)} F^{(h'',f)}(\tau_L)B_{t[?S(h')]}(s_0) \mid x_1\ x_2\ x_3\ x_4\rangle
\end{aligned}
$$

A.4.4 Equation 2.63d for short ribbons

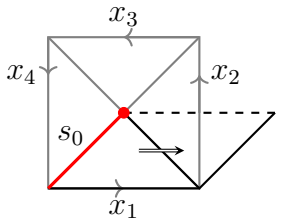

$$
\begin{aligned}
&B_t(s_0)F^{(h,f)}(\tau_R) \mid x_1\ x_2\ x_3\ x_4\rangle \\
&= B_t(s_0) \sum_{(h),i,(i)} F^{(h',g_i)}(\tau_1)F^{[S(i''')h''i',f(i''?)]}(\tau_2) \mid x_1\ x_2\ x_3\ x_4\rangle \\
&= B_t(s_0) \sum_{(h),i,(i)} F^{(h',g_i)}(\tau_1)\epsilon[f(i''?)] \mid x_1\ S[S(i''')h''i']x_2\ x_3\ x_4\rangle \\
&= B_t(s_0) \sum_{(h),i,(i),(x_1)} \epsilon(h')g_i(x_1'')f(i'') \mid x_1'\ S(i')S(h'')i'''x_2\ x_3\ x_4\rangle \\
&= B_t(s_0) \sum_{(x_1)} f(x_1''') \mid x_1'\ S(x_1'')S(h)x_1^{(4)}x_2\ x_3\ x_4\rangle \\
&= \sum_{(h),(x_i)} f(x_1^{(5)})t[x_1''S(x_1''')S(h')x_1^{(7)}x_2''x_3''x_4''] \mid x_1'\ S(x_1^{(4)})S(h'')x_1^{(6)}x_2'\ x_3'\ x_4'\rangle \\
&= \sum_{(h),(x_i)} f(x_1^{(4)})t[\epsilon(x_1'')S(h')x_1^{(6)}x_2''x_3''x_4''] \mid x_1'\ S(x_1''')S(h'')x_1^{(5)}x_2'\ x_3'\ x_4'\rangle \\
&= \sum_{(h),(x_i)} f(x_1''')t[S(h)x_1^{(5)}x_2''x_3''x_4''] \mid x_1'\ S(x_1'')S(h'')x_1^{(4)}x_2'\ x_3'\ x_4'\rangle \\
&= \sum_{(h),(x_i),i,(i)} \epsilon(h'')g_i(x_1'')f(i'')t[S(h')x_1''x_2''x_3''x_4''] \mid x_1'\ S(i')S(h''')i'''x_2'\ x_3'\ x_4'\rangle \\
&= \sum_{(h),(x_i),i,(i)} F^{(h'',g_i)}(\tau_1)\epsilon[f(i''?)]t[S(h')x_1''x_2''x_3''x_4''] \mid x_1'\ S[S(i''')h'''i']x_2'\ x_3'\ x_4'\rangle \\
&= \sum_{(h),(x_i),i,(i)} F^{(h'',g_i)}(\tau_1)F^{[S(i''')h'''i',f(i''?)]}(\tau_2)t[S(h')x_1''x_2''x_3''x_4''] \mid x_1'\ x_2'\ x_3'\ x_4'\rangle \\
&= \sum_{(h),(x_i)} F^{(h'',f)}(\tau_R)t[S(h')x_1''x_2''x_3''x_4''] \mid x_1'\ x_2'\ x_3'\ x_4'\rangle \\
&= \sum_{(h)} F^{(h'',f)}(\tau_R)B_{t[S(h')?]}(s_0) \mid x_1\ x_2\ x_3\ x_4\rangle
\end{aligned}
$$

A.4.5 Equation 2.64a for short ribbons

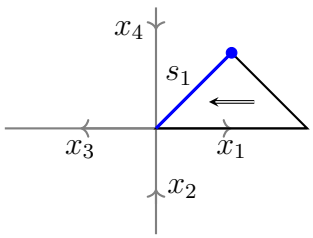

$$
\begin{aligned}
&A_a(s_1)F^{(h,f)}(\tau_L) \mid x_1\ x_4\ x_3\ x_2\rangle \\
&= A_a(s_1)\sum_{(x_1)} \epsilon(h)f(x_1'') \mid x_1'\ x_4\ x_3\ x_2\rangle \\
&= \sum_{(x_1),(a)} \epsilon(h)f[S(x_1'')] \mid a^{(4)}x_1'\ x_4 S(a')\ a''x_3\ x_2 S(a''')\rangle \\
&= \sum_{(x_1),(a)} \epsilon(h)f[S(x_1'')\epsilon(a^{(5)})] \mid a^{(4)}x_1'\ x_4 S(a')\ a''x_3\ x_2 S(a''')\rangle \\
&= \sum_{(x_1),(a)} \epsilon(h)f[S(x_1'')S(a^{(5)})a^{(6)}] \mid a^{(4)}x_1'\ x_4 S(a')\ a''x_3\ x_2 S(a''')\rangle \\
&= \sum_{(a)} F^{[h,f(?a^{(5)})]}(\tau_L) \mid a^{(4)}x_1\ x_4 S(a')\ a''x_3\ x_2 S(a''')\rangle \\
&= \sum_{(a)} F^{[h,f(?a'')]}(\tau_L)A_{a'}(s_1) \mid x_1\ x_4\ x_3\ x_2\rangle
\end{aligned}
$$

A.4.6 Equation 2.64b for short ribbons

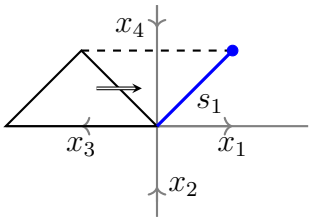

$$
\begin{aligned}
&A_a(s_1)F^{(h,f)}(\tau_R) \mid x_1\ x_4\ x_3\ x_2\rangle \\
&= A_a(s_1) \sum_{(i),i,(h)} F^{(h',g_i)}(\tau_1)F^{[S(i''')h''i',f(i''?)]}(\tau_2) \mid x_1\ x_4\ x_3\ x_2\rangle \\
&= A_a(s_1) \sum_{(i),i,(h)} F^{(h',g_i)}(\tau_1)\epsilon[f(i'?)] \mid x_1\ x_4 S(i''')h''i'\ x_3\ x_2\rangle \\
&= A_a(s_1) \sum_{(i),i,(h),(x_3)} \epsilon(h')g_i[S(x_3')]f(i'') \mid x_1\ x_4 S(i''')h''i'\ x_3''\ x_2\rangle \\
&= \sum_{(x_3)} A_a(s_1)f[S(x_3'')] \mid x_1\ x_4 x_3' h S(x_3''')\ x_3^{(4)}\ x_2\rangle \\
&= \sum_{(a),(x_3)} f[S(x_3'')] \mid a^{(4)}x_1\ x_4 x_3' h S(x_3''')S(a')\ a'' x_3^{(4)}\ x_2 S(a''')\rangle \\
&= \sum_{(a),(x_3)} f[S(x_3'')S(a'')a'] \mid a^{(6)}x_1\ x_4 x_3' h S(x_3''')S(a''')\ a^{(4)}x_3^{(4)}\ x_2 S(a^{(5)})\rangle \\
&= \sum_{(a),(x_3)} f[S(a^{(4)}x_3'')a'] \mid a^{(8)}x_1\ x_4 S(a'')a''' x_3' h S(x_3''')S(a^{(5)})\ a^{(6)}x_3^{(4)}\ x_2 S(a^{(7)})\rangle \\
&= \sum_{(a),(i),i,(h),(x_3)} \epsilon(h')g_i[S(a''' x_3')]\epsilon[f(i''?a')] \\
&\qquad\qquad \mid a^{(6)}x_1\ x_4 S(a'')S(i''')h''i'\ a^{(4)}x_3''\ x_2 S(a^{(5)})\rangle \\
&= \sum_{(a),(i),i,(h)} F^{(h',g_i)}(\tau_1)\epsilon[f(i''?a')] \mid a^{(5)}x_1\ x_4 S(a'')S(i''')h''i'\ a''' x_3\ x_2 S(a^{(4)})\rangle \\
&= \sum_{(a),(i),i,(h)} F^{(h',g_i)}(\tau_1)F^{[S(i''')h''i',f(i''?a')]}(\tau_2) \mid a^{(5)}x_1\ x_4 S(a'')\ a''' x_3\ x_2 S(a^{(4)})\rangle \\
&= \sum_{(a)} F^{[h,f(?a')]}(\tau_R) \mid a^{(5)}x_1\ x_4 S(a'')\ a''' x_3\ x_2 S(a^{(4)})\rangle \\
&= \sum_{(a)} F^{[h,f(?a')]}(\tau_R)A_{a''}(s_1) \mid x_1\ x_4\ x_3\ x_2\rangle
\end{aligned}
$$

A.4.7 Equation 2.64c for short ribbons

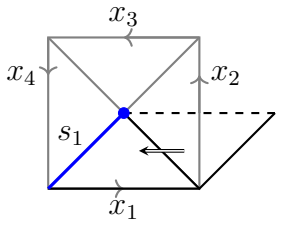

$$
\begin{aligned}
& B_t(s_1)F^{(h,f)}(\tau_L) \mid x_1\ x_2\ x_3\ x_4\rangle \\
&= B_t(s_1) \sum_{(h),i,(i)} F^{(h',g_i)}(\tau_1)F^{[S(i''')h''i',f(i''?)]}(\tau_2) \mid x_1\ x_2\ x_3\ x_4\rangle \\
&= B_t(s_1) \sum_{(h),i,(i),(x_1)} F^{(h',g_i)}(\tau_1)\epsilon[S(i''')h''i']f(i''x_1') \mid x_1''\ x_2\ x_3\ x_4\rangle \\
&= B_t(s_1) \sum_{(h),i,(i),(x_1)} \epsilon(g_i)\epsilon(i''')\epsilon(h'')\epsilon(i')f(i''x_1') \mid x_1''\ x_2S(h')\ x_3\ x_4\rangle \\
&= \sum_{(x_1)} B_t(s_1)f(x_1') \mid x_1''\ x_2S(h)\ x_3\ x_4)\rangle \\
&= \sum_{(x_i),(h)} f(x_1')t[S(x_1'')h''S(x_2')S(x_3')S(x_4')] \mid x_1'''\ x_2''S(h')\ x_3''\ x_4''\rangle \\
&= \sum_{(x_i),(h)} f(x_1''')t[S(x_1^{(4)})h''x_1''S(x_1')S(x_2')S(x_3')S(x_4')] \mid x_1^{(5)}\ x_2''S(h')\ x_3''\ x_4''\rangle \\
&= \sum_{(x_i),i,(i),(h)} f(i'')g_i(x_1'')t[S(i''')h''i'S(x_1')S(x_2')S(x_3')S(x_4')] \mid x_1'''\ x_2''S(h')\ x_3''\ x_4''\rangle \\
&= \sum_{(x_i),i,(i),j,(j),(h)} f(i'')\epsilon(g_i)\epsilon(j''')\epsilon(h'')\epsilon(j')g_i(j''x_1'') \\
&\qquad t[S(i''')h''i'S(x_1')S(x_2')S(x_3')S(x_4')] \mid x_1'''\ x_2''S(h')\ x_3''\ x_4''\rangle \\
&= \sum_{(x_i),i,(i),j,(j),(h)} f(i'')F^{(h',g_i)}(\tau_1)\epsilon[S(j''')h''j']g_i(j''x_1'') \\
&\qquad t[S(i''')h''i'S(x_1')S(x_2')S(x_3')S(x_4')] \mid x_1'''\ x_2''\ x_3''\ x_4''\rangle \\
&= \sum_{(x_i),i,(i),j,(j),(h)} f(i'')F^{(h',g_i)}(\tau_1)F^{[S(j''')h''j',g_i(j''?)]}(\tau_2) \\
&\qquad t[S(i''')h''i'S(x_1')S(x_2')S(x_3')S(x_4')] \mid x_1''\ x_2''\ x_3''\ x_4''\rangle \\
&= \sum_{(x_i),i,(i),(h)} f(i'')F^{(h',g_i)}(\tau_L)t[S(i''')h''i'S(x_1')S(x_2')S(x_3')S(x_4')] \mid x_1''\ x_2''\ x_3''\ x_4''\rangle \\
&= \sum_{i,(i),(h)} f(i'')F^{(h',g_i)}(\tau_L)B_{t[S(i''')h''i'?]}(s_1) \mid x_1\ x_2\ x_3\ x_4\rangle
\end{aligned}
$$

A.4.8 Equation 2.64d for short ribbons

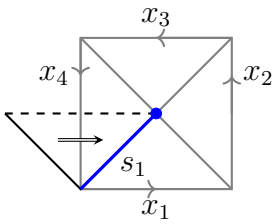

$$
\begin{aligned}
&B_t(s_1)F^{(h,f)}(\tau_R) \mid x_1\ x_2\ x_3\ x_4\rangle \\
&= B_t(s_1)\epsilon(f) \mid x_1\ x_2\ x_3\ x_4 S(h)\rangle \\
&= \sum_{(x_i),(h)} f(e)t(x_1''x_2''x_3''x_4''h'') \mid x_1'\ x_2'\ x_3'\ x_4'h'\rangle \\
&= \sum_{(x_i),(h),i,(i)} f(i'')\epsilon(g_i)t[x_1''x_2''x_3''x_4''S(i''')h''i'](s_1) \mid x_1'\ x_2'\ x_3'\ x_4'h'\rangle \\
&= \sum_{(x_i),(h),i,(i)} f(i'')F^{(h',g_i)}(\tau_R)t[x_1''x_2''x_3''x_4''S(i''')h''i'](s_1) \mid x_1'\ x_2'\ x_3'\ x_4'\rangle \\
&= \sum_{(h),i,(i)} f(i'')F^{(h',g_i)}(\tau_R)B_{t[?S(i''')h''i']}(s_1) \mid x_1\ x_2\ x_3\ x_4\rangle
\end{aligned}
$$

A.4.9 Equations 2.63b and 2.63c for long ribbons

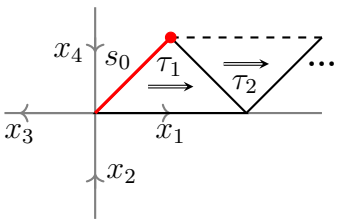

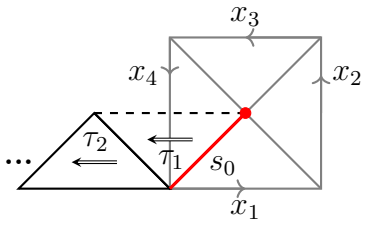

For the left figure above, we have,

$$
\begin{aligned}
& A_a(s_0)F^{(h,f)}(\tau_R) \\
= & \sum_{(h),i,(i)} A_a(s_0)F^{(h',g_i)}(\tau_1)F^{[S(i''')h''i',f(i''?)]}(\tau_2) \\
= & \sum_{(a),(h),i,(i)} F^{\{a''h'S(a^{(4)}),g_i[S(a''')?]\}}(\tau_1)A_{a''}(s_0)F^{[S(i''')h''i',f(i''?)]}(\tau_2) \\
= & \sum_{(a),(h),i,(i)} F^{\{a''h'S(a^{(4)}),g_i[S(a''')?]\}}(\tau_1)F^{[S(i''')h''i',f(i''?)]}(\tau_2)A_{a'}(s_0) \\
= & \sum_{(a),(h),i,(i),j} F^{\{a''h'S(a^{(4)}),g_i[S(a''')j]g_j(?)\}}(\tau_1)F^{[S(i''')h''i',f(i''?)]}(\tau_2)A_{a''}(s_0) \\
= & \sum_{(a),(h),j,(j)} F^{[a''h'S(a^{(6)}),g_j]}(\tau_1)F^{\{S(j''')a'''h''S(a^{(5)})j',f[S(a^{(4)})j''?]\}}(\tau_2)A_{a'}(s_0) \\
= & \sum_{(a),(h)} F^{\{a''hS(a^{(4)}),f[S(a''')?]\}}(\tau_R)A_{a'}(s_0)
\end{aligned}
$$

From the forth line to the fifth line in the above equation, we need to use

$$
\begin{aligned}
g_i(a\ b) = g_i\left[a\sum_j g_j(b)j\right] = \sum_j g_i(a\ j)g_j(b) \\
\Longrightarrow g_i(a\ ?) = \sum_j g_i(a\ j)g_j(?).
\end{aligned}
$$

For the right figure above,

$$
\begin{aligned}
& B_t(s_0)F^{(h,f)}(\tau_L) \\
= & \sum_{(h),i,(i)} B_t(s_0)F^{(h',g_i)}(\tau_1)F^{[S(i''')h''i',f(i''?)]}(\tau_2) \\
= & \sum_{(h),i,(i)} F^{(h'',g_i)}(\tau_1)B_{t[?S(h')]}(s_0)F^{[S(i''')h'''i',f(i''?)]}(\tau_2) \\
= & \sum_{(h),i,(i)} F^{(h'',g_i)}(\tau_1)F^{[S(i''')h'''i',f(i''?)]}(\tau_2)B_{t[?S(h')]}(s_0) \\
= & \sum_{(h)} F^{(h'',f)}(\tau_L)B_{t[?S(h')]}(s_0)
\end{aligned}
$$

A.5 Proof of Proposition 2.3.2

We are going to talk about Hamiltonian terms where a is the Haar integral of H and t is the Haar integral of H^* temporarily. Notice that the Haar integral is cocomutative, and so we can cyclically rotate the components a', a'', a''', etc. Below we prove the commutation relation for locally clockwise ribbons, and leave the details for locally counterclockwise ribbons to the reader.

A.5.1 Equation 2.65a

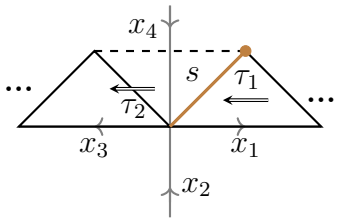

$$
\begin{aligned}
& A_a(s)F^{h,f}(\tau_L) \\
&= \sum_{(h),i,(i)} A_a(s)F^{(h',g_i)}(\tau_1)F^{[S(i''')h''i',f(i''?)]}(\tau_2) \\
&= \sum_{(h),i,(i),(a)} F^{[h',g_i(?a'')]}(\tau_1)A_{a'}(s)F^{[S(i''')h''i',f(i''?)]}(\tau_2) \\
&= \sum_{(h),i,(i),(a)} F^{[h',g_i(?a^{(5)})]}(\tau_1)F^{\{a'S(i''')h''i'S(a'''),f[i''S(a'')?]\}}(\tau_2)A_{a^{(4)}}(s) \\
&= \sum_{(h),i,(i),(a),j} F^{[h',g_i(ja^{(5)})g_j(?)]}(\tau_1)F^{\{a'S(i''')h''i'S(a'''),f[i''S(a'')?]\}}(\tau_2)A_{a^{(4)}}(s) \\
&= \sum_{(h),(a),j,(j)} F^{(h',g_j)}(\tau_1)F^{\{a'S(a^{(7)})S(j''')h''j'a^{(5)}S(a'''),f[j''a^{(6)}S(a'')?]\}}(\tau_2)A_{a^{(4)}}(s) \\
&= \sum_{(h),(a),j,(j)} F^{(h',g_j)}(\tau_1)F^{\{S(j''')h''j'a^{(4)}S(a''),f[j''a^{(5)}S(a')?]\}}(\tau_2)A_{a'''}(s) \\
&= \sum_{(h),(a),j,(j)} F^{(h',g_j)}(\tau_1)F^{\{S(j''')h''j'a^{(3)}S(a'),f[j''?]\}}(\tau_2)A_{a''}(s) \\
&= \sum_{(h),j,(j)} F^{(h',g_j)}(\tau_1)F^{\{S(j''')h''j',f[j''?]\}}(\tau_2)A_a(s) \\
&= F^{h,f}(\tau_L)A_a(s)
\end{aligned}
$$

From the sixth line to the end in the above equation, we used the cocomutative condition of $a \in H$, the Haar integral of H. So we can rotate a' to $a^{(n_{max})}$ and $a^{(n)}$ to $a^{(n-1)}$ for $n > 1$. After the rotation, we obtain $\epsilon(a^{(n)})$ to lower the maximum order step by step.

A.5.2 Equation 2.65b

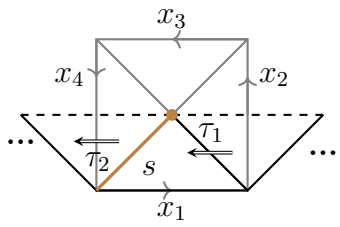

$$
\begin{aligned}
& B_t(s)F^{(h,f)}(\tau_L) \\
&= \sum_{(h),i,(i)} B_t(s)F^{(h',g_i)}(\tau_1)F^{[S(i''')h''i',f(i''?)]}(\tau_2) \\
&= \sum_{(h),i,(i),j,(j)} g_i(j'')F^{(h',g_j)}(\tau_1)B_{t[S(j''')h''j'?]}(S)F^{[S(i''')h'''i',f(i''?)]}(\tau_2) \\
&= \sum_{(h),i,(i),j,(j)} g_i(j'')F^{(h',g_j)}(\tau_1)F^{[S(i^{(4)})h^{(4)}i'',f(i'''?)]}(\tau_2) \\
&\qquad\qquad B_{t[S(j''')h''j'?S(i')S(h''')i^{(5)}]}(s) \\
&= \sum_{(h),j,(j)} F^{(h',g_j)}(\tau_1)F^{[S(j^{(5)})h^{(4)}j''',f(j^{(4)}?)]}(\tau_2)B_{t[S(j^{(7)})h''j'?S(j'')S(h''')j^{(6)}]}(s) \\
&= \sum_{(h),j,(j)} F^{(h',g_j)}(\tau_1)F^{[S(j^{(5)})h^{(4)}j''',f(j^{(4)}?)]}(\tau_2)B_{t[S(j'')S(h''')j^{(6)}S(j^{(7)})h''j'?]}(s) \\
&= \sum_{(h),j,(j)} F^{(h',g_j)}(\tau_1)F^{[S(j''')h''j',f(j''?)]}(\tau_2)B_t(s) \\
&= F^{(h,f)}(\tau_L)B_t(s)
\end{aligned}
$$

Similarly, from the last third line to the last second line, we used the cocomutative condition of $t \in H^*$, the Haar integral of H^*.

A.6 Fourier transformation of H^*

Let H be any finite dimensional $\mathbb{C}^*$ Hopf algebra. First, we define a Fourier transformation on H [64]:

$$
\mid \nu ab\rangle = \sqrt{\frac{dim(\nu)}{dim(H)}} \sum_{(h_0)} D^{\nu}(h_0')_{ab}h_0'', \quad \nu \in \mathrm{Irr}_H, a, b = 1, \cdots, dim(\nu),
$$

where Irr_H is the set of irreducible representations of H, and $D^{\nu}(h_0')_{ab}$ is the matrix entry of h_0' for the representation ν under a chosen (fixed) basis.

Recall from Section 2.2.2 that there are two commuting actions, L and R, of H on itself corresponding to multiplication on the left and multiplication on the right by $S(\cdot)$, respectively. We check the form of the two actions under the Fourier basis.

For an element $m \in H$, the action $L(m)$ is,

$$\begin{aligned} L(m) \mid \nu ab\rangle &= \sqrt{\frac{dim(\nu)}{dim(H)}} \sum_{(h_0)} D^{\nu}(h_0')_{ab} m h_0'' \\ &= \sqrt{\frac{dim(\nu)}{dim(H)}} \sum_{(h_0),(m)} D^{\nu}(h_0')_{ab} m' \epsilon(m'') h_0'' \\ &= \sqrt{\frac{dim(\nu)}{dim(H)}} \sum_{(h_0),(m)} D^{\nu}(h_0')_{ab} m' \epsilon[S(m'')] h_0''. \end{aligned}$$

As $xh_0 = \epsilon(x)h_0$, we have $\sum_{(x),(h_0)} x'h_0' \otimes x''h_0'' = \epsilon(x) \sum_{(h_0)} h_0' \otimes h_0''$. Applying the above identity for $x = S(m'')$, we obtain

$$\begin{aligned} L(m) \mid \nu ab\rangle &= \sqrt{\frac{dim(\nu)}{dim(H)}} \sum_{(h_0),(m)} D^{\nu}[S(m''')h_0']_{ab} m' S(m'') h_0'' \\ &= \sqrt{\frac{dim(\nu)}{dim(H)}} \sum_{(h_0)} D^{\nu}[S(m)h_0']_{ab} h_0'' \\ &= \sqrt{\frac{dim(\nu)}{dim(H)}} \sum_{(h_0),k} D^{\nu}[S(m)]_{ak} D^{\nu}(h_0')_{kb} h_0'' \\ &= \sum_k D^{\nu}[S(m)]_{ak} \mid \nu kb\rangle \\ &= \sum_k D^{\nu^*}[m]_{ka} \mid \nu kb\rangle. \end{aligned}$$

Similarly, we can obtain the action of $R(m)$:

$$R(m) \mid \nu ab\rangle = \sum_k D^{\nu}(m)_{kb} \mid \nu ak\rangle.$$

Now, take the dual basis $\{\langle \nu ab \mid\}$ in H^*. L and R each induces a representation on H^*, still denoted by the same letter. Then on the dual basis, the two actions are given by,

$$\begin{aligned} L(m)(\langle \nu ab \mid) &= \sum_k D^{\nu}(m)_{ka} \langle \nu kb \mid, \\ R(m)(\langle \nu ab \mid) &= \sum_k D^{\nu^*}(m)_{kb} \langle \nu ak \mid, \end{aligned}$$

Apply the above dual basis to $D(H)$, we obtain the desired basis for Equations 2.71 and 2.72.

B. SUPPLEMENTARY MATERIAL FOR CHAPTER 4

This chapter contains work from the article entitled "Generalized Kitaev spin liquid model and emergent twist defect" written by the author, Penghua Chen, and Shawn X. Cui published on Annals of Physics [2].

B.1 Perturbation treatment

B.1.1 Effective Hamiltonian

In this appendix, V represents the perturbation H' to avoid confusion. Consider the effective Hamiltonian:

$$H_{\text{eff}} = T\left(V + VG_0'V + VG_0'VG_0'V + \ldots\right)T \tag{B.1}$$

where $T = \mid GS\rangle\langle GS \mid$ is the projector onto the ground state of the system described by J_v, and $G_0' = \left(\frac{1}{E_0 - H_0}\right)'$. Here, the prime notation on G_0' indicates that it vanishes on the ground state and acts normally on the excited states.

In this appendix, V represents the perturbation H' to avoid confusion. For the effective Hamiltonian, we have:

$$H_{\text{eff}} = T\left(V + VG_0'V + VG_0'VG_0'V + \ldots\right)T \tag{B.2}$$

where $T = \mid GS\rangle\langle GS \mid$ is the projector onto the ground state of J_vs, and $G_0' = \left(\frac{1}{E_0 - H_0}\right)'$, indicating that G_0' vanishes on the ground state and acts normally on the excited states.

The perturbation tree, shown in Figure B.1, illustrates the general idea of the calculation. Each node of the diagram is labeled with a state Φ. The action of each check operator on $\mid \Phi_0\rangle = \mid GS\rangle$ will flip two terms in H_0, increasing the energy by 4. Applying another term in V on the intermediate state $\mid \Phi_1\rangle$ yields different outcomes based on the product of $P_{e_1} \times P_{e_2}$, where:

- If $\partial e_1 \cap \partial e_2 = \emptyset$, then we obtain $\mid \Phi_{23}\rangle$ with energy 8. - If $\partial e_1 = \partial e_2$, then we obtain $\mid \Phi_{21}\rangle$, reverting to the ground state. - The remaining possibility is that e_1 and e_2 share one common vertex, resulting in energy 4.

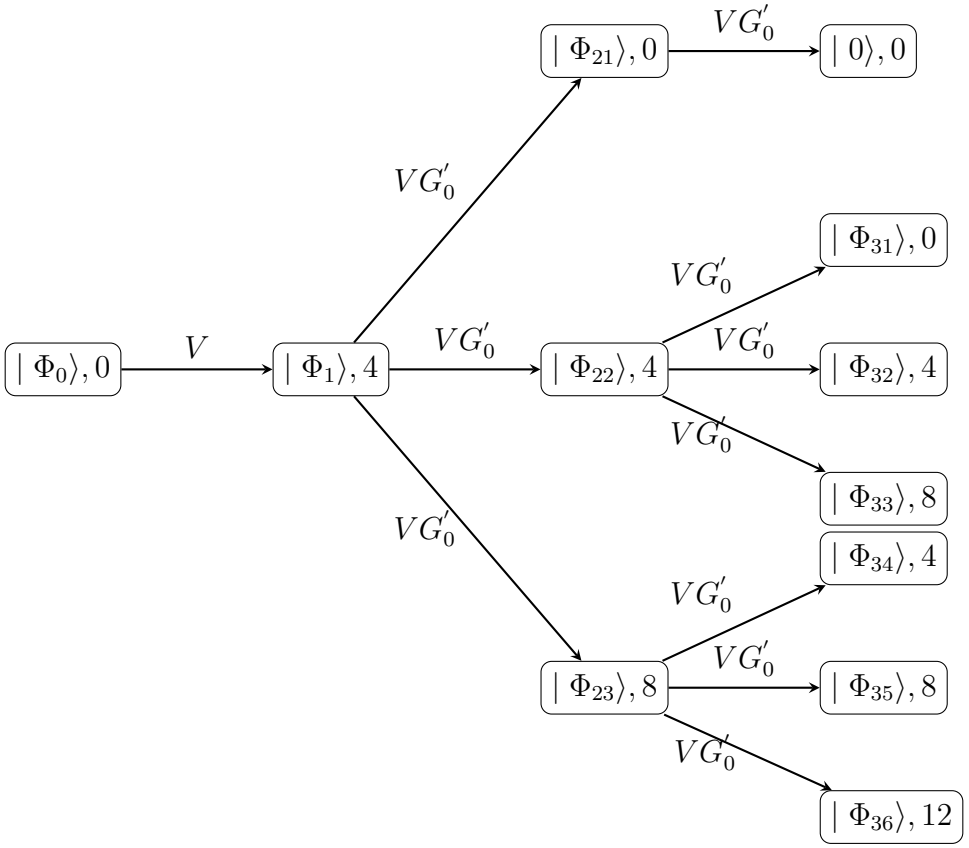

Figure B.1. Demostration of perturbation tree

Repeating this process for higher-order perturbations results in different sectors with varying energy levels, as shown in Figure B.1. The energy sector $\Phi_{i,j}$ reverting back to the ground state contributes to the i-th order of the effective Hamiltonian:

$$H^i_{\text{eff}} = \alpha_i \langle GS \mid V^i \mid GS \rangle \tag{B.3}$$

Where α_i is a path-dependent factor calculable from the diagram, named the geometric factor. Terms in V^i that do not vanish in the ground state are those that commute with all P_v. Generators could be $P_{e_i}P_{e_j}$, where $e_i = e_j$, contributing to a constant factor, or $\Pi_{e_j}P_{e_j}$, where e_j forms a closed loop, contributing to the plaquette term $W'_p = \Pi_{e \in Bo(p) | P_e \in H'} P_e$.

Thus, the effective Hamiltonian is:

$$H_{\text{eff}} = \sum_p (-1)^{\gamma_p} \alpha_{l_p} \lambda^{l_p} W_p + constant \tag{B.4}$$

Where l_p is the number of edges in W'_p. The factor λ^{l_p} arises from the dominant contribution in the l_p-th order perturbation. The cases of creation or fusion are handled differently, indicating a transformation of the plaquette, leading to alterations in the effective Hamiltonian despite maintaining the same eigenvalue.

B.1.2 Geometric Factor α_p

The geometric factor α_p needs to be evaluated via explicit calculation and we did not find a general formula for it. However, we are primarily concerned with cases where the factor $\alpha_p = 0$ as this scenario represents a hole in the surface code limit. We identify a family of plaquettes that would have $\alpha_p = 0$ when the corresponding plaquette operator consists of an odd number of anti-commutative check operator pairs. The proof is as follows:

Suppose we have a plaquette operator W'_p, which is a product of several perturbation check operators. The factor α_p is calculated in the l_p-th order of perturbation through the diagram shown in Figure B.1. For any permutation $\sigma \in S_{l_p}$, the product $\prod_i A_{\sigma(i)}$ has a nontrivial perturbation contribution to the plaquette operator W'_p, where S_n is the n-th order of the permutation group.

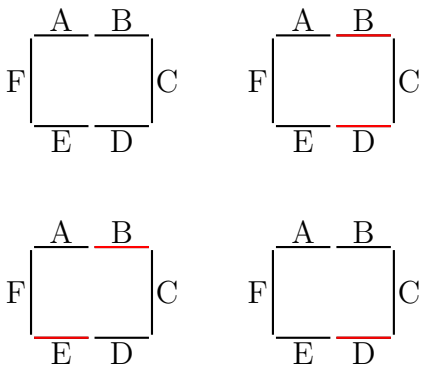

Figure B.2. The figures provided illustrate a plaquette consisting of six edges within a honeycomb lattice, where the red edges represent the dominant check operators, and the black edges denote perturbation terms. The figure in the top-right position depicts a typical scenario observed in the honeycomb lattice. In contrast, the figure in the bottom-left position shows the configuration after defects have been moved. The figure in the bottom-right position illustrates the state of the plaquette when a defect is present.

The perturbation contribution consists of two parts. One comes from the action of the Green's function, essentially derived from the path on the perturbation tree, denoted as Fg_σ. Then, the outcome of the perturbation can be written as $\alpha_p W_p' = \sum_{\sigma \in S_{l_p}} Fg_\sigma \prod_i A_{\sigma(i)}$. Thus, $\alpha_p = \sum_{\sigma \in S_{l_p}} Fg_\sigma Sg_\sigma$, where Sg_σ results from aligning $\prod_i A_{\sigma(i)}$ to a fixed form $W_p' = \prod_{i=1}^{l_p} A_i$, controlled simply by the commutation relation between A_is. Consider $\bar{\sigma}$: $\bar{\sigma}(i) = \sigma(l_p - i + 1)$, a function that is the reverse permutation of σ. Notice that reversing the order of check operators in the perturbation tree remains valid since it starts and ends in the ground state, and they have $Fg_\sigma = Fg_{\bar{\sigma}}$ due to symmetry.

The relative sign $\frac{Sg_\sigma}{Sg_{\bar{\sigma}}}$ is determined by converting $\prod_i A_{\sigma(i)}$ to $\prod_i A_{\bar{\sigma}(i)}$. For illustration, consider three elements A_1, A_2, A_3, and $\sigma(i) = i$, $\bar{\sigma}(i) = 3 - i$. The relative sign, determined by the commutation relations of A_is, depends on the parity of the anti-commutative pairs. The relative sign is -1 if W_p contains an odd number of anti-commutative pairs of check operators, and $+1$ if even, resulting in $\alpha_{l_p} = 0$ since the reverse permutation forms an equivalence relation in the permutation group S_{l_p}.

Remark 1: In a general lattice with vertices where $d_v = 4$, the coefficient of each W_p is no longer uniform. However, continuously deforming the coefficients of W_ps to be uniformly

large, regardless of the sign (as argued, the sign does not impact the toric code phase), is a continuous transformation that does not close the gap. Therefore, it maintains the same phase.

Remark 2: Concerns about cases where $\alpha_p = 0$ are significant because this factor is path-dependent and heavily reliant on the details of the lattice and the choice of S_c. However, for a zero α_p with multiple channels in the diagram shown in Figure B.1, we might find a nonzero $(l_p + 2)$-th order contribution by inserting a pair of P_{e_0} in the process to build up W_p, where $e_0 \notin Bo(p)$, into the perturbation tree. This change in the action of G_0' between the pair of P_{e_0}, being generally non-linear, might result in a nonzero effect. If it remains zero, further insertions could be attempted. Ultimately, W_p may survive in higher orders of perturbation theory.

Remark 3: In cases of a large plaquette in the lattice Γ, since l_p is large, λ^{l_p} is generally so small that this plaquette could be treated as a hole or a boundary, depending on its color. Alternatively, if some $\alpha_p = 0$ and cannot survive even under the argument of Remark 2, or it only survives in a very high order of perturbation, it also serves as a hole in the toric code model.

B.2 Mapping Table of vertex with $d_v > 4$

Consider a vertex with degree $d_v > 4$. Assuming $d_v = 2k$, there are k qubits placed on it. We define a k-order Pauli operator as a tensor product of k Pauli operators. We choose $P_v = \bigotimes_{i=1}^{k} Z$, where each Z acts on a different qubit. The eigenstate of P_v corresponding to the eigenvalue $+1$ represents the ground state for these qubits. The eigenspace associated with this eigenvalue is 2^{k-1}-dimensional. The task is to identify effective $k-1$ order Pauli operators from the set of k-order Pauli operators that commute with P_v. The generators of these commuting operators are of the following form:

$$\mathcal{X}_i = \underbrace{1 \otimes 1 \cdots 1}_{i-1} \otimes X \otimes X \otimes 1 \otimes \cdots 1 \otimes 1 \tag{B.5}$$

Here $\mathcal{X}$ represents a tensor product of k Pauli operators. $\mathcal{X}_i$ is explicitly two X operators at positions i and $i+1$, with the identity I at the others. We have obviously $k-1$ such operators $\{\mathcal{X}_i \mid i = 1, 2, \ldots, k-1\}$. Another set of generators are:

$$\mathcal{Z}_i = \underbrace{I \otimes I \cdots I}_{i-1} \otimes Z \otimes I \cdots I \tag{B.6}$$

Which means $\mathcal{Z}_i$ is one Z operator located at position i, with identity I at the others. We have k such operators, $\{\mathcal{Z}_i \mid i = 1, 2, \ldots, k\}$. Notice, $\mid \phi_0\rangle = \bigotimes_{j=1}^{k} \mid 0\rangle$ is one of the bases in the eigenspace. $\mathcal{X}_i \mid \phi_0\rangle$ effectively generates the whole eigenspace. Then we define the mapping of $\mathcal{X}_i$ to $k-1$ order operator:

$$\mathcal{X}_i \to \underbrace{I \otimes I \cdots I}_{i-1} \otimes X \otimes X \otimes I \cdots I \tag{B.7}$$

We denote the notation $\tilde{\mathcal{X}}_i$ to represent the effective action of $\mathcal{X}_i$ in the eigenspace of P_v. Notice on the right, it is a tensor product of $k-1$ Pauli operators. Similarly, $\tilde{\mathcal{Z}}_i$ represents the effective operator of $\mathcal{Z}_i$:

$$\tilde{\mathcal{Z}}_i = \underbrace{I \otimes I \cdots I}_{i-2} \otimes Z \otimes Z \otimes I \cdots I \otimes I \tag{B.8}$$

For $1 < i < k-1$, and $\tilde{\mathcal{Z}}_1 = Z \otimes I \cdots I \otimes I$, $\tilde{\mathcal{Z}}_k = I \otimes I \cdots I \otimes Z$. Notice the product of $\tilde{\mathcal{Z}}_i$ is 1, which agrees with $\prod_{i=1}^{k} \mathcal{Z}_i = P_v$. Then arranging the operators similarly as in Fig. 3.4b would give rise to the splitting of $d_v > 6$.

B.3 Possible Measurement-Based Initializing Method

We have emphasized that since each process is described by time evolution, it is natural to depict each process (movement, creation, and fusion) by a quantum circuit. Here, we describe a convenient measurement-based method to initialize a ground state of the effective toric code on a honeycomb lattice as shown in Figure B.3, which follows the same approach as in the Floquet code described in [73].

The method follows a measurement schedule:

First, measure the check operators associated with yellow edges.

Second, measure the check operators associated with blue edges.

Third, measure the check operators associated with red edges.

Repeat the routine above.

After the fourth step, the state achieves the ground state of all plaquette terms (with signs that depend on the measurement outcomes). We then proceed to measure the yellow checks (or equivalently, the elements in S_c) as depicted in Figure 3.6. Following this measurement, the state transitions into the ground state of the plaquette operators and the stabilizer center S_c, with the corresponding eigenvalues depending on the measurement outcomes. This process effectively generates the desired toric code. Subsequently, we can apply the unitary operator, as described by the time evolution operators in the previous section, to manipulate the twist defects.

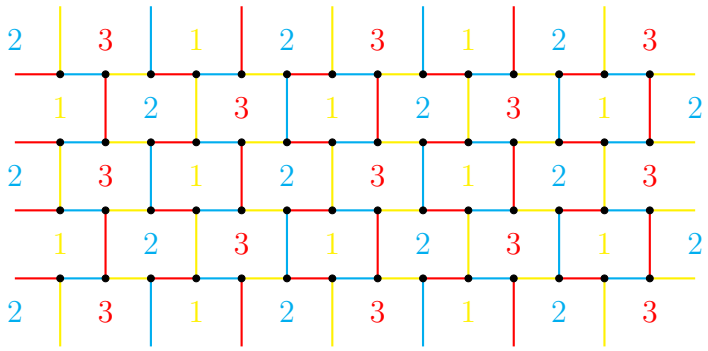

Figure B.3. This figure illustrates a honeycomb lattice used to initialize a ground state of the effective toric code, a platform that facilitates defect manipulation. Each edge is colored according to the plaquettes to which it is connected.

C. SUPPLEMENTARY MATERIAL FOR CHAPTER 4

This chapter contains work from the article entitled "Floquet Codes from Coupled Spin Chains" written by the author, Penghua Chen, and Shawn X. Cui published on arXiv [1].

C.1 The Instantaneous Phase of Floquet code in dimension 3

Consider a 3-dimensional Kitaev Spin Liquid(KSL) Hamiltonian:

$$H = \sum -J_x X \otimes X - J_Y Y \otimes Y - J_z Z \otimes Z \tag{C.1}$$

The arrangement of check operators is shown in figure 4.5a. Green/Blue checks are associated with $X \otimes X / Y \otimes Y$ operators and controlled by J_x / J_y, and red and black checks are all $Z \otimes Z$ operators, controlled by J_z. The check operators no longer always anti-commute when they are connected. When J_z is dominant, we will get the instantaneous phase at round $6r$. Each group of 4 qubits near each physical edge will falls into the $+1$ common eigenspace of operators $Z \otimes Z \otimes I \otimes I$, $I \otimes Z \otimes Z \otimes I$ and $I \otimes I \otimes Z \otimes Z$, thus become effective one qubit. Effective Pauli operators are generated by $\mathbf{Z} = Z \otimes I \otimes \cdots \otimes I$ and $\mathbf{X} = X \otimes X \otimes X \otimes X$. It is easy to see, the red stabilizers in SSG are products of $\mathbf{X}$ along the border of each plaquette and the blue/green stabilizers are products of $\mathbf{X}$ over each edges connected to the vertex. We shall note here, if one edge only borders odd number of qubits, that two vertex opertors that the edge connects will anticommute. So, the requirement of possible splitting of red and black checks agree with the commutativity of effective stabilizer operators. The above argument only require the whole lattice is vertex-2-colorable and each edge borders even number of plaquettes, which matchs the requirement of construcing the floquet code and works on general lattices. So it naturally works also in higher dimensions, thus will generate $(n, 1)$ toric code model at round $6r$.

For the X-cube construction, a unit cell of cubic lattice as shown in figure 4.10a, edges of the same color represents the edges from the same spin chain, and $Z \otimes Z$ inter-chain coupling are in between concussive qubits on the same edge. Effective operators are cubic terms, that are product of all check operators shown in this figure, and the vertices terms, that are

the product of check operators of the same color around a single vertex, noticing that the arrangement of edge operators are translational-invariant. Each edge is surrounded by 4 cube terms, and the action of them on this edge are $X\otimes X\otimes X\otimes X$, $X\otimes Y\otimes X\otimes Y$, $Y\otimes Y\otimes Y\otimes Y$, $Y\otimes X\otimes Y\otimes X$, respectively. They commute so they have the same effective representation $\mathbf{X}$. The action of vertex terms on each edge is the effective operator $\mathbf{Z}$. So they matches the Hamiltonian of X Cube model. The analysis works naturally to higher dimensions, thus permits n-dimensional instantaneous (4,1) toric code and generalized X-cube model.

C.2 A Trivalent 3D Kitaev Spin Liquid Model from Coupling Spin Chain

C.2.1 A Short Review of Binary Vector Representation of the Pauli Hamiltonian

Single-qubit Pauli operators, or the Pauli matrices, are denoted by X, Y, Z, or σ_x, σ_y, σ_z, satisfying

$$\sigma_i \cdot \sigma_j = \delta_{i,j} + i\epsilon_{ijk}\sigma_k.$$

Thus, the tensor product of Pauli matrices over finite support forms an abelian group P, with scalars of $\{\pm 1, \pm i\}$. When considering the stabilizer code, one can ignore the scalar coefficients, leading to the abelian Pauli group $P/\{\pm 1, \pm i\}$. Thus, we can define an $\mathbf{F}_2$ module vector representation for Pauli matrices as follows:

$$\text{Pauli-X} \mapsto \begin{bmatrix} 1 \\ 0 \end{bmatrix}, \quad \text{Pauli-Y} \mapsto \begin{bmatrix} 1 \\ 1 \end{bmatrix}, \quad \text{Pauli-Z} \mapsto \begin{bmatrix} 0 \\ 1 \end{bmatrix}.$$

To restate the commutation relation in this new language, we shall use the symplectic matrix.

$$\lambda = \begin{bmatrix} 0 & 1 \\ 1 & 0 \end{bmatrix}$$

We call the map $\tau : P \to V$ as V_P, where P is a Pauli operator, and V_P is the corresponding vector representation. The commutation relation $[P, P'] = 0$ is restated as $V_P^T \cdot \lambda \cdot V_P' = 0 \pmod 2$. Here, T denotes transpose.

For a Pauli operator that is the tensor product of K Pauli matrices, we can use a $2K$-dimensional vector to represent it, i.e., the direct sum of the vector representation of each Pauli matrix. We rearrange the vector so that the first (last) K entries mainly record the σ_x (σ_z) on K sites.

For a translationally invariant stabilizer code, one can write the Hamiltonian term in a compact form. An n-dimensional translationally invariant lattice is denoted as a binary polynomial ring $\mathbf{F}_2[x_1, x_2, \ldots, x_n]$. Suppose each unit cell of the lattice contains q qubits. Then a generator of a translationally invariant stabilizer code can be denoted as:

$$\mathrm{P} \mapsto \begin{bmatrix} L_1(x_1, x_2, \ldots, x_n) & L_2(x_1, x_2, \ldots, x_n) & \ldots & L_{2q}(x_1, x_2, \ldots, x_n) \end{bmatrix}$$

where $L_i(x_1, x_2, \ldots, x_n)$ is a Laurent polynomial over $\mathbf{F}_2$.

A simple but non-trivial example is to consider a 2D lattice, denoted as $\mathbf{F}_2[x, y]$, with 2 qubits placed on each vertex, labeled by a and b, respectively. The Hamiltonian, which is the negative sum of all stabilizers, is written as:

$$H = -\sum_{i,j} X^a_{i,j} \otimes X^a_{i+1,j} \otimes X^b_{i,j+1}.$$

The subscript $\{i, j\}$ denotes the position of the qubit being acted upon. We can pick any point on the lattice as the origin and denote this origin as position 1. The Hamiltonian term at the origin is referred to as the generator, since all other terms can be obtained by translating this generator. The generator applies σ_x to the first qubit of the a-labeled qubit at position 1 and x, and applies σ_x to the b-labeled qubit at position y. It can be written as the following binary vector:

$$h = \begin{bmatrix} 1 + x & y & 0 & 0 \end{bmatrix}.$$

All Hamiltonian terms can be generated by the formula $M(x, y) \cdot h$, where $M(x, y)$ is a monomial of x and y, representing the position of the Hamiltonian term.

If there are more Hamiltonian generators, we simply have more vectors. Thus, a Hamiltonian or a stabilizer code can be written as a $k \times 2q$ matrix, where k is the number of

generators, and each entry of the matrix is a Laurent polynomial. For a more detailed reference, see[99].

C.2.2 The Ground State Degeneracy of the 3D Trivalent Model

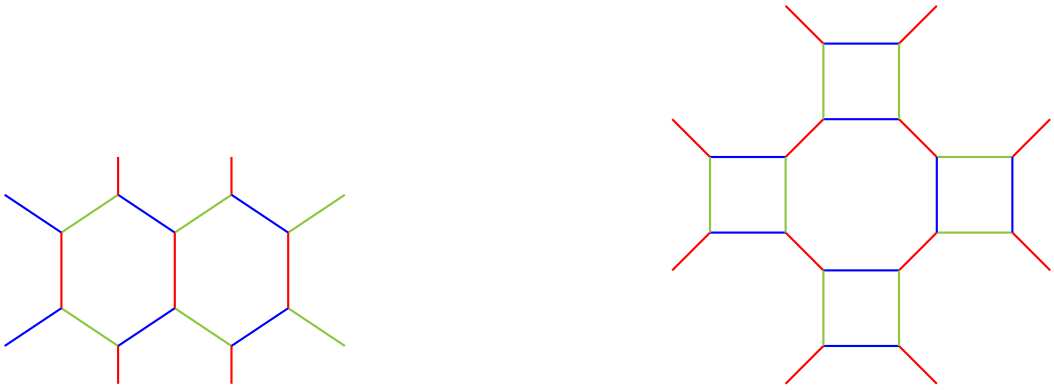

(a) (b)

Figure C.1. C.1a places spin chains extending horizontally and couples them vertically in a specific manner. This setup recovers the honeycomb Kitaev spin liquid model and supports the toric code phase in the limit of strong inter-chain coupling. However, note that this is not a natural Floquet code construction (unless the color of the checks is rearranged). C.1b places closed spin chains and couples them as a square-octagon lattice. Similarly, this can be viewed as a Kitaev spin liquid model, and a $\mathbf{Z}_2$ phase is recovered at the strong inter-chain coupling limit. Indeed, there are various ways to place the spin chains, and they will always recover the $\mathbf{Z}_2$ phase in the strong coupling limit when the interaction diagram is trivalent.

In 2D, different placements of spin chains result in the same phase, as shown in Figure C.1b and Figure C.1a, consistent with the fact that a 2D translationally invariant Pauli Hamiltonian can only support a $\mathbf{Z}_2$ topological phase. However, in 3D, there are many more distinct topological and exotic phases. Here, we identify a special coupling spin chain construction, shown in Figure C.2. This construction deviates significantly from the traditional coupling layer approach, but we prove that it has the same ground state degeneracy (GSD) as the 3D toric code on any manifold, though it is unknown whether they are fully equivalent. This suggests that coupling spin chain constructions could recover more topological phases or even lead to new Floquet codes.

In the context of the Kitaev spin liquid (KSL) or equivalently a gauge-fixed subsystem code, the effective Hamiltonian can be calculated using perturbation theory [77][2]. To rigorously demonstrate that this special construction shares the same GSD as the 3D toric code, we adopt the Laurent polynomial representation of the effective Hamiltonian.

$$H = \begin{pmatrix} x+1 & y+1 & 0 & 0 & 0 & 0 & 0 & 0 & 1 & 1 & 1 & 1 \\ 0 & 0 & 0 & 0 & 0 & 0 & y+1 & xy+y & y & xy & x & 1 \\ 0 & z+1 & z+1 & z+1 & 0 & 0 & 0 & 0 & z & z & 0 & 0 \\ 0 & yz+y & 0 & 0 & z+1 & z+1 & 0 & 0 & 0 & 0 & z & z \\ z+1 & 0 & 0 & z+1 & z+1 & 0 & 0 & 0 & 0 & 1 & 1 & 0 \\ 0 & 0 & 0 & 0 & xz+x & z+1 & z+1 & 0 & 0 & 0 & x & 1 \\ 0 & 0 & z+1 & xz+x & 0 & 0 & z+1 & 0 & 1 & x & 0 & 0 \\ 0 & 0 & yz+y & 0 & 0 & z+1 & 0 & yz+y & yz & 0 & 0 & z \end{pmatrix}$$

Each column represents a generator of the Hamiltonian. Thus, the Hamiltonian contains 8 generators, and each unit cell has 6 qubits. We find the following invertible matrices:

$$r = \begin{pmatrix} 0 & 0 & 0 & 0 & 0 & 0 & 0 & 0 & 0 & 0 & 0 & 1 \\ 0 & 0 & 0 & 0 & 0 & 0 & 0 & 0 & 1 & 0 & 0 & 1 \\ 0 & 0 & 0 & 0 & 0 & 0 & 0 & 0 & 0 & 0 & 1 & 1 \\ 0 & 0 & 0 & \bar{x} & \bar{x} & 0 & \bar{x} & 0 & \bar{z}+1 & \bar{x}\bar{z}+\bar{x} & \bar{x}\bar{z}+\bar{x} & \bar{z}+1 \\ 0 & 0 & 0 & 0 & 0 & 0 & 0 & 0 & x\bar{z} & \bar{z} & \bar{z} & x\bar{z} \\ 0 & 0 & 0 & 0 & 0 & 0 & 0 & \bar{y} & 0 & 0 & 0 & 0 \\ 0 & 0 & 0 & z\bar{x} & z\bar{x} & 0 & z\bar{x}+\bar{x} & 0 & 0 & z\bar{x}+\bar{x} & z\bar{x}+\bar{x} & 0 \\ 0 & 0 & 0 & 0 & 1 & 1 & 0 & z\bar{y}+\bar{y} & 0 & 0 & z+1 & z+1 \\ 0 & 0 & 1 & \bar{x} & \bar{x} & 1 & 0 & 0 & \bar{z}+1 & \bar{x}\bar{z}+\bar{x} & \bar{x}\bar{z}+\bar{x} & \bar{z}+1 \\ \bar{x}\bar{z} & 0 & 0 & 0 & \bar{x}\bar{z} & \bar{x}\bar{z} & 0 & \bar{x}\bar{y}\bar{z} & 0 & 0 & 0 & \bar{x}\bar{z}+\bar{z} \\ 0 & 0 & 0 & 0 & 0 & \bar{z} & 0 & 0 & 0 & 0 & 0 & 0 \\ 0 & \bar{y} & 0 & \bar{x}\bar{y} & \bar{x}\bar{y} & 0 & \bar{x}\bar{y} & 0 & \bar{y}\bar{z}+\bar{y} & \bar{x}\bar{y}\bar{z}+\bar{x}\bar{y} & \bar{x}\bar{y}\bar{z}+\bar{x}\bar{y} & \bar{y}\bar{z}+1 \end{pmatrix}$$

$$l = \begin{pmatrix} 1 & 0 & 0 & 1 & 0 & 0 & 1 & z+1 \\ 0 & 0 & 0 & 1 & 0 & 0 & 0 & 0 \\ 0 & 0 & 0 & 0 & 1 & y & 0 & 1 \\ 0 & 0 & 0 & 0 & 0 & 1 & 0 & 1 \\ 0 & 0 & 1 & x+1 & 0 & z & x+1 & x+1 \\ 0 & 0 & 0 & 0 & 0 & 0 & 1 & 1 \\ 0 & 1 & 0 & y+1 & z & 0 & 1 & 1 \\ 0 & 0 & 0 & 0 & 0 & 1 & 0 & 0 \end{pmatrix}$$

The $\bar{i}$, for $i \in \{x, y, z\}$, denotes the inverse of i. We find:

$$r \cdot H^T \cdot l = \begin{pmatrix} 1 & 0 & 0 & 0 & 0 & 0 & 0 & 0 \\ 0 & 1 & 0 & 0 & 0 & 0 & 0 & 0 \\ 0 & 0 & 1 & 0 & 0 & 0 & 0 & 0 \\ 0 & 0 & 0 & y+1 & z+1 & 0 & 0 & 0 \\ 0 & 0 & 0 & 0 & x+1 & y+1 & 0 & 0 \\ 0 & 0 & 0 & x+1 & 0 & z+1 & 0 & 0 \\ 0 & 0 & 0 & 0 & 0 & 0 & 0 & 0 \\ 0 & 0 & 0 & 0 & 0 & 0 & 0 & 0 \\ 0 & 0 & 0 & 0 & 0 & 0 & 0 & 0 \\ 0 & 0 & 0 & 0 & 0 & 0 & \bar{x}+1 & 0 \\ 0 & 0 & 0 & 0 & 0 & 0 & \bar{z}+1 & 0 \\ 0 & 0 & 0 & 0 & 0 & 0 & \bar{y}+1 & 0 \end{pmatrix}$$

The RHS is equivalent to the 3D toric code Hamiltonian, tensored with 3 ancilla qubits. The ground state degeneracy (GSD) is given by $\log_2 \mathrm{GSD} = \mathrm{rank}\,(\ker(H\sigma)/H)$. Since both r and l are invertible, this model exhibits the same GSD behavior as the 3D toric code. However, since r and l are not symplectic, we cannot simply conclude that these two models are equivalent up to a quantum circuit.

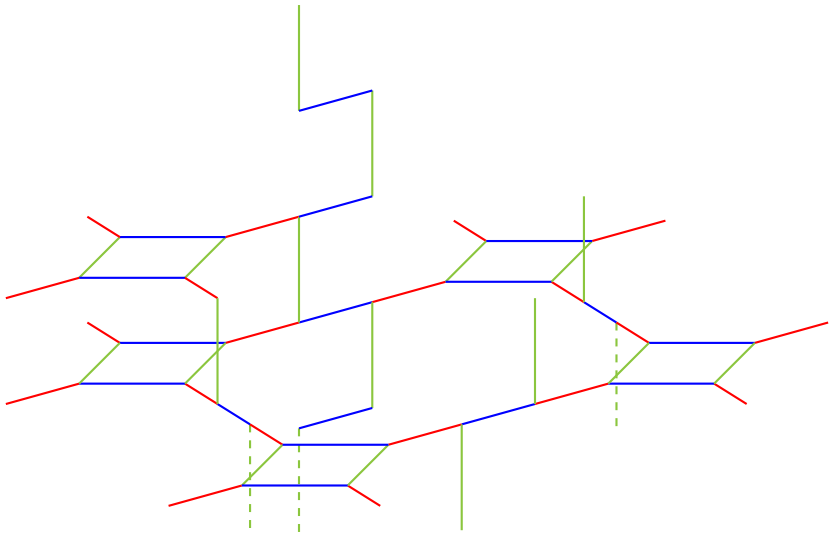

Figure C.2. It shows a special spin chain construction of a 3d Kitaev spin liquid model. Closed spin chains on squares are places on each plane and coupled to vertically spin chains . We prove it is topological phase that share the same GSD with 3d toric code at the strong coupling limit. It also have the mobile point like charges excitations.

C.3 The evolution of logic operator

In this appendix, we will present, in Figure C.3, the evolution of the logical operator of the 2D toric code to demonstrate the necessary requirements to maintain the logical information of the 3D Floquet code, by doubling the measurement routine as first discussed in [86].

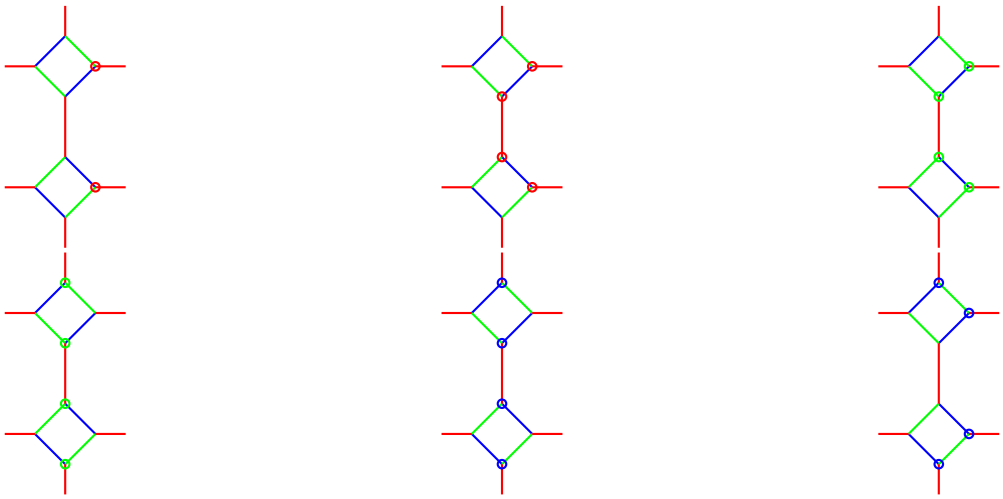

Figure C.3. The evolution of the logical operator in a measurement routine. Each subfigure represents the current logical operator at each measurement round. From top-left to bottom-right, red, blue, and green checks are measured respectively. Each small (red/blue/green) circle represents a $Z/Y/X$ Pauli operator at the marked position, and the logical operator is the tensor product of the operators on the circles. It is shown that the logical operator changes its type after 3 steps of measurement and evolves back after 6 steps. The entire process requires consecutive closed spin chains connected by red checks.

Where the green/blue/red segments represent the corresponding checks, and the blue/-green/red circles represent the $Y/X/Z$ Pauli operators acting on the qubits at the marked vertices, forming the instantaneous logical operator. The evolution itself is not new, but it is important to highlight that this evolution can be achieved within a series of closed spin chains coupled through red checks. As mentioned earlier, the division of red and black checks is hand-chosen. Therefore, when the lattice satisfies the requirements in Section 4.3, we can select three series of non-overlapping plaquettes along three homotopically nontrivial loops on the lattice, which is sufficient to ensure that three line logical operators of the instantaneous 3D toric code phase survive.

C.4 Properties of higher dimensional X-cube code

As proposed in Section 4.3.4, we are able to construct the Floquet code with an instantaneous phase being the higher-dimensional X-cube code on locally hyper-cubic lattices. In an n-dimensional cubic lattice, the Hamiltonian is given by Equation 4.3.5. The number of ground state degeneracies is given by $N_q - N_S$, where N_q is the number of qubits, and N_S is the number of independent generators of the stabilizer group. The conditions $I_{q+1} = 0$ and $I_q \neq 0$ ensure that there is non-trivial ground state degeneracy (GSD) and no local logical operator, confirming a topological phase. Clearly, the GSD is a polynomial in the size of the cubic lattice L. We address the leading order of GSD as follows:

On an n-dimensional $L \times L \times \cdots \times L$ cubic lattice with periodic boundary condition, the translational group is represented by $\mathbf{F}_2[x_1, x_2, \ldots, x_n]$, where $x_i^L = 1$. There are L^n vertices, $n \cdot L^n$ edges, and L^n n-cells. Since each edge has a qubit placed on it, $N_q = n \cdot L^n$.

For the generator $A_v^{x_i,x_j}$, notice that $A_v^{x_i,x_j} \cdot A_v^{x_i,x_k} = A_v^{x_j,x_k}$. Thus, $A_v^{x_1,x_i}$ for $i = 2, 3, \ldots, n$ forms a complete set of generators. With the notation of Laurent polynomials, we have the generators:

$$A^{i,j} = (0, \ldots, 1 + \bar{x}_i, 0, \ldots, 1 + \bar{x}_j, \ldots, 0 \;||\; 0, 0, \ldots, 0),$$

where $1 + \bar{x}_i$ and $1 + \bar{x}_j$ appear at the i-th and j-th positions, respectively, and $\bar{x}_i = x_i^{-1}$. The symbol $||$ represents the division between the representation of the Pauli-X and Pauli-Z regions.

As discussed above, $A^{1,i}$ for $i = 2, 3, \ldots, n$ constitutes a complete set of almost independent generators. Any term in the Hamiltonian can be represented as $M(x_1, x_2, \ldots, x_n)A^{1,i}$, where $M(x_1, x_2, \ldots, x_n)$ is a monomial of $x_1, x_2, \ldots, x_n$. Therefore, we estimate that $N_{S_A} \approx (n-1) \cdot L^n$, where $\approx$ is used because these generators are not exactly independent.

To understand this dependency, note that since the lattice has periodic boundary conditions, we define $K_i = 1 + x + x^2 + \cdots + x^{L-1}$ such that $K_i \cdot (1 + x_i) = 0$ over $\mathbb{F}_2$. Thus, the constraints are represented by $M(x_1, \ldots, \tilde{x}_i, \ldots, \tilde{x}_j, \ldots, x_n)K_iK_j \cdot A^{i,j} = 0$, where $M(x_1, \ldots, \tilde{x}_i, \ldots, \tilde{x}_j, \ldots, x_n)$ is any monomial of variables $x_1, x_2, \ldots, x_n$, excluding x_i and x_j. This contributes $\binom{n}{2} \cdot L^{n-2}$ constraints, which we call 2-constraints since they are induced from the 2D planes. We conclude that:

$$N_{S_A} \approx (n-1) \cdot L^n - \binom{n}{2} \cdot L^{n-2}$$

Again, we use $\approx$ since the above 2-constraints are not independent. For example,

$$M(x_4, x_5, \ldots, x_n) x_3^k K_1 K_2 A^{1,2} = 0 \qquad M(x_4, x_5, \ldots, x_n) K_3 K_1 K_2 A^{1,2} = 0$$

For k ranging from $0, 1, 2, \ldots, L-1$, the second equation is obtained by summing k up in the first equation. Similarly, we get:

$$M(x_4, x_5, \ldots, x_n) K_3 K_1 K_2 A^{1,3} = 0 \qquad M(x_4, x_5, \ldots, x_n) K_3 K_1 K_2 A^{2,3} = 0$$

However,

$$M(x_4, x_5, \ldots, x_n) K_3 K_1 K_2 A^{1,2} \cdot M(x_4, x_5, \ldots, x_n) K_3 K_1 K_2 A^{1,3} = M(x_4, x_5, \ldots, x_n) K_3 K_1 K_2 A^{3,2}$$

The coefficients $M(x_4, x_5, \ldots, x_n) K_3 K_1 K_2$ represent positions, so they have to match to allow the product as shown above. These equations demonstrate that the 2-constraints are not independent in any 3D hyperplane. We call the redundancy of 2-constraints the 3-constraints. The number of 3-constraints is clearly of the order L^{n-3}.

This process can be iterated: the number of k-constraints is of the order of L^{n-k} and is further reduced by $(k+1)$-constraints, which are of the order of L^{n-k-1}, over $(k+1)$-dimensional hyperplanes. If we denote the number of k-constraints as ξ_k, we obtain:

$$N_{S_A} = (n-1) \cdot L^n - \xi_2 + \xi_3 - \ldots$$

where $\xi_2 = \binom{n}{2} L^{n-2}$. Similarly, for the B_c terms, they are not independent. The generator of B_c is represented as:

$$B = (0, 0, \ldots, 0 \mid\mid \Xi/(1+x_1), \Xi/(1+x_2), \ldots, \Xi/(1+x_n))$$

where $\Xi = \prod_{i=1,2,\ldots,n}(1+x_i)$. Similarly, $M(x_1,\ldots,\tilde{x}_i,\ldots,\tilde{x}_j,\ldots,x_n)K_iK_j \cdot B = 0$, and we have almost the same structure as for $A^{i,j}$. Thus, $N_{S_B} = L^n - \xi_2 + \xi_3' - \ldots$, where ξ_3' is not necessarily equal to ξ_3. Since the generators B_c and A_v are mutually independent, we get $N_S = N_{S_A} + N_{S_B}$, and:

$$\log_2 \mathrm{GSD} = N_q - N_S = 2 \cdot \binom{n}{2} L^{n-2} + \mathrm{poly}(L, n-3) \tag{C.2}$$

where $\mathrm{poly}(L, n-3)$ is a polynomial in L with a degree less than $n-3$. This equation clearly holds in both dimension 3 and dimension 2 (which returns to the toric code), and aligns with numerical results in dimension 4.

The behavior of excitations is quite similar to that in 3D. We have lineons that move freely along specific lines but cannot turn, and membrane operators that trap excitations at the corners of the membrane. However, a pair of lineons, commonly referred to as a dipole, exhibits the same mobility as individual lineons. In 4D, these dipoles can turn when a quadrupole of lineons is paired up. More generally, in dimension n, an $(n-2)$-dimensional multipole can freely move in a plane perpendicular to the dimension spanned by the multipole, suggesting a higher-dimensional tensor field description.